

Alma Mater Studiorum - Università di Bologna

DOTTORATO DI RICERCA IN
DATA SCIENCE AND COMPUTATION

Ciclo 34

Settore Concorsuale: 09/G2 - BIOINGEGNERIA

Settore Scientifico Disciplinare: ING-INF/06 - BIOINGEGNERIA ELETTRONICA E
INFORMATICA

MATHEMATICAL METHODS TO ANALYZE AND INTERPRET CALCIUM
SIGNALS OF ASTROCYTES

Presentata da: Jacopo Bonato

Coordinatore Dottorato

Daniele Bonacorsi

Supervisore

Stefano Vittorio Tiziano Panzeri

Co-supervisore

Andrea Cavalli

Esame finale anno 2023

Mathematical methods to analyze and interpret calcium signals of astrocytes

Jacopo Bonato

Abstract

Astrocytes are the most numerous glial cell type in the mammalian brain and permeate the entire CNS interacting with neurons, vasculature, and other glial cells. Astrocytes display intracellular calcium signals that encode information about local synaptic function, distributed network activity, and high-level cognitive functions.

Several studies have investigated the calcium dynamics of astrocytes in sensory areas and have shown that these cells can encode sensory stimuli. Nevertheless, only recently the neuro-scientific community has focused its attention on the role and functions of astrocytes in associative areas such as the hippocampus. In our first study, we used the information theory formalism to show that astrocytes in the CA1 area of the hippocampus recorded with 2-photon fluorescence microscopy during spatial navigation encode spatial information that is complementary and synergistic to information encoded by nearby "place cell" neurons.

In our second study, we investigated various computational aspects of applying the information theory formalism to astrocytic calcium data. For this reason, we generated realistic simulations of calcium signals in astrocytes to determine optimal hyperparameters and procedures of information measures and applied them to real astrocytic calcium imaging data.

Calcium signals of astrocytes are characterized by complex spatiotemporal dynamics occurring in subcellular parcels of the astrocytic domain which makes studying these cells in 2-photon calcium imaging recordings difficult. However, current analytical tools which identify the astrocytic subcellular regions are time consuming and extensively rely on user-defined parameters. Here, we present Rapid Astrocytic calcium Spatio-Temporal Analysis (RASTA), a novel machine learning algorithm for spatiotemporal semantic segmentation of 2-photon calcium imaging recordings of astrocytes which operates without human intervention. We found that RASTA provided fast and accurate identification of astrocytic cell somata, processes, and cellular domains, extracting calcium signals from identified regions of interest across individual cells and populations of hundreds of astrocytes recorded in awake mice.

Acknowledgments

I would like to thank my family, Giorgia and Francesco, who have supported me in all my endeavors. The last 4 years have been an extremely important life lesson from which I have learned so much.

I would like to express my gratitude to my supervisor Stefano Panzeri. Under his supervision I have learned a lot, but I really appreciate that I have been able to develop my scientific attitude and *forma-mentis* thanks to his valuable feedback. Moreover, I must thank Stefano Panzeri for his help in developing new technical analyzes, correctly interpreting the results obtained in the different studies, and writing the studies.

I would like to thank Tommaso Fellin for all his great feedback and for writing a large part of the "Plos Biology" paper together with Stefano Panzeri.

I would like to thank Sebastiano Curreli for providing most of the data used in this Thesis, for the detailed and rich scientific discussions we had, and for the nice time we spent together.

I would like to thank Sara Romanzi for providing her data used in the RASTA study and for her valuable feedback on the RASTA open source software.

Table of Contents

Abstract	i
Aknowledgements	ii
Table of Contents	iii
List of Figures	v
1 Introduction	1
1.1 Astrocytes	1
1.2 Mathematical methods to analyze and interpret calcium signals of astrocytes	9
2 Complementary encoding of spatial information in hippocampal astrocytes	13
2.1 Introduction	13
2.2 Results	13
2.3 Discussion	24
2.4 Methods	27
3 Optimizing measures of information encoding in astrocytic calcium signals	43
3.1 Introduction	43
3.2 Computing amount and significance of information in astrocytic calcium activity	44
3.3 Measuring conditional mutual information to evaluate genuine information encoding	49
3.4 Spatial information in CA1 astrocytes during spatial navigation . . .	50
3.5 Conclusions	51
4 Rapid spatiotemporal analysis of astrocytic calcium dynamics using deep learning	53
4.1 Introduction	53
4.2 Results	55

4.3	Methods	65
5	Conclusions	81
5.1	Complementary encoding of spatial information in hippocampal astrocytes	81
5.2	Optimizing measures of information encoding in astrocytic calcium signals	83
5.3	Rapid spatiotemporal analysis of astrocytic calcium dynamics using deep learning	85
	Bibliography	89
A	Chapter 2: Supplementary material	107
B	Chapter 4: Supplementary material	141
B.1	Neuronal and astrocytic algorithms	141
B.2	Algorithm details	142

List of Figures

1.1	Astrocyte main sub-structures	3
1.2	A schematic summary of the diverse roles performed by astrocytes in the functioning brain	5
1.3	Schematics of 2-photon Ca^{2+} imaging experimental setup for a mice running on a wheel	7
1.4	Somata and processes in astrocytes present complex calcium transients	8
2.1	Astrocytic calcium signals in the CA1 hippocampal area encode spatial information during virtual navigation	17
2.2	Topographic organization of spatial information encoding in astrocytes: somas vs processes.	19
2.3	Efficient decoding of the animal's spatial location from astrocytic calcium signals.	20
2.4	The majority of spatial information in astrocytes is genuine spatial information that cannot be explained by tuning to visual cues.	22
2.5	Astrocytes have broader response field width and a different distribution of field position compared to neurons.	23
2.6	Spatial information encoding in astrocytes is complementary and synergistic to spatial information encoding in neurons.	24
3.1	Sensitivity of information content measures for realistic simulations of position encoding astrocytic Ca^{2+} signals.	47
3.2	Characterization of information theoretic methods applied on simulations of astrocytic Ca^{2+} responses.	48
3.3	Determining the significance of conditional mutual information. (A) Schematic of a virtual track containing three distinct visual patterns	50
3.4	Spatial information encoding in CA1 astrocytes during virtual navigation.	52
4.1	RASTA: a machine learning algorithm for fast and automatic semantic segmentation of astrocytes.	54
4.2	Evaluation and benchmarking of RASTA on dataset-1.	59
4.3	Identification of statistically correlated calcium signals in astrocytic domains using RASTA.	60
4.4	Impact of image noise and pre-processing on RASTA performance.	63
4.5	RASTA performance on never-before-seen data.	64

4.6	RASTA pipelines.	71
4.7	Schematic representation of RASTA modules.	73
A.1	Chronic CA1 window to monitor astrocytic calcium dynamics in head restrained mice.	120
A.2	Identification of reliable spatial modulation of astrocytic calcium signals.	121
A.3	Reliable spatial modulation of astrocytic calcium signals.	122
A.4	Modulation of astrocytic calcium responses during locomotion and virtual navigation.	123
A.5	Calcium signals of CA1 astrocytes encode direction selective spatial information during virtual bidirectional navigation.	124
A.6	Anatomical organization of subcellularly localized astrocytic calcium signals.	125
A.7	Temporal relationships among subcellularly localized astrocytic calcium signals.	126
A.8	Decoding animal's position from astrocytic calcium signals in the unidirectional virtual navigation task.	126
A.9	Decoding animal's position from astrocytic calcium signals in the bidirectional virtual navigation task.	127
A.10	Visual cues identities do not explain animal's position decoding from astrocytic calcium signals.	128
A.11	Chronic CA1 window to simultaneously monitor astrocytic and neuronal calcium signals in head restrained mice.	129
A.12	Temporal relationships between astrocytic and neuronal signals.	130
A.13	Modulation of astrocytic and neuronal calcium responses during locomotion and virtual navigation.	131
A.14	Pairwise correlations of calcium signals during virtual navigation.	132
A.15	Pairwise correlation of calcium signals and difference in field position as a function of pairwise distance.	133
A.16	Precision and stability of neuronal and astrocytic spatial responses.	134
A.17	The majority of spatial information in astrocytes and neurons is genuine spatial information that cannot be explained by tuning to visual cues.	134
A.18	Visual cues identity does not explain animal's position decoding from neither astrocytic nor neuronal calcium signals.	135
A.19	Astrocytes and neurons encode complementary and synergistic spatial information.	136
A.20	Position-dependent correlations contribute to synergistic information encoding.	137
A.21	Correlation between astrocytes and neurons is animal's position-dependent.	138
A.22	Decoding the animal's position from neuronal and astrocytic population vectors.	139
B.1	RASTA pre-processing.	146
B.2	Generation of the consensus annotation.	147

B.3	Precision and Recall of RASTA semantic segmentation against human annotators on dataset-1.	148
B.4	Representative example of segmentations of somata and processes.	148
B.5	RASTA semantic segmentation against GECI-quant segmentation.	149
B.6	RASTA seeding of event-based segmentation.	150
B.7	RASTA performance under various signal-to-noise ratio regimes.	151
B.8	Performance of RASTA and other algorithms under various signal-to-noise ratio regimes.	152
B.9	Impact of pre-processing modules on RASTA performances.	153
B.10	RASTA performance as a function of recordings length.	153
B.11	RASTA detection and segmentation performance on dataset-2.	154
B.12	RASTA detection and segmentation performance on dataset-3.	155
B.13	RASTA detection and segmentation performance on dataset-4.	156
B.14	Execution time of the RASTA inference pipeline.	157

Chapter 1

Introduction

1.1 Astrocytes

Glia, also called glial cells or neuroglia¹, are electrically non-excitabile non-neuronal cells in the central nervous system (CNS, brain and spinal cord) and peripheral nervous system. Glia were first discovered in 1856 by the pathologist Rudolf Virchow and then better described and made known to a wider public several decades later by Santiago Ramón y Cajal and Pío del Río Hortega. Thanks to electrophysiological characterizations and physiological studies of glial cells in the second half of the 20th century, significant progress was made in understanding the multiple vital functions of glial cells [1–6].

Glia are an abundant cell type in the CNS and are essential for the brain to function as an organ and as a computational structure [7]. In mammals, glia can be divided into 2 macrogroups resembling their embryonic origin: microglia and macroglia.

Microglia cells originate from yolk sac progenitor cells that populate the brain only during development [reviewed in [8, 9]], a feature that distinguishes this group from other glial cells. Microglia represent the major immunocompetent and phagocytic cells of the CNS [10] and cover much of the adult brain in discrete, non-overlapping domains. Microglia sense the environment through the movement of their filopodia and respond rapidly to abnormalities or damage [11]. In addition to their role in the immune system, microglia have recently been ascribed an active role in the healthy brain, although opinions on this are controversial[12–17].

Macroglia, the other macrogroup of glial cells, originate from neuroectoderm and can be further divided into 3 categories: *oligodendrocytes*, their progenitors *NG2-glia*, and *astrocytes*.

Oligodendrocytes form the myelin sheath that surrounds and insulates neuronal axons, resulting in increased conduction velocity of the action potential (AP)[18]. However, high numbers of nonmyelinating oligodendrocytes have also been found

¹The term originates from Greek term for "glue"

in sparsely myelinated brain regions, and presumably these oligodendrocytes have other overlooked functions.

The recently discovered NG2-positive cells are precursors of oligodendrocytes [19]. NG2 glia are part of the oligodendrocyte lineage and form mature myelinating oligodendrocytes throughout their life [20–23]. NG2 glia have been observed to form a tight homeostatic network in the adult rodent brain in which cell numbers are maintained stable under physiological conditions. The gap produced by cells differentiations or death is immediately replaced by a neighboring cell [24]. One particular aspect of NG2 glial cells, originally discovered in the hippocampus [25] but also observed in other parts of the brain (reviewed in [26]), is the ability to form functional synapses with neurons. Although the function of these synapses is not yet fully understood, a distinctive aspect of these synapses is their directionality. NG2 glia can receive neuronal signals but cannot generate and transmit action potentials themselves [27].

The final major group of macroglial cells in the brain is astrocytes. The anatomy of astrocytes and the function of their intracellular signals are highly relevant aspects for this work. For this reason, in the next sections we will briefly review their anatomy, function, signalling, and their known relationships with neuronal activity.

Astrocytes anatomy

Astrocytes are the most abundant glial cell type in the mammalian brain [28]. Even though astrocytes were discovered about 150 years ago, our understanding of their role in brain function is far from complete.

Astrocytes are a heterogeneous group of cells, showing differences in morphology, molecular profile, and function [29]. From a morphological point of view, astrocytes can be broadly divided into two types: fibrous and protoplasmic. Fibrous astrocytes are star-shaped cells with regular contours. They are mainly found in the white matter of the brain, spinal cord, optic nerve, and retinal fiber layer. These astrocytes are characterized by an elongated morphology in which their long processes make extensive contact with blood vessels, form a gap junction between the distal processes of adjacent astrocytes, and form nodes of Ranvier ². The processes of fibrous astrocytes are characterized by spatial overlap in the cell domain; moreover, the processes extend to perivascular, subpial, and axonal endfeet [30].

Protoplasmic astrocytes are characterised by a "bushy" and irregular morphology. The small round cell body, called soma, is about 10 μm in diameter (Fig. 1.1). A protoplasmic astrocyte has 5 to 10 primary processes that further branch into thousands of branches, forming dense arborizations that contact synapses (Fig. 1.1) [31]. In addition, astrocytic processes contact the vasculature via the so-called processes endfeet [32, 33]. This class of astrocytes mainly populates the grey matter in the brain with well-defined domains that have minimal overlap [31]. A single

²Nodes of Ranvier are the small, interspersed, non-myelinated interruptions along the length of an axon that help conduct nerve impulses

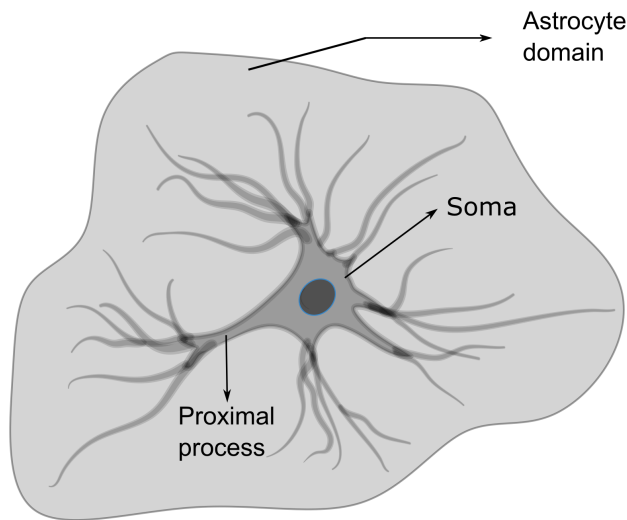


Figure 1.1: Astrocyte main substructures. Soma: main cell body. Proximal processes: biggest substructures that grow from soma. Astrocyte domain: territory comprising all branches and branchlets of astrocyte

astrocyte domain can cover an area of 20,000 to 80,000 μm^3 (Fig. 1.1) and be in contact with 300 to 600 dendrites and potentially 100,000 individual synapses [31, 34]. This dense connectivity allows astrocytes to control multiple functions, including ion homeostasis, neurotransmitter clearance, trophic support of neurons, and neuromodulation.

In the further course of this thesis, the term astrocytes is used for protoplasmic astrocytes.

Astrocytes functions

The complex morphology of astrocytes, especially their numerous contacts with synapses and blood vessels, makes this cell type a very influential cell in the brain. Therefore, understanding the main functions of astrocytes in the brain is a fundamental question that needs to be answered.

This is still an active area of research, even though many functions of astrocytes have already been discovered and characterized (Fig. 1.2). Some of the most important functions are enumerated below, including contributions to the blood-brain barrier, regulation of blood flow, energetic support, regulation of synaptic activity, buffering of neurotransmitters, and secretion of neuroactive substances (reviewed in [35]).

The blood-brain barrier (BBB) is an cerebral vasculature feature where astrocytes are involved, that consists of preventing the influx of certain molecules into the brain parenchyma depending on their polarity and size [36, 37]. BBB is constituted by astrocytes endfeets, perivascular pericytes³, basal lamina⁴, and capillary endothelial cells. Capillary endothelial cells are surrounded by the other BBB con-

³Pericytes are cells present at intervals along the walls of capillaries.

⁴The basal lamina is a layer of extracellular matrix secreted by epithelial cells on which the epithelium sits.

stituents forming tight junctions with them. Although both pericytes and astrocytes endfeets are involved in the BBB mechanism, their role in the BBB has not been fully elucidated [36–41]. For this reason, further studies are needed to elucidate the initial molecular mediators that may cause BBB properties in cerebral endothelia and how astrocyte endfeets and pericytes are involved in BBB functions.

The large number of contacts of astrocytes with blood vessels in the CNS allows astrocytes to have basic bidirectional interactions with blood vessels, where, for example, blood flow in the CNS is regulated. Through the production of molecular mediators (such as prostaglandins, nitric oxide, and arachidonic acid), astrocytes can increase or decrease the diameter of CNS blood vessels and blood flow [42, 43]. In addition, changes in neuronal activity can cause local changes in CNS blood flow thanks to the mediating role of astrocytes [44]; processes that contact both blood vessels and synapses can control blood flow depending on the level of synaptic activity [45]. This phenomenon has been observed in visual cortex, where fMRI-detected changes in blood flow in response to visual stimuli were dependent on astrocyte function [46, 47].

In addition, astrocytes contribute to CNS metabolism through their processes which are in contact with neuronal perikarya, axons (at the nodes of Ranvier), synapses and blood vessels. This position allows astrocytes to take up glucose from blood vessels and provide energy metabolites to several neuronal elements in the CNS. Furthermore, astrocytes are the major storage sites of glycogen granules in the CNS, with the greatest glycogen accumulation occurring where synaptic density is high [48–50]. These storage sites are essential for maintaining neuronal activity during hypoglycemia and during periods of high neuronal activity [50, 51].

The release of various active molecules during synaptic activity (such as glutamate, purines, GABA⁵, and D-serine) is sensed by G protein-coupled receptors (GPCRs) in astrocytes. These (GPCRs) enable astrocytes to respond to neurotransmitters or neuromodulators [52, 53]. Following activation of GPCRs, a Ca²⁺ increase occurs in astrocytes. Importantly, these Ca²⁺ increases have been observed in-vivo in both astrocytic processes and their somata [54–59]. Moreover, GPCRs are able to stimulate the release of gliotransmitters that can interact with synaptic elements. This direct and interactive role of astrocytes in synaptic activity has given rise to the "tripartite synapse" hypothesis, according to which astrocytes, together with neurons, are fundamental players in information processing in the neuronal circuit [34, 60, 61].

Moreover, gliotransmission has been observed to contribute to the modulation of all major forms of synaptic plasticity [62]. In several brain regions, astrocytes have been observed to modulate short-term synaptic excitation or depression on time scales ranging from seconds to minutes. Long-lasting synaptic changes lasting tens of minutes, such as long-term potentiation (LTP) and long-term depression (LTD) of synaptic transmission, have also been modulated by astrocytes [52].

⁵Gamma-Aminobutyric Acid

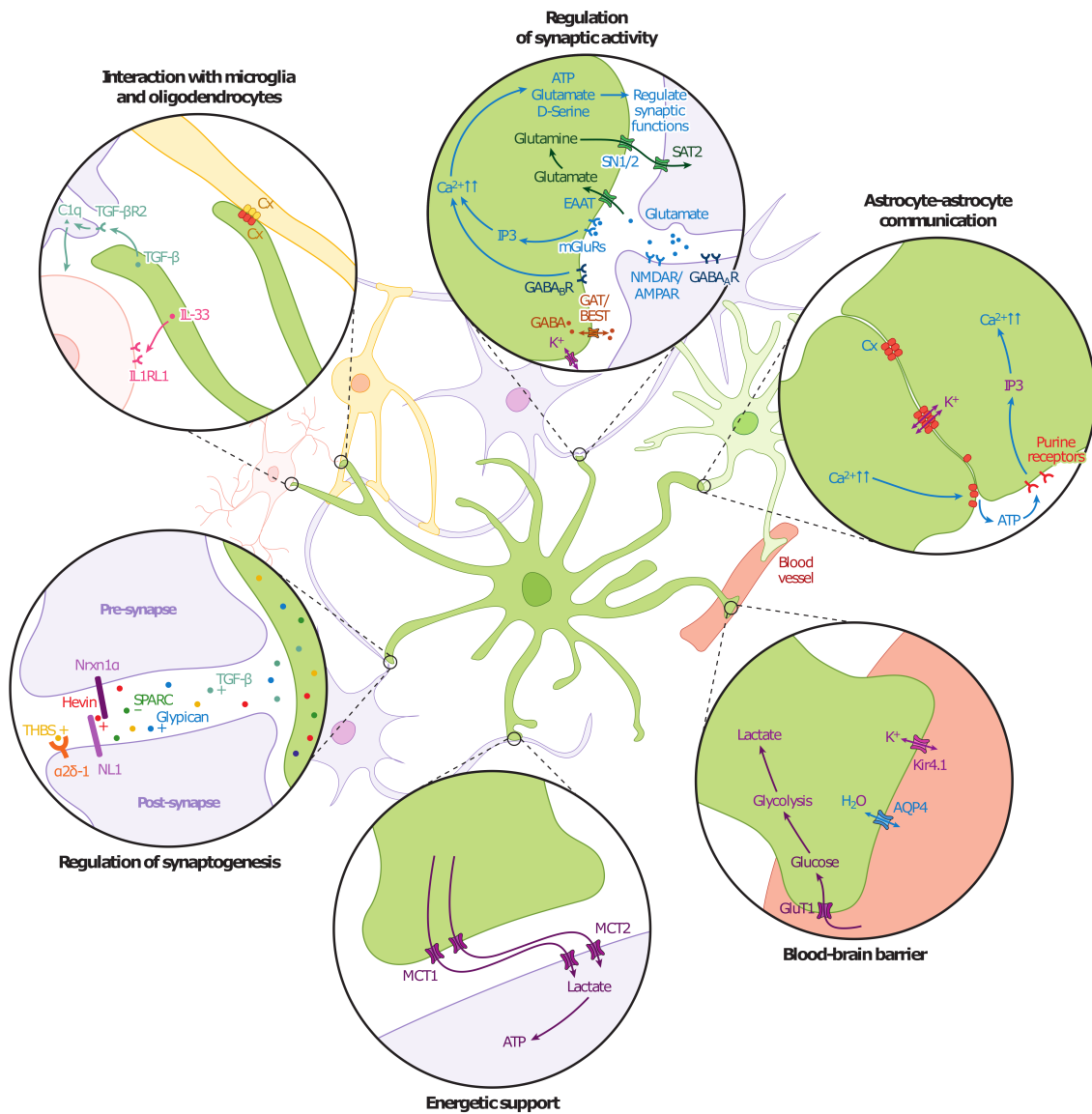


Figure 1.2: A schematic summary of the diverse roles performed by astrocytes in the functioning brain. Abbreviations: AMPAR, α -amino-3-hydroxy-5-methyl-4-isoxazolepropionic acid receptor; BEST, bestrophin; Ca^{2+} , calcium ion; Cx, connexin; EAAT, excitatory amino acid transporter; GABA, γ -aminobutyric acid; GAT, GABA transporter; GluT1, glucose transporter 1; IL, interleukin; IP3, inositol triphosphate; K^+ , potassium ion; MCT1/2, monocarboxylate transporter 1/2; mGluRs, metabotropic glutamate receptors; NMDAR, N-methyl-d-aspartate receptor; Nrxn1 α , Neurexin 1 α ; THBS, thrombospondin. From [63]

In addition to the above functions, astrocytes are involved in ion [64, 65], water [66, 67], and neurotransmitter homeostasis [68, 69]. Finally, important aspects of astrocyte physiology are how their excitability functions based on intracellular Ca^{2+} concentration work, relate and interact with neuronal functions in the brain. These aspects will be discussed in the following two sections.

Calcium signaling

In the early 1990s, a seminal work by Cornell-Bell [4] showed that astrocytes responded to the release of glutamate with intracellular increases in Ca^{2+} . These and other findings [70–72] suggested a possible role of astrocytic Ca^{2+} dynamics in brain circuitry communication. In fact, it has been observed that the Ca^{2+} concentration in astrocytes changes not only spontaneously but also in response to various stimuli. Therefore, monitoring the Ca^{2+} concentration has become a standard method to study the physiological responses of astrocytes in single cells and to compare them between different brain regions [73–77]. The Ca^{2+} dynamics can be monitored using molecular indicators that change their properties (such as brightness during imaging experiment) as a function of the Ca^{2+} concentration. These indicators can either be synthetic ([4], review in [78]) or generated through genetic engineering (i.e. recombinant proteins such as GCaMPs [79]). The observation of Ca^{2+} indicators is performed with optical setups that are used to detect fluorescence signals generated either with 1-photon excitation or exploiting the 2-photon effect.

2-photon calcium imaging 2-photon calcium imaging is an experimental technique that allows to measure Ca^{2+} concentration in astrocytes and neurons [80, 81]. This technique records fluorescence signals from a fluorophore indicator triggered by the absorption of photons transmitted by a laser beam [81, 82]. The 2-photon imaging technique is based on the absorption of two photons that promote the transition of an electron of the fluorophore from the ground state energy level to an excited state. The excited-state electron then decays and a photon with a shorter wavelength than that of the exciting laser beam is emitted. This emitted light is then recorded from each excited sample region (Fig. 1.3).

Two-photon excitation microscopy typically uses excitation light in the near-infrared range, which minimizes scattering in tissue and thus background signals; it reduces photobleaching and increases tissue penetration depth and light detection efficiency [81]. A key feature of this technique is the lack of crosstalk between adjacent zones in the imaged brain tissue as the sample is sequentially excited [83].

Over the past 30 years, 2-photon calcium imaging technology has been improved by increasing the signal-to-noise ratio, temporal resolution, field-of-view size, penetration depth, and accessible volume for in-vivo imaging (reviewed in [84]). The combination of 2-photon calcium imaging with synthetic or genetically engineered indicators represents one of the most powerful experimental methods for studying

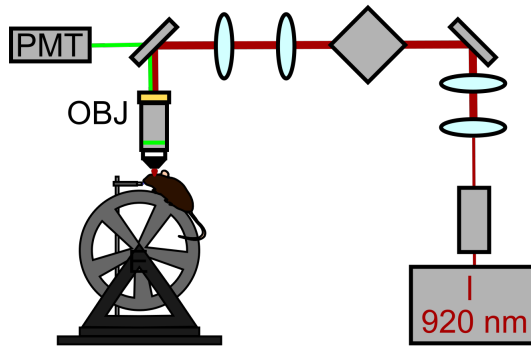


Figure 1.3: Schematics of 2-photon Ca^{2+} imaging experimental setup for a mice running on a wheel. The optical setup is characterized by an exciting laser beam of 920 nm of wavelength which is sent through the optical path to the selected brain region. Fluorescence signals are then collected through objective lenses (OBJ) and a photomultiplier (PMT) and finally recorded.

astrocytic networks in the CNS in-vivo at the subcellular level for several μm^2 of brain area.

Calcium signal in astrocytes. Thanks to this imaging technique, astrocyte Ca^{2+} signaling has been shown to be diverse in its properties, it can occur in different compartments, and it has different underlying mechanisms and variable dependence on neuronal activity (reviewed in [63]).

Spontaneous Ca^{2+} signals in astrocytes have been observed in highly localized subregions in branches and branchlets of astrocytes which are often referred as microdomains [57, 58, 85–89]. These signals were observed without external stimulation of astrocytes or brain tissue and without triggering by firing action potentials of nearby neurons, and only some of them are mediated by Ca^{2+} release from IP3R2⁶-dependent intracellular Ca^{2+} stores [85]. Another spontaneous signal observed in the main branches and occasionally in the somata of the astrocytes are "local waves". These display characteristic spatial and temporal features spreading over few tens of microns of astrocytic processes over 2-3 seconds [85, 90].

Neuronal activity may also mediate Ca^{2+} signaling in astrocytes. In the CA1 and dentate gyrus regions of the hippocampus [91–93], a highly localized type of Ca^{2+} signaling was observed in the microdomain of astrocytes mediated by nearby neurons. Another type of Ca^{2+} signaling triggered by intense AP bursts in mossy fiber axons has been observed in CA3 in the hippocampus [85]; in this case, calcium concentration is not highly localized and may involve entire astrocytes, including their somata. For this reason, the literature refers to it as a "global wave." Another important phenomenon involving neurons and astrocytes is neurovascular coupling. Indeed, during vasodilation, Ca^{2+} release from IP3R2-dependent stores [94] and Ca^{2+} entry via TRPV4 channels [95] have been observed to mediate Ca^{2+} signaling in endfeet of astrocytes in response to neuronal activation.

Another type of Ca^{2+} signaling, extremely broad and covering essentially all astrocytes imaged, was observed in-vivo during locomotion and startle responses.

⁶inositol 1,4,5-trisphosphate receptor type 2

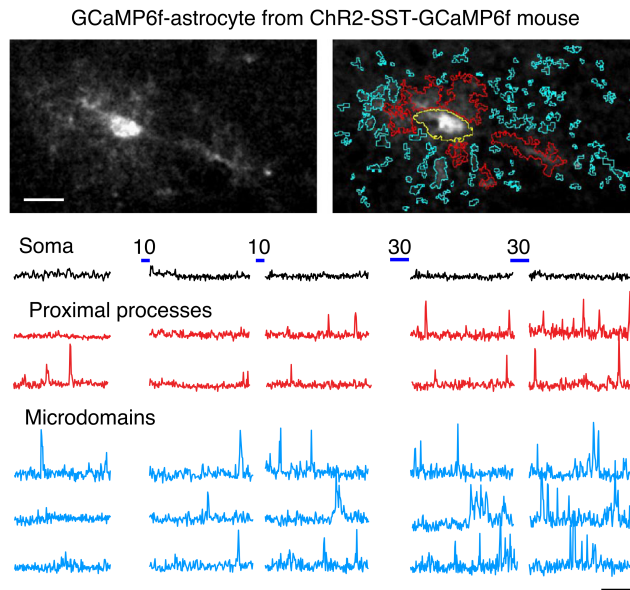


Figure 1.4: Somata and processes in astrocytes present complex calcium transients. Astrocytes in layer 2/3 SSCx from an adult Chr2-SSTGCaMP6f mouse that underwent SST interneuron optogenetic stimulation. ROIs are: soma (yellow), proximal processes (red) and microdomains (blue); scale bar is $20 \mu\text{m}$. Different region of the astrocyte display different Ca^{2+} transients, scale bars are 50 s and $20 (f - f_0)/f_0$, where f is the Ca^{2+} fluorescence trace and f_0 the baseline fluorescence value. Adapted from [59].

Volumetric release of neuromodulators that mobilize intracellular IP3R2-dependent stores controls this type of signaling [86, 96–98]. It has been suggested that these modulators act via the astrocytes themselves, but other cells may also be involved in this process.

Finally, an important aspect of astrocyte signaling involves basal Ca^{2+} levels, through which basal arteriole diameter can be altered [99]. The basal level of Ca^{2+} has been observed to vary between different compartments of astrocytes [99, 100] and is regulated by age and prior activity [101].

Astrocytes and Behaviour

Although the role of astrocytes in the action of neuromodulators has not been fully elucidated, the last two decades have shown how astrocyte responses to neuromodulators affect sensory and motor processes.

In [102], it is shown how astrocytes are fundamental in the cholinergic-induced modulation of visual processing through the release of the neuromodulator acetylcholine. Another important study [46] showed how astrocytes in ferret primary visual cortex respond to visual stimuli with limited spatial receptive fields and sharp tuning to visual stimulus features. Another important study of the primary visual cortex showed how sensory processing is affected by astrocytes heterogeneously modulating the excitability of different neuron subtypes [103].

Motor processes are also influenced by the activity of astrocytes within neuronal circuits. For example, in the dorsal striatum, a brain nucleus important for motor function, astrocytes are involved in its function. In [104] chemogenetic activation of astrocytes in the dorsal striatum was shown to disrupt attention in mice and cause the animals to exhibit hyperactive behaviour. Indeed, activation of astrocytes by

the release of thrombospondin-1 causes an enhancement of the activity of medium-sized spiny neurons. Another important study [105] on motor behaviour showed how conditional deletion of IP3R2 in astrocytes impairs motor skill learning in mice during forelimb grasping task.

Astrocytes are involved not only in sensory-motor processes but also in decision making. A recent study [106] showed how astrocytes in the brainstem of zebrafish act as signal integrators to perform computations critical for controlling behaviour during a decision-making task. In this task, the animals were exposed to a virtual reality environment in which visual feedback was decoupled from motor actions, so that swimming behaviour did not elicit the expected visual flow. This resulted in the animals entering a passive behavioural state after becoming aware of the futility of their efforts. The large-scale optical imaging of astrocytes used in this study showed that the passive behavioural state of the zebrafish was triggered by astrocytes. During swimming episodes that do not trigger perceptual movement, the astrocytic network shows cumulative Ca^{2+} responses triggered by noradrenergic neurons that detect swimming failures. Once the number of swimming failures reaches a threshold, the GABAergic neuronal network is activated by the astrocytic network to suppress swimming.

Similarly in the CA1 area of the mouse hippocampus, the astrocytic network also influences the spatiotemporal dynamics of neuronal networks. First, the astrocytic network integrates neuronal activity and then triggers the barrage firing in some populations of inhibitory interneurons [107].

1.2 Mathematical methods to analyze and interpret calcium signals of astrocytes

As described in the previous sections, astrocytes are not electrically excitable but show excitability depending on their complex dynamics of intracellular Ca^{2+} concentration. The dynamics of astrocytic Ca^{2+} concentration can be studied in-vivo using functional two-photon microscopy [108]. This experimental technique allows to distinguish between somata and proximal processes thanks to its high spatial subcellular resolution.

Several studies [46, 55, 58, 98, 109] investigated the Ca^{2+} dynamics of astrocytes in sensory areas and showed that these cells can encode sensory stimuli. Recently, several laboratories [110–112] have started to investigate how astrocytes encode information about external variables. For example, in our work [111], using the information theory formalism [113, 114], we showed that astrocytes in hippocampal CA1 recorded during spatial navigation in a virtual environment encode spatial information that is complementary and synergistic to information encoded by nearby "place cell" neurons (Sec. 1.2). Moreover, in another recent paper [115], we have shown how to optimally apply the information theory formalism to astrocytic calcium imaging data (Sec. 1.2).

However, the available methods for extracting recordings and analyzing astrocytic calcium data are highly dependent on a large number of user-defined parameters. This limits the analytical workflow, scalability, and reproducibility of astrocyte calcium measurements. For this reason, we have developed a novel algorithm called Rapid Astrocytic Spatio-Temporal Analysis (RASTA) that enables rapid, accurate, and fully automated segmentation and signal extraction of astrocytic Ca^{2+} dynamics (Sec. 1.2).

Complementary encoding of spatial information in hippocampal astrocytes [111]

Neuronal place cells in the hippocampus encode information about the spatial position of the animal by modulating their firing rate as a function of space. This mechanism forms the cellular substrate for spatial cognition. Is this spatial information encoded only in neuronal circuits or beyond?

Therefore, using the two-photon calcium technique, we simultaneously imaged astrocytes and neurons in the CA1 hippocampus of mice navigating in a virtual environment and showed that astrocytes encode spatial information about the animal's position in virtual space in their Ca^{2+} signals. We observed that spatial informative Ca^{2+} dynamics in astrocytes occur in topologically bounded and topographically organized regions that include both somata and processes. The spatial fields of astrocytes were larger and centered at different positions compared with neuronal place fields. Moreover, the spatial information encoded in astrocytes was complementary and synergistic to that carried by nearby "place cell" neurons, resulting in an increase in decoding performance when astrocytic and neuronal signals were considered together.

These results show for the first time how spatial information encoded in the spike outputs of projecting CA1 neurons in the hippocampus is locally complemented by non-neural CA1 elements. This additional reservoir of spatial information expands the population-coding capacity of the hippocampal network and reveals a new level of organization for encoding spatial information in the hippocampus.

Optimizing measures of information encoding in astrocytic calcium signals[115]

According to recent studies [110–112], the calcium dynamics of astrocytes, the most abundant glial cell type in the mammalian brain, contain information about important cognitive variables but also provide information not contained in the activity of nearby neurons. Understanding the role and contribution of astrocytes in information processing is fundamental to describe the functioning of the CNS. For this reason, analytical tools that allow the description of this contribution are needed. We simulated realistic astrocytic activities that depended on external variables to optimally set the parameters of the information-theoretic analysis of astrocytic ac-

tivity. Finally, we applied information analyses to both simulated and real astrocytic data to obtain conservative and reliable estimates of astrocytic calcium contribution to circuit-level information processing in the brain.

Rapid spatiotemporal analysis of astrocytic calcium dynamics using deep learning

In section 1.1 it has been described how astrocytic signals are characterized by complex spatiotemporal dynamics occurring in subcellular regions of the astrocytic cell. Current analytical tools for astrocytic calcium signals are time consuming and extensively rely on user-defined parameters. These pitfalls limit reproducibility and scalability of the workflow and prevent closed-loop experimental approaches. Therefore, the development of a method to obtain rapid, precise, and fully automated segmentation and signal extraction from 2-photon (2P) calcium recording from astrocytes is of utmost importance.

For this reason we developed a novel software for spatiotemporal semantic segmentation of 2P-calcium imaging recordings of astrocytes, called Rapid Astrocytic Spatio-Temporal Analysis (RASTA). RASTA combines deep learning algorithms with feature engineering of calcium data and operates without human intervention. RASTA provides rapid and accurate identification of astrocytic cell somata and processes and it extracts calcium signals from identified astrocytes regions of interest (ROIs).

RASTA combines supervised and unsupervised techniques to provide a fully automatic algorithm for the analysis of spatiotemporal information of astrocytic calcium signals. RASTA's workflow comprises three main blocks: i) pre-processing; ii) semantic segmentation; iii) subcellular cross-correlation analysis. These steps result in an end-to-end characterization of the complex morphological and dynamical properties of astrocytic calcium signals. Pre-processing block computes a bi-dimensional reconstruction of the recorded field-of-view (FOV), compressing spatial and temporal features into spatiotemporal projection. The outputs of the pre-processing block are used as inputs for the second block of the pipeline. The semantic segmentation employs a U-Net [116] based deep neural network (DNN) to perform subcellular semantic segmentation of astrocytic cellular structures, identifying somata and processes. Subcellular cross-correlation analysis identifies regions of the astrocytic cell showing calcium dynamics which are statistically correlated to the morphological structures outlined by the segmentation block

We validated RASTA on in-vivo two-photon calcium imaging data against human manual annotation, obtaining near-human performance in astrocyte detection and segmentation. RASTA outperformed state-of-the-art algorithms for the analysis of astrocytic and neuronal calcium imaging data in detecting and segmenting astrocytic ROIs. Overall, RASTA is an end-to-end analytical tool, which provides fast, automated, and accurate semantic segmentation of two-photon imaging data of astrocytes. RASTA will facilitate the analysis of astrocytic calcium signals and

will enable new closed-loop experimental approaches.

Chapter 2

Complementary encoding of spatial information in hippocampal astrocytes

2.1 Introduction

Astrocytes, the most abundant class of glial cells in the brain, exhibit complex dynamics in intracellular calcium concentration [76]. Intracellular calcium signals can be spatially restricted to individual subcellular domains (e.g., cellular processes vs somata) and be coordinated across astrocytic cells [58, 59, 92, 93, 98, 117, 118]. In the intact brain, astrocytic calcium dynamics can be spontaneous [119] or triggered by the presentation of external physical stimuli [46, 55, 58, 98, 109]. Interestingly, previous reports suggest that astrocytic calcium signals triggered by external sensory stimuli largely mirror the activity of local neuronal cells [46, 109]. Such findings have led current models of sensory information coding in the brain to overlook the contribution of astrocytes, under the implicit or explicit assumption that astrocytic cells only provide information already encoded in neurons [120, 121]. Here, we challenged this assumption and tested the hypothesis that astrocytes encode information in their intracellular calcium dynamics that is not present in the activity of nearby neurons. As a model, we used spatial information encoding in the hippocampus, where neural place cells encode navigational information by modulating their firing rate as a function of the animal’s spatial location [122–124]. We demonstrate that astrocytic calcium signals encode information about the animal’s position in virtual space, and that, according to the statistical analysis we performed, this information is complementary to that carried by hippocampal neurons.

2.2 Results

We combined two-photon functional imaging in head-fixed mice navigating in virtual reality [123, 124] (Fig 2.1A) with astrocyte-specific expression of the genetically en-

coded calcium indicator GCaMP6f (Fig 2.1B, D, Fig. A.1) [57, 79, 85]. To control for potential reactivity of astrocytes, we stained against the glial fibrillary acidic protein (GFAP) sections of fixed tissue from animals implanted with the chronic hippocampal window (Fig. A.1). As internal controls, we used the contralateral non-implanted hemisphere from the same experimental animals. We quantified GFAP signals in implanted and control hemispheres in three regions: the Stratum Oriens, the Stratum Pyramidale, and the Stratum Radiatum. We found similar GFAP immunoreactivity in the Stratum Pyramidale and Radiatum in implanted hemispheres compared to controls (Fig. A.1 E, F). In contrast, we observed increased GFAP immunoreactivity in the Stratum Oriens in implanted hemispheres compared to controls (Fig. A.1 E, F). These results are in line with previous publications [125, 126], which reported no astrocyte reactivity in the Stratum Pyramidale, where imaging was performed, and some astrocyte reactivity in a small region in the Stratum Oriens close to the glass coverslip of the implant. We measured subcellular calcium dynamics of hippocampal CA1 astrocytes during spatial navigation in a virtual monodirectional corridor (Fig 2.1C) [127]. Using the intersection of two stringent criteria (significance of mutual information about spatial location carried by the cell’s activity, and reliability of calcium activity across running trials; Methods, Fig. A.2), we found that a large fraction of astrocytic regions of interest (ROIs) had calcium signals that were reliably modulated by the spatial position of the animal in the virtual track (44 ± 21 %, 155 out of 356 ROIs, from 7 imaging sessions on 3 animals, Fig 2.1E, App. A S1 Table, Fig. A.3). We defined the spatial response field of an astrocytic ROI as the portion of virtual corridor at which that ROI showed, on average across trials, increased GCaMP6f fluorescence (Methods). The distribution of astrocytic spatial response field positions covered the entire length of the virtual corridor (Fig 2.1F, G, $N = 155$ ROIs from 7 imaging sessions on 3 animals). The median width of the astrocytic spatial field was 56 ± 22 cm ($N = 155$ ROIs from 7 imaging sessions in 3 animals, Fig 2.1H). ROIs with reliable spatial information had reproducible estimates of spatial response profiles (Fig. A.3 B, C). Splitting the dataset in odd and even trials resulted in a similar distribution of astrocytic field position compared to the entire dataset (Fig 2.1F center and rightmost panels, Fig 2.1I). We computed spatial precision as in [128] and found that calcium responses in astrocytic ROIs encoding reliable spatial information were moderately more precise than their unmodulated counterpart (Fig. A.3 D; spatial precision, median \pm m.a.d. $3.2E-2 \pm 0.6E-2$, $N = 155$ out of 356 total ROIs, for ROIs with reliable spatial information; $3.0E-2 \pm 0.5E-2$ cm⁻¹, $N = 201$ out of 356 total ROIs, for not-modulated ROIs: $p = 3.8E-2$, Kolmogorov-Smirnov test; 7 imaging sessions on 3 animals). We computed response fields using running trials recorded either during the first or the second half of each experimental session. As in [128], we considered as stable those response fields showing an absolute difference in the estimated response field centers < 15 cm. We found that a fraction of astrocytic ROIs (10 ± 10 %, 35 out of 356 ROIs, from 7 sessions in 3 animals) encoded reliable spatial information and had stable response field. Moreover, we found that astrocytic calcium events were smaller when

the mouse was still vs. when the mouse was locomoting [86, 129], and, for spatially modulated ROIs, in the absence vs. presence of virtual reality (Fig. A.4 A, B).

Experiments performed with mice trained in a bidirectional virtual corridor (Fig. A.5) [123, 124] confirmed the results obtained in the monodirectional virtual corridor: a significant fraction of astrocytic ROIs carried significant information about the spatial position of the animal in the virtual corridor and the distribution of position of the astrocytic spatial field covered the whole virtual corridor ($29 \pm 13 \%$, $N = 192$ out of 648 ROIs in the forward direction; $20 \pm 13 \%$, $N = 133$ out of 648 ROIs in the backward direction, $p = 0.09$ Wilcoxon signed rank test for comparison between forward and backward directions, from 18 imaging sessions in 4 animals; Fig. A.5 E, F). The median width of the spatial response field was 44 ± 20 cm, $N = 192$ out of 648 ROIs in the forward direction and 44 ± 29 cm, $N = 133$ out of 648 ROIs in the backward direction ($p = 0.34$ Wilcoxon rank-sums test for comparison between forward and backward directions, Fig. A.5 G). In the bidirectional virtual corridor, astrocytic ROIs showed significant direction-selective spatial modulation in their response field (Fig. A.5 H). Thus, hippocampal astrocytic calcium signaling encoded spatial information.

Astrocytic calcium signaling has been shown to be organized at the subcellular level; the calcium dynamics of astrocytic cellular processes can be distinct from those occurring in the astrocytic cell body [58, 59, 92, 93, 118]. We thus categorized astrocytic ROIs (among the set of 356 described above) according to whether they were located within main processes (process-ROIs) or cell bodies (soma-ROIs, Fig 2.2). Signals from both soma-ROIs and process-ROIs encoded spatial information (Fig 2.2A). Moreover, a similar fraction of soma-ROIs and process-ROIs were modulated by the spatial position of the animal ($42 \pm 34 \%$, 19 out of 46 soma-ROIs vs $44 \pm 21 \%$, 136 out of 310 process-ROIs, $p = 0.61$ Wilcoxon signed-rank test, from 7 imaging sessions on 3 animals). The distribution of field position of soma-ROIs and process-ROIs similarly covered the entire length of the virtual corridor (Fig 2.2B, Fig. A.6 A, App. A S1 Table). The average width of the astrocytic spatial field did not differ between process-ROIs and soma-ROIs (Fig. A.6 B). Within individual astrocytes, the difference between the field position of a process-ROI and the corresponding soma-ROI (both containing reliable spatial information) increased as a function of the distance between the two ROIs (Fig 2.2C, Fig. A.6). Thus, spatial information was differentially encoded in topographically distinct locations of the same astrocyte. The difference between the field position of a process-ROI and the corresponding soma-ROI did not depend on the angular position of the process with respect to the soma (Fig. A.6). When comparing calcium activity across pairs of ROIs with reliable spatial information (belonging to processes or somas across astrocytes), correlation decreased as a function of the pair distance ($\tau_{\text{decay}} = 14 \pm 2 \mu\text{m}$, $R^2 = 0.98$) in the 0-50 μm range, and then substantially plateaued for pair distances between 50 μm and 160 μm (Fig 2.2F). This indicates that calcium signals encoding reliable spatial information were coordinated across distant ROIs, even those putatively belonging to different cells. In agreement with this observation, the difference

in field position among pairs of ROIs with reliable spatial information increased as a function of pair distance within 0-40 μm and then plateaued to a constant value ($\tau_{\text{rise}} = 13 \pm 7 \mu\text{m}$, $R^2 = 0.79$) for pair distances between 40-160 μm (Fig 2.2G). Event-triggered averages of astrocytic responses representing temporal relationships between calcium signals at different subcellular regions are shown in Fig. A.7.

Since calcium dynamics of individual astrocytic ROIs encodes significant spatial information, it should be possible to decode the animal's position in the virtual corridor from single-trial calcium dynamics of populations of astrocytic ROIs. We trained a Support Vector Machine (SVM) to classify the mouse's position according to a set of discrete spatial locations using a single-trial population vector made combining calcium signals of all individual astrocytic ROIs within the FOV. We computed the population decoding accuracy and the decoded spatial information [114] as a function of spatial granularity, i.e., the number of discrete locations available to the SVM decoder (4, 8, 12, 16, 20, or 24 locations). We found that the SVM predicted the animal's spatial location across granularities (Fig 2.3A, App. A S1 Table). Cross-validated decoding accuracy (Fig. A.8) and decoded spatial information were significantly above chance (Fig 2.3B) across the entire range of spatial granularities (chance level was estimated by decoding position after randomly shuffling spatial locations in the data while preserving the temporal structure of the population calcium signals, see Methods). Disrupting the within-trial temporal coupling within astrocytic population vectors while preserving single-ROI activity patterns [130, 131] consistently decreased decoded spatial information (Fig 2.3B) and decoding accuracy (Fig. A.8). This suggests that within-trial interactions among astrocytic ROIs encode spatial information not present in their individual activities. Misclassifications were more likely to happen among nearby locations across all granularity conditions (Fig 2.3C), consistent with the idea that astrocytic activity allows localization of the animal's position. Experiments performed with mice trained in a bidirectional virtual environment (Fig. A.9) largely confirmed these decoding results.

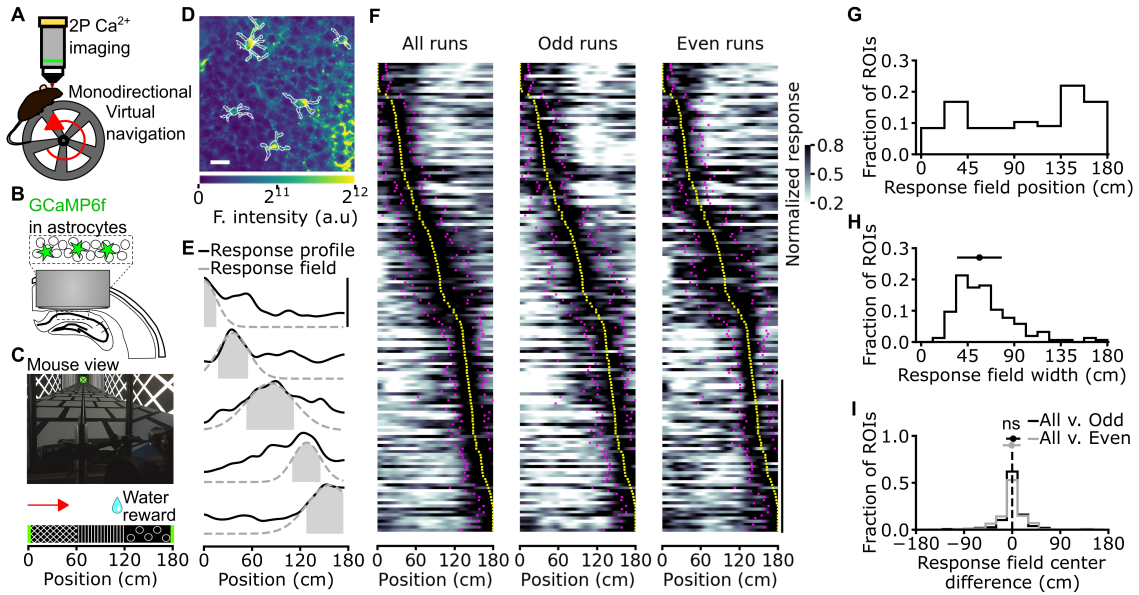


Figure 2.1: Astrocytic calcium signals in the CA1 hippocampal area encode spatial information during virtual navigation. (A) Two-photon fluorescence imaging was performed in head-fixed mice running along a monodirectional virtual track. (B) GCaMP6f was expressed in CA1 astrocytes and imaging was performed through a chronic optical window. (C) Mice navigated in a virtual linear corridor in one direction, receiving a water reward in the second half of the virtual corridor. (D) Median projection of GCaMP6f-labeled astrocytes in the CA1 pyramidal layer. Scale bar: $20\ \mu\text{m}$. (E) Calcium signals for five representative astrocytic ROIs encoding spatial information across the corridor length. Solid black lines indicate the average astrocytic calcium response across trials as a function of spatial position. Dashed grey lines and filled grey areas indicate Gaussian fitting function and response field width (see Methods), respectively (see also Fig. A.3). (F) Normalized astrocytic calcium responses as a function of position for astrocytic ROIs that contain significant spatial information ($n = 155$ ROIs with reliable spatial information out of 356 total ROIs, 7 imaging sessions from 3 animals). Responses are ordered according to the position of the center of the response field (from minimum to maximum). Left panel, astrocytic calcium responses from all trials. Center and right panels, astrocytic calcium responses from odd (center) or even (right) trials. Yellow dots indicate the center position of the response field, magenta dots indicate the extension of the field response (see Methods, vertical scale: 50 ROIs). (G) Distribution of response field position. (H) Distribution of field width. (I) Distribution of the differences between the center position of the response fields in cross-validated trials and odd trials (black) or cross-validated and even trails (grey). Deviations for odd and even trials are centered at 0 cm: median deviation for odd trials 2 ± 13 cm; median deviation for even trials -1 ± 17 cm, neither is significantly different from zero ($p = 0.07$ and $p = 0.69$, respectively, Wilcoxon signed-rank test with Bonferroni correction. $N = 155$ ROIs from 7 imaging sessions on 3 animals). The data presented in this figure can be found in the S1 Data archive.

Our virtual corridor was characterized by the alternation of three different patterns (grid, vertical lines, and circles) similarly to [123, 124, 128]. The three patterns covered the whole length of the virtual corridor (180 cm) and each pattern was presented for 60 cm of the corridor. Within each of these 60 cm-long visual cues, the visual stimuli associated with each pattern were periodically repeated (Fig 2.1C). Can the different visual cues account for the modulation of spatial information that we observed in astrocytes? We reasoned that if astrocytes responses in the virtual reality corridor were only modulated by visual cues regardless of the position in which the visual stimulus was provided, then astrocytes calcium responses should not have the power to discriminate between spatial locations within the 60 cm-long spatial interval in which a single visual cue was presented. In such case, the astrocytic responses would not carry spatial information above and beyond the one that is inherited from the information they carry about the identity of the visual cue. To test whether astrocytic signals carried spatial information that cannot be possibly attributed to visual cue modulation, we randomly shuffled the relationship between position and astrocytic signals within each visual cue. This data shuffling procedure preserves cue information carried by the astrocytes but destroys all the genuine spatial information they carry above and beyond visual cue information. The difference between the information carried by the real, unshuffled, responses and the information carried by the shuffled responses quantifies the amount of spatial position information carried by the astrocytes that cannot be possibly attributed to spatial cue tuning. Analyzing individual astrocytic ROIs (Fig 2.4A), we found that a large fraction (~ 50 to 60 %) of spatially modulated ROIs carried significantly more information than what could be solely explained by visual cue identity. Moreover, when decoding the animals' position from astrocytic population vectors (Fig 2.4B, C, Fig. A.10), we found that the majority (~ 55 to 65 %) of the decoded information was genuinely information about position. We performed both analyses dividing each visual cue in a number of spatial bins that was systematically varied from 3 to 6, leading to an overall spatial granularity varying from 9 to 18, and obtaining qualitatively similar results across granularities.

How does the astrocytic representation of spatial information relate to that of neuronal cells? We combined astrocyte-specific expression of GCaMP6f with neuronal expression of jRCaMP1a (Dana, Mohar et al. 2016) and performed simultaneous dual color hippocampal imaging with two-photon microscopy (Fig 2.5A, B, Fig. A.11) during virtual navigation. We found that a sizable fraction of astrocytic and neuronal ROIs (astrocytes, 22 ± 19 %, 76 out of 341 ROIs; neurons, 38 ± 13 %, 335 out of 870 ROIs, from 11 imaging sessions on 7 animals) reliably encoded information about the spatial position of the animal in the virtual corridor. For both astrocytes and neurons, the distribution of field position covered the entire length of the virtual corridor (Fig 2.5C, D). The median width of the astrocytic spatial field was statistically larger than that of neurons (Fig 2.5E, App. A S1 Table). Event triggered averages of astrocytic ROIs signals triggered by neuronal signals are shown in Fig. A.12. Both, neuronal and astrocytic calcium events were bigger when the

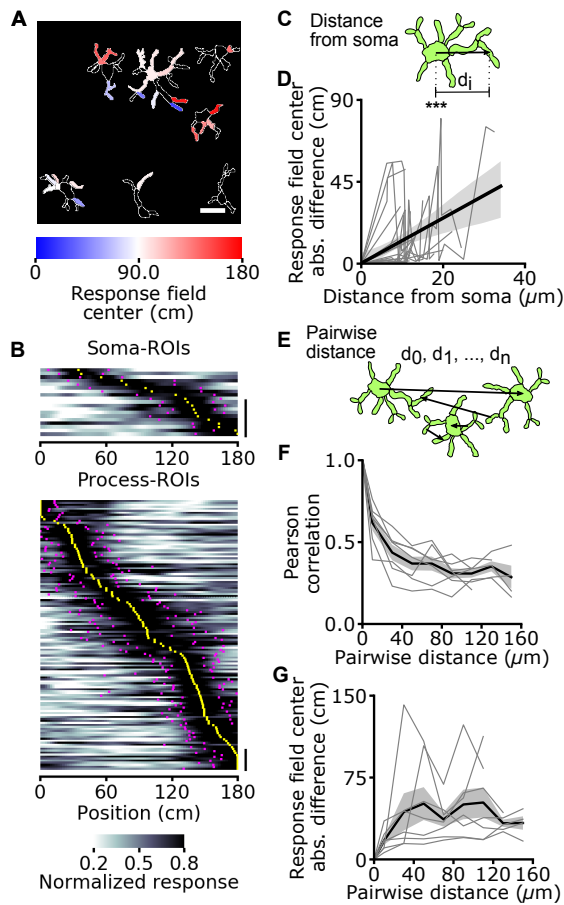


Figure 2.2: Topographic organization of spatial information encoding in astrocytes: somas vs processes. (A) Astrocytic ROIs in a representative FOV are color-coded according to response field position along the virtual corridor. Scale 20 μm . (B) Normalized astrocytic calcium responses as a function of position for astrocytic ROIs with reliable spatial information corresponding to somas (top) and processes (bottom) (somas: 19 ROIs with reliable spatial information out of 46 total ROIs; processes: 136 ROIs with reliable spatial information out of 310 total ROIs; data from 7 imaging sessions in 3 animals). Vertical scale: 10 ROIs. (C) Distance between the center of a process-ROI and corresponding soma-ROI computed for each astrocyte. (D) Absolute difference in response field position of a process-ROI with respect to the field position of the corresponding soma-ROI as a function of the distance between the two ($R^2 = 0.21$, $p = 3.2\text{E-}6$, Wald test, data from 19 cells in which there was significant spatial modulation in the soma and at least one process; 7 imaging sessions on 3 animals). (E) The distance between the centers of pairs of ROIs (d_0, d_1, \dots, d_n) is computed across recorded astrocytic ROIs. (F, G) Difference between response field position (G) and Pearson's correlation (F) for pairs of astrocytic ROIs containing reliable spatial information across the whole FOV as a function of pairwise ROI distance. Grey lines indicate single experiments, black line and the grey shade indicate mean \pm s.e.m, respectively. Data from 41 cells in which there was significant spatial modulation in at least one ROI; 7 imaging sessions in 3 animals. In this as well as in other figures: *, $p < 0.05$; **, $p \leq 0.01$; ***, $p \leq 0.001$. The data presented in this figure can be found in the S1 Data archive.

mouse was engaged in locomotion (Fig. A.13 A), and for spatially modulated ROIs in the presence vs. the absence of virtual reality (Fig. A.13 B). We then investigated the organization of astrocytic and neuronal spatial representations across the FOV. We found that calcium dynamics among mixed pairs of ROIs (one astrocytic ROI with reliable spatial information and one neuronal ROI with reliable spatial information) were significantly correlated (Fig. A.14), independent of pair distance (0-160 μm ; Fig 2.5F).

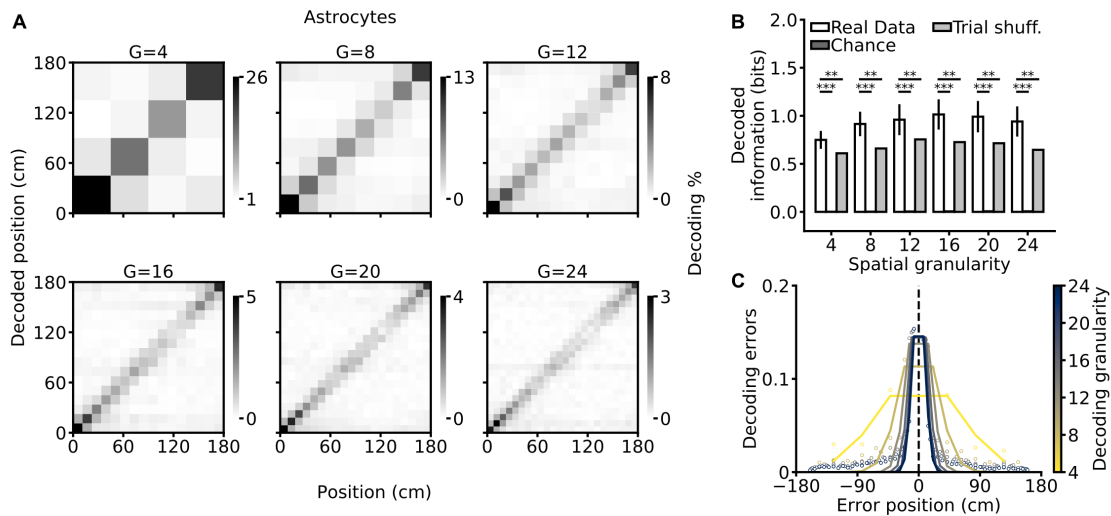


Figure 2.3: Efficient decoding of the animal’s spatial location from astrocytic calcium signals. (A) Confusion matrices of a SVM classifier for different decoding granularities ($G = 4, 8, 12, 16, 20, 24$). The actual position of the animal is shown on the x-axis, decoded position is on the y-axis. The grey scale indicates the number of events in each matrix element. (B) Decoded information as a function of decoding granularity on real (white), chance (dark grey), and trial-shuffled (grey) data (see Methods). Trial-shuffling disrupts temporal coupling within astrocytic population vectors while preserving single-ROI activity patterns. Data are shown as mean \pm s.e.m. See also App. A S2 Table. (C) Decoding error as a function of the error position within the confusion matrix. The color code indicates decoding granularity. Data in all panels were obtained from 7 imaging sessions in 3 animals. The data presented in this figure can be found in the S1 Data archive.

Correlation among pairs of astrocytic ROIs was generally higher than correlation among pairs of neuronal ROIs (Fig. A.14 2.14, Fig. A.15), even when we stratified the calculation of pairwise correlation for pairs of ROIs belonging to the same astrocyte and for pairs of ROIs belonging to different astrocytes (Fig. A.14). The difference in spatial field position of an astrocytic ROI with reliable spatial information and a neuronal ROI with reliable spatial information was also largely independent of pair distance (Fig 2.5G). We compared the spatial precision (Sheffield

and Dombeck 2015) of astrocytic responses with that of neuronal responses. We found that the responses of position-encoding neurons were more precise than the responses of simultaneously recorded position-encoding astrocytic ROIs (mean \pm s.e.m.; neuronal responses $7.5\text{E-}2 \pm 1.6\text{E-}2$; astrocytic responses $4.1\text{E-}2 \pm 0.2\text{E-}2$; $p = 4.6\text{E-}2$ Wilcoxon signed-rank test; 11 imaging sessions on 7 animals, Fig. A.16 A). We also compared astrocytic response field stability with neuronal place field stability. We found that similar fractions of astrocytic ROIs and neuronal cells encoded reliable spatial information and had stable response field (astrocytes, 8 ± 7 %, 29 out of 341 ROIs; neurons, 16 ± 9 %, 139 out of 870 ROIs; $p = 0.29$, Wilcoxon Rank-sum test; from 11 imaging sessions on 7 animals, Fig. A.16 B). Importantly, we also found that a large fraction of astrocytic and neuronal ROIs showing spatial modulation carried a significant amount of spatial information that could not be explained by visual cue tuning (Fig. A.17 A, B). Moreover, when analyzing population vectors using a support vector machine decoder, the majority (~ 60 to 80 %, Fig. A.18) of the total spatial information carried by either astrocytic or neuronal ROIs could not be possibly explained by visual cue modulation. Thus, the majority of spatial information in astrocytes and neurons is genuine spatial information that cannot be explained by tuning to visual cues.

We then quantitatively tested whether calcium dynamics in astrocytes and neurons carry the same or complementary information about space. We did so at the pairwise level using mutual information analysis (Quian Quiroga and Panzeri 2009) on all pairs of ROIs (either astrocytic, neuronal, or mixed pairs). Regardless of pair identity, we found that information carried by pairs of ROIs was greater than information carried by either ROI individually (Fig 2.6A, Fig. A.19). Moreover, information carried by pairs of ROIs was higher than the sum of the information carried by each of two ROIs, regardless of pair identity (Fig 2.6A, Fig. A.19, and App. A S1 Table). Thus, information carried by the pairs was also synergistic. To understand how correlations between ROIs leads to synergistic coding, we used mutual information breakdown analysis of ROI pairs [132, 133]. This revealed two notable results. First, the “signal-similarity” component of information (ISS), which quantifies the reduction of ROI pair information, or redundancy, due to the similarity of the trial-averaged response profiles of the individual ROIs (see Methods and Fig. A.20), was close to zero. Thus, the diversity of spatial profiles allowed ROIs to sum up their information with essentially no redundancy. Second, synergy between elements of pairs was based on a positive stimulus-dependent correlation component (ICD, see Methods and Fig. A.20), which contributed to increase the joint information. Mathematically, ICD can be non-zero if and only if within-trial correlations between ROIs are modulated by the animal’s position and they carry information complementary to that given by position modulation of each individual ROI [132]. Correlation enhancement of spatial information was found in a sizeable fraction of pairs across all pair identities, including mixed pairs (Fig 2.6B). This was because the strength of correlations between neurons and astrocytes marked the position in virtual corridor: for pairs of one neuronal ROI and one astrocytic ROI, the

absolute magnitude of correlations showed a position-dependent modulation (Fig. A.21), with stronger correlations inside the spatial fields.

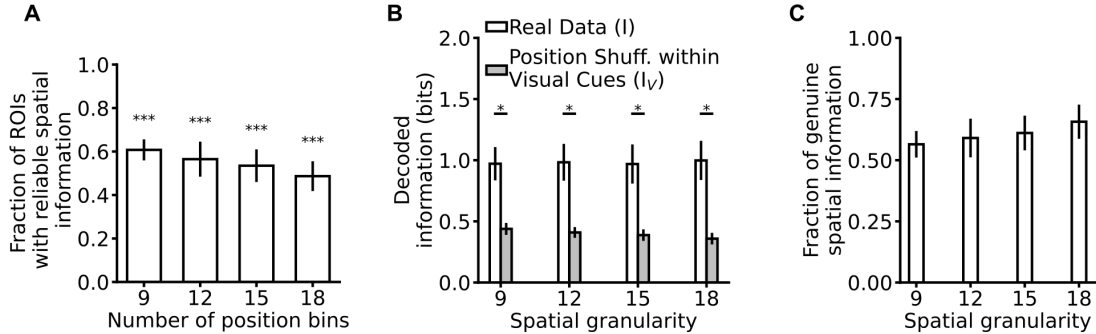


Figure 2.4: The majority of spatial information in astrocytes is genuine spatial information that cannot be explained by tuning to visual cues. (A) Fraction of astrocytic ROIs encoding reliable spatial information showing a significant decrease in their information content when position is shuffled within the same visual cue (see Methods). Shuffling position within the same visual cue decouples spatial information encoded in the astrocytic response from the information related to visual cues identity (see Methods). The fraction of ROIs showing significant information loss is shown as function of the number of position bins used to compute mutual information. $p = 3.5\text{E-}168$, $p = 3.2\text{E-}138$, $p = 5.0\text{E-}133$, and $p = 5.2\text{E-}85$ for 9, 12, 15, and 18 position bins, respectively; $N = 155$, Binomial test. (B) Decoded information as a function of decoding granularity on real data (I, white) and for data in which position is shuffled within the same visual cue (IV, grey). $p = 1.6\text{E-}2$, $p = 1.6\text{E-}2$, $p = 1.6\text{E-}2$, and $p = 1.6\text{E-}2$ for decoding granularity of 9, 12, 15, and 18, respectively. $N = 7$ imaging sessions, Wilcoxon Signed rank test. See also Fig. A.10. (C) Fraction of genuine spatial information in astrocytic population vectors computed shuffling position within individual visual cues. Results are shown as a function of decoding granularity. In all panels, data are shown as mean \pm s.e.m. and were obtained from 7 imaging sessions in 3 animals. The data presented in this figure can be found in the S1 Data archive.

Complementary and synergistic spatial information encoding in mixed pairs suggested that the network of astrocytes that we imaged carried spatial information that was not found in the imaged neurons and in their interactions. To directly address this hypothesis, we computed the spatial information gained by decoding the animals' position from an SVM operating on population vectors comprising either all neuronal, all astrocytic, or all ROIs of both types. We found that neuronal, astrocytic, and mixed population vectors allowed to classify the animal's position across granularity conditions (Fig 2.6C-E and Fig. A.22). However, decoding population vectors comprising both astrocytic and neuronal ROIs led to a greater amount of spatial information than decoding either neuronal or astrocytic population vectors separately (Fig 2.6D). This result supports the hypothesis that the population of astrocytic ROIs encodes information not found in neurons or their interactions. In

agreement with what we found in the pair analysis, information decoded from all types of population vectors decreased when within-trial temporal correlations between cells were disrupted by trial shuffling (Fig 2.6E, Fig. A.22) (Pola, Thiele et al. 2003, Runyan, Piasini et al. 2017). Within-trial correlations were thus an important factor for the complementary and synergistic contribution of astrocytes to spatial information encoding at the population level.

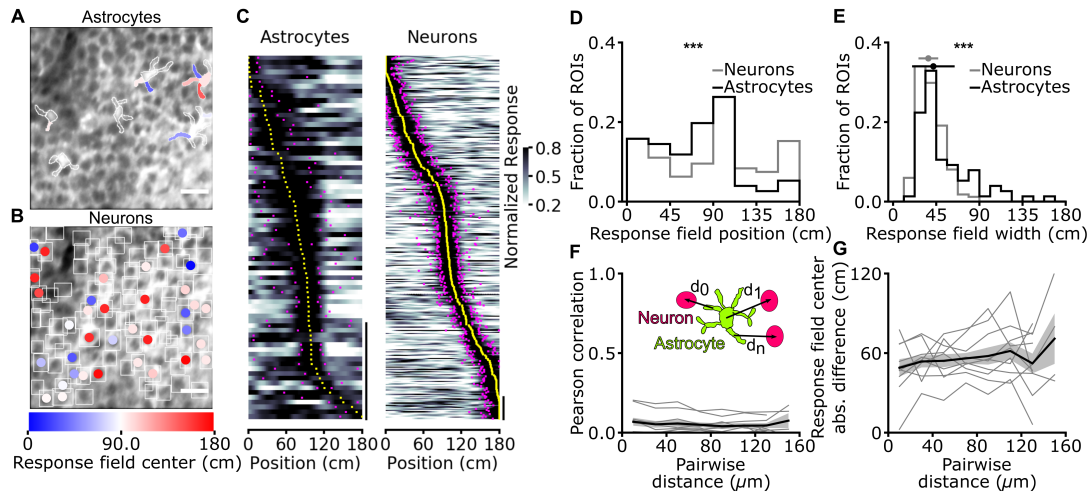


Figure 2.5: Astrocytes have broader response field width and a different distribution of field position compared to neurons. (A, B) ROIs corresponding to simultaneously recorded GCaMP6f-labeled astrocytes (A) and jRCaMP1a-labeled neurons (B) in the CA1 pyramidal layer. ROIs are color-coded according to response field and place field center along the virtual corridor, respectively. Scale bar, 20 μm . (C) Normalized calcium responses as a function of position for astrocytic ROIs (left) and neuronal ROIs (right) that contain a significant amount of spatial information (astrocytic ROIs, $N = 76$ ROIs with reliable spatial information out of 341 total ROIs; neuronal ROIs, $N = 335$ ROIs with reliable spatial information out of 870 total ROIs, data from 11 imaging sessions in 7 animals). Responses are ordered according to the position of the center of the response field for astrocytes and place field for neurons. Vertical scale bar, 20 ROIs. (D) Distribution of astrocytic response field position (black line) and neuronal place field position (grey line, $p = 5\text{E-}4$, Kolmogorov-Smirnov test for comparison between astrocytic and neuronal distribution). (E) Distribution of astrocytic response field width (black line) and neuronal place field width (grey line, median width of astrocytic response field: 42 ± 22 cm, $N = 76$; median width of neuronal place field: 37 ± 10 cm, $N = 335$, $p = 2\text{E-}5$, Wilcoxon Rank-sum test for comparison between astrocytic and neuronal distribution). (F, G) The inset shows astrocytic ROIs (green) and neuronal ROIs (pink). For all pairs, the distance (d_0 , d_1 , d_n) between the center of an astrocytic ROI and the center of a neuronal ROI, both containing reliable spatial information, is computed. Pairwise Pearson's correlation (F) and difference between response field position for astrocyte-neuron ROI pairs (G) as a function of pair distance. Data are from 11 imaging sessions in 7 animals (see also Fig. A.15). The data presented in this figure can be found in the S1 Data archive.

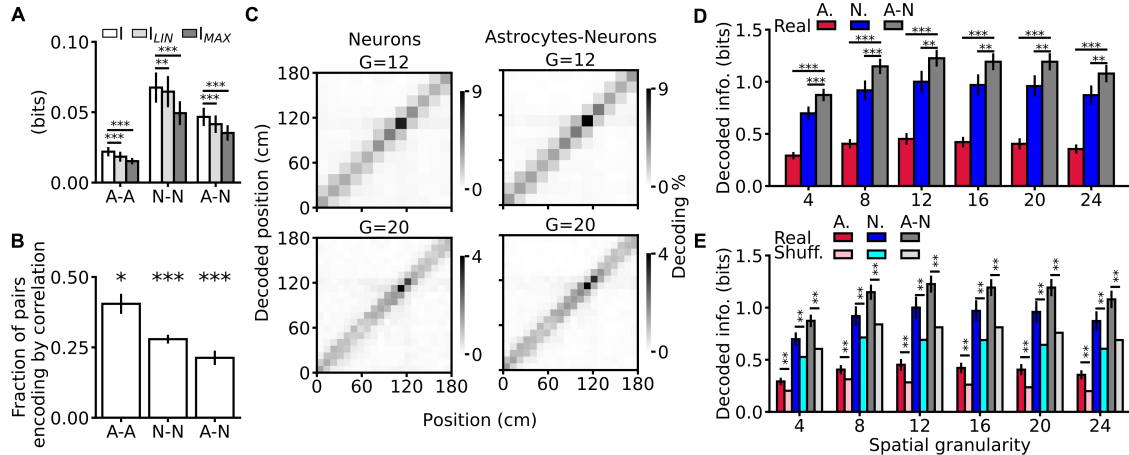


Figure 2.6: Spatial information encoding in astrocytes is complementary and synergistic to spatial information encoding in neurons. (A) Information about position carried by pairs of ROIs (I) compared to the sum (ILIN) or the maximum (IMAX) of the information separately encoded by each member of the pair. A-A, pair composed of two astrocytic ROIs; N-N, pair composed of two neuronal ROIs; A-N, mixed pair composed of one astrocytic and one neuronal ROI (I vs. ILIN: A-A: $p = 1E-3$, N-N: $p = 5E-3$, A-N: $p = 1E-3$; I vs. IMAX: A-A: $p = 1E-3$, N-N: $p = 1E-3$, A-N: $p = 1E-3$, Wilcoxon signed-rank test, see also Fig. A.19 and App. A S3 Table). (B) Fraction of pairs encoding spatial information encoding by correlations (A-A: $p = 3E-2$, N-N: $p = 1E-3$, A-N: $p = 1E-3$, Wilcoxon signed rank-test with respect to the null hypothesis that a pair could be either synergistic or non-synergistic with equal probability set at 0.5). (C) Representative confusion matrices of a SVM classifier decoding mouse position using population vectors comprising neuronal (left) or astrocytic and neuronal ROIs (right), for different decoding granularities ($G = 12, 20$, see also Fig. A.21). (D) Decoded information for population vectors of different compositions (A, astrocytic ROIs only; N, neuronal ROIs only; A-N, population vector considering all ROIs) as a function of decoding granularity (see App. A S4 Table). (E) Same as in (D) but adding comparison with trial-shuffled data (lighter bars) (see App. A S5 Table). In panels A-B, D-E data are represented as mean \pm s.e.m. In all panels, data are obtained from 11 imaging sessions in 7 animals. The data presented in this figure can be found in the S1 Data archive.

2.3 Discussion

Our findings demonstrate, for the first time, that information-encoding cellular signals during virtual spatial cognition extend beyond neuronal circuits to include the nearby astrocytic network. This information was expressed in spatially-restricted subcellular regions, including cellular processes and somas, in agreement with previous work describing the complexity and compartmentalization of calcium signals in these glial cells [59, 75, 92, 93, 98, 118]. Importantly, individual astrocytes could encode multiple spatial fields across different subcellular compartments, suggesting that a single astrocyte may integrate multiple neuronal spatial representations.

Interestingly, the spatial representations in individual astrocytes displayed a concentric organization: the difference between the place field position of a subcellular process and the place field position of the corresponding soma increases as a function of distance. Most importantly, combining astrocytic and neuronal signals generated significantly greater information about the animal's position, suggesting the signals are both complementary and synergistic. The complementary and synergistic information of astrocytes relied both on the diversity of position tuning and on position-dependent correlations among astrocytic and neuronal ROIs similarly to what observed on neuronal ROIs by (Stefanini, Kushnir et al. 2020). It should also be considered that astrocytic signals may convey complementary information by simultaneously integrating the activity of several different neuronal inputs encoding distinct stimulus-related variables (McNaughton, Barnes et al. 1983, Gauthier and Tank 2018, Gois and Tort 2018).

Since the seminal observations of Cornell-Bell et al. [4] and Charles et al. [70], it has been shown that astrocytic calcium signaling can be activated by the extracellular increase in the concentration of neuroactive molecules [76, 134]. The source of the observed calcium signaling has long been investigated and there is evidence of both release from intracellular organelles (e.g., endoplasmic reticulum and mitochondria, [6, 117] and direct calcium influx through the astrocytic plasma membrane [135]. Moreover, while neuronal activity induces membrane depolarization in astrocytes, these depolarizations are small (a few millivolts in maximal amplitude), at least at the level of the astrocytic somata [93, 136, 137]. Pharmacological studies demonstrated that these membrane potential depolarizations are mediated mostly by K^+ conductances and transporters-mediated currents [138]. For neuronal activity-induced calcium signals, a largely accepted model [134, 139] is thus that spillover of neurotransmitter release at the synaptic cleft activates receptors in the plasma membrane of astrocytic processes, which enwrap the pre- and the post-synaptic terminals. Activation of astrocytic receptors then causes the mobilization of intracellular calcium signaling. Within this framework, it is interesting to note that previous studies *in vivo* showed that calcium dynamics into astrocytes largely mirror the activity of nearby neurons [46, 58, 109]. The information theoretic approach we used in the present study instead shows that spatial information encoded in astrocytes is complementary to that encoded by nearby neurons. This observation raises a series of questions about the molecular, anatomical, and network mechanisms that may generate the observed information complementarity. Can complementarity be generated by differences in the diffusion of pre-synaptically released neurotransmitter that reaches postsynaptic neuronal terminals in the synaptic cleft vs. thin astrocytic processes outside the cleft? Are the different molecular mechanisms regulating intracellular signaling in neurons and astrocytes accountable for the observed information complementarity? Additionally, can information complementarity stem from astrocytes integrating spatial information from different sets (or different combinations) of pre-synaptic terminals compared to post-synaptic neurons? Our work does not directly address the questions raised above and future studies combining

experimental and modeling work will be fundamental to tackle these questions. It is important to note that demonstrating by statistical analysis of cell activity, as we did here, that astrocytes carry complementary spatial information is not sufficient to demonstrate that this information is causal to circuit function or behavior. Experimental manipulations targeted to either astrocytes or neurons must be used to establish causality [140]. To this aim, it will thus be necessary to perturb hippocampal astrocytic and neuronal networks with high spatial and temporal resolution [141–143] while monitoring downstream effects on circuit functions and behavior.

Models of hippocampal function posit that information about variables of the external environment, which are key to spatial navigation and memory, is exclusively encoded in population of neurons [144–147]. Our results challenge this established view by revealing a fundamental new level of organization for information encoding in the hippocampus during virtual navigation: spatial information, which according to the information theoretical analysis used in this study is not available in the activity of CA1 projecting neuron or in their interactions, is encoded in the calcium dynamics of local non-neuronal elements and in their position-dependent interaction with neurons. The presence of this additional non-neural reservoir of information and the dependence of the interaction between neuron and astrocytes on key cognitive variables suggest the possible presence of novel and unexpected cellular mechanisms underlying how brain circuits encode information.

Can complementary spatial information encoded in astrocytic calcium dynamics contribute to neuronal computation? If so, how? Although our data do not address these questions, previous work in other brain regions reported that astrocytic calcium dynamics largely mirror the activity of nearby neurons [46, 58, 109] and that astrocytic signals translate into changes in neuronal excitability and synaptic transmission through various mechanisms (reviewed in [53, 76, 148, 149]). In this scenario, changes in synaptic transmission and neuronal excitability induced by astrocytic calcium dynamics that simply mirror neuronal information would only modulate neural activity without providing further information, as all the activity-dependent information is already encoded in the neuronal activity. For example, if the neuronal tuning curve and the astrocytic-induced change in neural function are similarly modulated by the animal’s position, no additional dependence of neuronal function by position would be introduced by astrocyte-neuron interactions. Conversely, our findings suggest that astrocytic calcium dynamics carrying complementary information to that of neurons enable modulations of synaptic transmission and neuronal gain which could increase the computational capability of neural circuits [150, 151]. For example, changing the gain of neurons with a coordinate system complementary to that regulating its tuning function has been shown to endow neural networks with richer computations [150, 152]. Moreover, targeted dynamic control of neural excitability (e.g., changing the gain of a subset of neurons in the network rather than the whole network) can greatly increase the dynamic repertoire and coding capabilities of circuits, for example by making it possible to reach different attractors from a similar set of initial conditions [153]. We thus propose

that the complementary place-dependence of the astrocytic calcium dynamics and the place-dependence of astrocytic-neuron interactions reported here facilitate the emergence of dynamic, context-dependent changes in population coding of CA1 neurons. Within this scenario, local neuromodulation of the space-encoding properties of projecting CA1 neurons by astrocytes could affect hippocampal output. Future experiments involving selective perturbation (e.g., activation or inactivation) of astrocytic calcium signaling will be needed to test this hypothesis. Our work calls for a re-examination of the theory of place coding and of brain population codes in light of the opportunities offered by the suggested complementary astrocytic information coding. We propose that the complementary regulation of astrocytic calcium activity and of its interaction with neurons may reflect a general principle of how the brain encodes information. This conclusion may extend beyond the hippocampus and spatial navigation to other brain regions and cognitive tasks and it will need to be included in the conceptualization of brain function.

2.4 Methods

Data analysis

Motion correction, image segmentation, and trace extraction Analysis was performed using Python 3.6 (python.org) and custom code. t-series were pre-processed to correct motion artifacts using an open-source implementation of up-sampled phase cross-correlation [154, 155]. Each t-series was motion corrected using its median projection as reference frame. Corrected t-series were then concatenated in a single movie and, to compensate small x-y drifts across t-series, motion corrected using its median projection image as the reference frame. Regions (typically at the edges of the field of view) within which artifacts could not be corrected were not considered for analysis.

For astrocytic recordings, ROI segmentation was performed on median projections after motion correction using manual annotation. Astrocytic ROIs were classified as soma or process according to visible anatomic features. For each ROI, fluorescence signals were computed as:

$$\frac{\Delta F}{F_0} = \frac{F(t) - F_0(t)}{F_0(t)} \quad (2.1)$$

where $F(t)$ is the average fluorescence signal of a given ROI at time t , and $F_0(t)$ is the baseline fluorescence, computed as the 20th percentile of the average fluorescence intensity in a 30 s-long rolling window centered in t .

For neuronal recordings, cell identification was performed on the median temporal projection of each t-series, after motion correction, by identifying rectangular boxes containing the neuronal soma of the identified neuron, as in [156]. Within the rectangular box, pixels were ranked according to the pixel signal-to-noise (SNR)

using the following formula:

$$SNR_{i,j} = \frac{\max_{i,j} F_{i,j}(t)}{\text{noise}_{i,j}} \quad (2.2)$$

where $\max_{i,j} F_{i,j}(t)$ is the maximum fluorescence intensity of the pixel i,j , at time t and $\text{noise}_{i,j}$ was computed as the standard deviation across all fluorescence values of the t -series below the 25th percentile of the fluorescence distribution of the pixel i,j [156]. Only pixels with SNR value greater than the 80th percentile of the SNR distribution were considered as part of the ROI corresponding to the considered rectangular box. The neuropil signal was computed as the average trace of all pixels in the time series not belonging to bounding boxes. This value was multiplied by a factor $r = 0.7$ [79] and then subtracted from each fluorescence trace. $\Delta F/F_0$ traces were computed as:

$$\frac{\Delta F}{F_0} = \frac{F(t) - F_0(t)}{F_0(t)} \quad (2.3)$$

where $F(t)$ is the neuropil-subtracted fluorescence trace signal at time t , and $F_0(t)$ is the baseline trace computed as 20th percentile of the average intensities in a 10 s rolling window centered in t .

Identification of calcium events For both astrocytic and neuronal fluorescence traces, extraction of statistically significant calcium events was performed on $\Delta F/F_0$ traces via modified implementation of the algorithm described in [129]). In brief, for each trace, a first parameter (σ_1) was computed as the standard deviation of the whole signal. Values crossing the threshold set at $\pm \sigma_1$ were removed from the trace and a second parameter (σ_2) was computed as the standard deviation of the thresholded trace. This procedure avoided biases induced by large signal transients on the estimation of the signal standard deviation in the absence of transients and provided a better estimation of signal baseline fluctuations (σ_2). For astrocytic traces, fluorescence transients were identified on the original trace (thus considering all data) as events that: i) crossed the threshold of $\pm 2\sigma_2$; ii) returned within $\pm \sigma_2$ in more than 0.5 [129]). For both astrocytic and neuronal signals, these criteria were selected to obtain a false discovery rate $\leq 5\%$, according to the following:

$$FDR = \frac{N_{En}}{N_{Ep} + N_{En}} \quad (2.4)$$

where N_{Ep} and N_{En} are the numbers of identified positive and negative deflections of the $\Delta F/F_0$ trace, respectively. For all subsequent analysis, an event trace was obtained from the $\Delta F/F_0$ trace by setting all fluorescence values outside of those belonging to positive events to 0.

Identification of reliable spatial modulation of calcium signals To evaluate if and how position in the virtual corridor modulated calcium signals, we applied

two basic requirements: that activity carried significant information about position, and that the spatial modulation properties were reliably reproducible across subsets of trials. We restricted the analysis to running-trials, defined as consecutive frames of forward locomotion in which mouse speed was greater than 1 cm/s. Running-trials separated by less than 1 s were merged. The average number of running-trials per experimental session was 32 ± 3 trials/session ($N = 18$ experimental sessions) for unidirectional experiments and 30 ± 3 trials/session ($N = 18$ experimental sessions) for bidirectional experiments. Unidirectional running-trials were on average longer than bidirectional ones (mean running-trial length for unidirectional virtual navigation, 140 ± 3 cm, $N = 18$; mean running-trial length for bidirectional virtual navigation: 49 ± 4 cm, $N = 18$). Calcium responses were considered with reliable spatial information if they matched both of the following criteria: i) response field reliability was greater than 0 (see Spatial reliability of calcium responses); and ii) mutual information between position and calcium event trace was significant (see Spatial information in calcium signals). The same criteria were applied to astrocytic ROIs and neuronal ROIs.

Analysis of calcium responses during virtual navigation Analysis was performed on all running-trials, binning the length of the virtual corridor (number of spatial bins, 80; bin width, 2.25 cm). For each ROI, the occupancy map was built by computing the total amount of time spent in each spatial bin. The activity map was computed as the average fluorescence value in each spatial bin. Both the activity map and the occupancy map were normalized to sum 1 and convolved with a Gaussian kernel (width of the Gaussian, σ , was equal to 3 spatial bins, which corresponded to 6.75 cm). The response profile of an ROI, RP, was defined as the ratio of the activity map over the occupancy map for that ROI. For each RP, we identified a response field, RF, as follows: i) the array of local maxima greater than the 25th percentile of the response profile values was selected, $C = (c_0, c_1, \dots, c_n)$; ii) the elements of C were used to initialize the fitting of the sum of a set of n parametrized Gaussian functions, with mean at one of the elements of C , amplitude (a) at $0 \leq a \leq 1$, and standard deviation (σ) at $0 \leq \sigma \leq 90$ cm; iii) this set of Gaussian functions was fitted to the response profile to solve a non-linear least squares problem (curve-fit function from (Virtanen, Gommers et al. 2020)); and iv) the response field was defined as the Gaussian with the highest amplitude and the response field width was defined as $2\sigma_i$. Thus:

$$RP \simeq \sum_{c_i \in C} a_i e^{-\frac{(x-c_i)^2}{2\sigma_i^2}} \text{ with } \begin{cases} 0 \leq c_i \leq 180\text{cm} & \forall c_i \in C \\ 0 \leq a_i \leq 1 & \forall a_i \in A \\ 0 \leq \sigma_i \leq 90\text{cm} & \forall \sigma_i \in S \end{cases} \quad (2.5)$$

$$RF = a_i e^{-\frac{(x-c_i)^2}{2\sigma_i^2}} \text{ with } i = \text{argmax}(A) \quad (2.6)$$

Reliability and stability of calcium spatial responses To quantify spatial reliability of response fields, we computed response profiles subsampling either odd

or even running-trials. For either fraction of running-trials we estimated response field center (c_{odd} , c_{even}) and response field half-width (σ_{odd} , σ_{even}). We quantified spatial reliability of calcium responses as a similarity index, where the absolute difference of response field centers, obtained with either fractions of the running-trials, was inversely weighted by the most conservative estimate of response field width:

$$Reliability - 1 - \frac{|c_{odd} - c_{even}|}{2min(\sigma_{odd}, \sigma_{even})} \quad (2.7)$$

ROIs with reliability greater than 0 were considered reliable (Fig. A.2). To classify response field stability, we computed response profiles subsampling running trials recorded either in the first (h1) or the second (h2) half of the experimental session. For either half of the trials, we computed response field center (ch1, ch2). ROIs with an absolute difference in response field centers smaller than 15 cm were considered stable (Sheffield and Dombeck 2015).

Spatial information in calcium signals We used information theory to quantify our information gain (or reduction of uncertainty) about position obtained by knowing the calcium response [113, 114]. We computed the mutual information, $I(\mathbf{S};\mathbf{R})$, between position in the linear track, stimulus (\mathbf{S}), and the calcium event trace, response (\mathbf{R}), as follows:

$$I(\mathbf{R}; \mathbf{S}) = \sum_s p(s) \sum_r p(r|s) \log_2 \frac{P(r|s)}{P(r)} \quad (2.8)$$

with \mathbf{S} and \mathbf{R} representing the arrays of all possible discrete values of stimulus or response, $p(s)$ the probability of the stimulus s , $p(r)$ the probability of the response r across all trials to any stimulus, and $p(r|s)$ the conditional probability of the responses r given presentation of stimulus s . We characterized the effects of discretization on the estimates of mutual information, computing mutual information while changing the number of discrete states (N) for both \mathbf{S} ($N_S = 4, 8, 12, 16, 20, 24, 40, 60, 80, 100, 160$) and \mathbf{R} ($N_R = 2, 3, 4, 5, 8, 10, 20$). For the stimulus we used a uniform count binning procedure and for the response we used equally spaced bins. Statistical significance of mutual information was tested using a non-parametric permutation test. We randomly permuted the calcium event trace 104 times, removing any relationship between \mathbf{R} and \mathbf{S} . We used shuffled traces to compute a null distribution of mutual information values. A mutual information value was considered significant if greater than the 95th percentile of the null distribution. Mutual information values were conservatively corrected for limited-sampling bias subtracting the mean value of the null distribution [157, 158]. The results of this analysis for astrocytic ROIs are reported in Fig. A.2. To allow robust estimates of mutual information values while preserving adequately fine discretization of position, we used $N_s = 12$ throughout the manuscript. For single ROIs analysis reported in figures Fig 2.1, Fig 2.2, and Fig 2.5, we used $N_R = 4$ to discretize astrocytic cal-

cium event traces and $NR = 2$ for binarized neuronal event traces (setting to 1 all the non-zero values as in (Ziv, Burns et al. 2013)).

Response profile standard error A Jackknife estimator [159, 160] of the astrocytic response profile - RP - was computed as the average of n-Jackknife samples obtained by iteratively omitting one running-trial from the computation. We used this deterministic approach to compute Jackknife standard error (SE) as a function of ROIs spatial modulation (Fig. A.3).

$$RP = \frac{1}{n} \sum_{i=1}^n RP_i \quad \text{with } i = 1, \dots, n \quad (2.9)$$

and

$$SE = \sqrt{\frac{n-1}{n} \frac{1}{n} \sum_{i=1}^n (RP_i - RP)^2} \quad (2.10)$$

For each ROI, we measured the difference between the response field center computed using the Jackknife estimator of the RP and the response profiles computed using either odd or even running-trials (Fig 2.1I).

Spatial precision of calcium responses During monodirectional virtual navigation, we measured the spatial precision of calcium responses (SP) with the method reported in (Sheffield and Dombek 2015). For each ROI reliably encoding spatial information, we binned the length of the virtual corridor in m bins ($m = 40$; bin width, 4.5 cm) and for each running trial (n) we calculated the center of mass (COM_n) of the calcium response (Eq. 11), where DF_i is the value of the event trace observed in the i-th bin and x_i is the center of the i-th bin. For each ROI, we then computed the average center of mass across N trials (COM_w, Eq. 12), weighting each COM_n by the peak amplitude of the event trace during the n-th running trial (A_n). Spatial precision was computed as the inverse of the trial-by-trial squared difference between COM_n and COM_w weighed by peak amplitude (Eq. 13).

$$COM_n = \frac{\sum_m^i DF_i x_i}{\sum_m^i DF_i} \quad (2.11)$$

$$COM_w = \frac{\sum_N^n COM_n A_n}{\sum_N^n A_n} \quad (2.12)$$

$$SP = \left(\sqrt{\frac{\sum_N^n (COM_n - COM_w)^2}{\sum_N^n A_n}} \right)^{-1} \quad (2.13)$$

When comparing spatial precision of astrocytic and neuronal responses (Fig. A.16), we corrected for the different dynamic range (DR) of the two genetically encoded calcium indicators. For each imaging session, we estimated DRA and DRN

as the mean DR for astrocytic and neuronal event traces, respectively (mean \pm s.e.m; DRA = 0.95 ± 0.13 for 76 astrocytic ROIs expressing GCaMP6f; DRN = 0.54 ± 0.06 for 335 neuronal ROIs expressing jRCaMP1a; data from 11 imaging sessions from 7 animals). We corrected spatial precision of neuronal responses in each imaging session by the factor DRA /DRN.

Directionality of astrocytic spatial responses In experiments where the mouse performed bidirectional navigation, astrocytic ROIs could be spatially-modulated in either running direction. To quantify whether responses were direction selective, we computed the directionality index (DI) as:

$$DI = \frac{F_d - F_o}{F_d + F_o} \quad (2.14)$$

where F_d was the average of $\Delta F/F_0$ inside the response field, and F_o was the average of $\Delta F/F_0$ at the same response field while running in the opposite direction. DI ≥ 0 indicated that average response at the response field was direction-selective. We compared the distribution of DI values for all spatially-modulated ROIs with surrogate data. To this end, we randomly selected one of the informative ROIs and computed DI after applying a random shift of response field position along the linear track while preserving its width. We repeated this operation 105 times, obtaining a distribution of DI values representing the occurrence of DI values at any spatial location as wide as a response field.

Population analysis using Mutual Information For experiments in which we simultaneously recorded astrocytic and neuronal calcium activity, we used all running-trials to compute the mutual information about animals' position obtained by observing the calcium signals of a pair of simultaneously recorded ROIs. Results are reported as a function of pair composition, with pairs containing either two astrocytic ROIs, two neuronal ROIs, or one element of each type. Mutual information between the spatial position, S , and the array of joint responses for a pair of ROIs, $\mathbf{R} = (R_1, R_2)$, was computed as (Pola, Thiele et al. 2003):

$$I(\mathbf{R}; \mathbf{S}) = \sum_s p(r_1, r_2) \sum_r P(r_1, r_2|s) \log_2 \frac{P(r_1, r_2|s)}{P(s)} \quad (2.15)$$

where $p(s)$ is the probability stimulus s , $p(r_1, r_2)$ is the probability of joint responses r_1 and r_2 across all trials to any stimulus, and $p(r_1, r_2|s)$ is the conditional probability of the joint responses r_1 and r_2 given presentation of stimulus s . For consistency with single-ROI analysis, spatial position was discretized with $N_s = 12$. To allow consistent scaling of probability spaces and comparable information values, the astrocytic calcium event trace was binned with $NR = 2$ (we verified that the main conclusions were maintained when using $NR = 3$ and $NR = 4$), and $NR = 2$ for neuronal calcium event trace discretization, as described for single neuron analysis.

To correct mutual information bias caused by limited sampling of astrocytic or neuronal responses, we performed quadratic extrapolation correction [133, 161] using 100 iterations. To quantify whether the within-trial correlations of a given ROI pair enhanced the amount of position information carried by the pair, we used trial-shuffling to disrupt the within-trial correlations between ROIs while keeping intact the spatial position information of individual ROIs. Within subsets of trials with the same position bin, we generated pseudo-population responses by independently combining shuffled identities of trials for each ROI. Thus, responses of individual ROIs to the spatial position were maintained while within-trial correlations between ROIs were disrupted. We computed 100 trial-shuffling estimates of mutual information, $I(\mathbf{S};\mathbf{R})_{\text{trial-shuffled}}$, for calcium responses at fixed position. A pair was classified as having information enhanced by correlations, if $I(\mathbf{S};\mathbf{R})$ was greater than the 95th percentile of the corresponding $I(\mathbf{S};\mathbf{R})_{\text{trial-shuffled}}$ distribution.

Information Breakdown We performed information breakdown analysis [132, 133]. We decomposed spatial information carried by a pair of ROIs, $I(\mathbf{S};\mathbf{R})$, into 4 terms. Each term expressed a different contribution carried by correlations to the information between the ROIs. The decomposition is as follows:

$$I(\mathbf{R}; \mathbf{S}) = I_{LIN} + I_{SS} + I_{CI} + I_{CD} \quad (2.16)$$

ILIN, the mutual information linear term, is the sum of the information provided by each ROI. ISS (signal similarity term) is a non-positive term quantifying the decrease of information (amount of redundancy) due to signals correlation caused by correlations between the trial-averaged spatial position profiles of the calcium signals of the two ROIs. ICI (stimulus independent correlation) is a term that can be either positive, null, or negative and that quantifies the contribution of stimulus-independent correlations. ICI is negative if noise and signal correlations have the same signs and positive otherwise. ICD (stimulus-dependent correlational term) is a non-negative term that quantifies the amount of information, above and beyond that carried by the responses of individual ROIs carried by stimulus modulation of noise correlation strength. Although ICD is strictly non-negative, ICD values could occasionally become slightly negative due to quadratic extrapolation bias correction. The above calculations of $I(\mathbf{S};\mathbf{R})$ were conducted with a bias correction procedure that, with the typical number of trials per spatial location represented in our data (mean \pm s.e.m. 72 ± 7 trials/location), was shown to be accurate for removing the limited sampling bias [162]. However, it was also shown to leave on average, a small residual positive overestimation that tended to slightly over-estimate synergy [162]. To make sure that our results of prevalent synergy could not be explained by a residual positive bias, we repeated the calculation with the bias correction procedure described and termed ‘‘shuffled’’ in [162]. The shuffling correction has a higher variance but overcorrects the bias and leaves overall a smaller residual underestimation of $I(\mathbf{S};\mathbf{R})$. We found that this alternative bias correction procedure generated results similar to the ones presented in the paper (Fig. A.19 and App.

A S3 Table). The fact that our findings are stable using two methods biased in opposite directions, shows that our information estimations are accurate and that the results are solid and conservative.

Position-dependent correlation To measure whether correlation between pairs of neuronal and astrocytic ROIs was position-dependent, we computed pairwise Pearson’s correlations between calcium signals sampled inside and outside the response fields. On average, response fields were smaller than half the linear track, thus either set of observations, inside or outside the response field, could contain uneven amounts of datapoints. To compensate for the unbalanced numerosity, we resampled the same number of points found in the smaller set, while preserving temporal ordering. We then computed Pearson’s correlation between the two vectors. For each pair of ROIs, we computed the average Pearson’s correlation with 100 iterations of this procedure. We repeated this procedure inside both astrocytic fields and neuronal response fields.

Population analysis using SVM decoder of spatial position To decode animals’ position from a population of ROIs, we trained an SVM classifier with Gaussian kernel (Bishop 2006, Pedregosa, Varoquaux et al. 2011, Bzdok, Krzywinski et al. 2018). We performed decoding analysis on three datasets: i) astrocytic signals during monodirectional virtual navigation; ii) astrocytic signals during bidirectional virtual navigation; iii) simultaneous recording of astrocytic and neuronal signals during monodirectional virtual navigation. Experimental sessions were considered independently. We evaluated decoding performance as a function of decoding granularity, G , i.e., the number of spatial bins we used to discretize the linear track. For monodirectional virtual navigation, we used $G = (4, 8, 12, 16, 20, 24)$, and for bidirectional virtual navigation, for which there was a limited number of running trials, we used $G = (4, 8, 12, 16)$. All experimental sessions with at least three observations in each spatial bin were included in the analysis. For experiments in which we recorded astrocytic and neuronal calcium activity simultaneously, we measured decoding performance for multiple population settings, using both astrocytic and neuronal signals, or excluding either one. We used experimental session as the n -dimensional array of calcium event traces ($n = \text{number of ROIs}$) to decode discretized positions along the virtual linear track at each time point. Each experimental session was composed of a set of T_{exp} observations (X_i, y_i) , where X_i is the n -dimensional array of the calcium activity of the n ROIs, whereas y_i corresponds to the discretized spatial position. For each granularity, we trained and tested the SVM using 10-fold cross-validation procedure on each experimental session independently. During each iteration of the cross-validation, the SVM was trained and optimal hyperparameters were selected performing 5-fold cross-validation on each fold training-set. Predictions of the decoder for each of the 10-folds used as test were then collected to compute the overall performance of the decoder.

For each granularity, we measured decoding performance computing decoded information, as the mutual information between predicted and real spatial position [114]:

$$I(\mathbf{S}; \mathbf{S}_p) = \sum_{s, s_p} p(s, s_p) \log_2 \frac{p(s, s_p)}{p(s)p(s_p)} \quad (2.17)$$

where s_p denotes the decoded spatial position (with the SVM method described above) from the population response vector in each trial, s is the actual spatial position of the animal, and $p(s; s_p)$ is the decoder’s confusion matrix obtained from the predictions of the 10-folds cross-validation test-set. We corrected mutual information measures for the limited sampling bias using the conservative bootstrap correction method described in [157, 158, 162].

Decoding performance was also computed as decoding accuracy (fraction of correct predictions):

$$Accuracy = \frac{\text{number of correct predictions}}{\text{total number of predictions}} \quad (2.18)$$

To assess the statistical significance of decoding results, we trained and tested the decoder on each experimental session after randomly permuting position and responses. This procedure removed all information about position carried in the responses. We performed 103 random permutations for each granularity and population type. We then used the distribution of information values on permuted data as the null hypothesis distribution for the one-tailed non-parametric permutation test of whether information was significantly larger than zero. We repeated this procedure separately for each granularity.

To assess if the correlations among neurons and/or astrocytes increased the amount of spatial information, we disrupted across-neuron correlations by randomly shuffling, separately for each ROI, the order of trials with the same position category. We performed 500-trial shuffling for each granularity and population type. We then used the trial-shuffled distribution as the null hypothesis distribution for the one-tailed non-parametric permutation test of whether the information in the real population vector (which includes correlations) is significantly higher than that obtained when correlations are removed.

Decoding error analysis We investigated classification errors made by the decoder for each decoding granularity. We considered only misclassified samples in the test set and we measured the distance between the position predicted by the decoder and the ground truth position. We computed the frequency histogram of these deviations from the ground truth, and fitted a Gaussian curve [163] using non-linear least squares. For each histogram, we computed R2 score to quantify the fitting performance.

Computing genuine spatial information that cannot be possibly attributed to visual cue information To assess whether spatial information encoded in a calcium response could be attributed to visual cues, we leveraged on the structure of the visual patterns of the virtual linear track. Three distinct visual cues covered the whole length of the corridor each in 60 cm long segments. Within each segment, the visual stimuli were periodically repeated (Fig 2.1C). We reasoned that, if responses in the virtual reality corridor were only modulated by visual cues, regardless of the position in which the visual stimulus was provided, then it would not be possible to discriminate between positions within the spatial extent of each visual cue (60 cm). In such case, the responses would not carry any spatial information above and beyond the one that is inherited from the information they carry about the identity of the visual cue. To quantitatively test this hypothesis, we computed mutual information using (Eq. 8), while randomly shuffling positions of calcium responses observed within the spatial extent of each visual cue (IV). This spatially targeted permutation procedure preserved the information about visual cues identity, while it destroyed all the genuine spatial information carried by the response beyond visual cue information. We repeated this spatially targeted permutation procedure generating a distribution of IV values for each ROI (100 permutations). Information values were corrected for the limited sampling bias using the Panzeri-Treves procedure [158]. Responses were considered as carrying information beyond visual cue identity if the real information, I, was greater than 95th percentile of the distribution of IV. Positions and responses were discretized using uniform-width bins. We systematically characterized the effect of position discretization on the estimates of I and IV repeating binning spatial positions into different number of spatial bins NS (NS = 9, 12, 15 18). We used numbers of bins that were multiple integers of 3 to ensure that each spatial bin fell within an individual 60 cm-long visual cue zone. The number of response bins NR for astrocytic and neuronal responses were 4 and 2, respectively. We extended this analysis measuring information on population response vectors. We trained and tested the SVM decoder to decode discretized positions along the virtual linear track from the n-dimensional array of calcium event traces on each experimental session, while performing the spatially targeted permutation procedure described above. We repeated the permutation procedure 500 times to build a distribution of decoded information (Eq. 17) to estimate IV. For each experimental session, we computed the mean value of decoded information as the average of IV distribution. We repeated this procedure systematically varying the value of decoding granularity G (again using multiple integers of 3 for the number of spatial bins, thus leading to use G = 9, 12, 15, 18).

Statistics Significance threshold for statistical testing was always set at 0.05. No statistical methods were used to pre-determine sample size, but sample size was chosen based on previous studies [124, 127, 128]. Statistical analysis was performed using Python (SciPy 0.24, NumPy 1.19, statsmodels 0.9), or the InfoToolbox library [133] available for Matlab (MathWorks R2019b). A Python 3 [164] (version

3.6) front-end was used for execution. To test for normality, either a Shapiro-Wilks (for $N \leq 30$) or a D'Agostino K-squared test (for $N > 30$) was run on each experimental sample. When comparing two paired populations of data, a paired t-test or Wilcoxon signed-rank test were used to calculate statistical significance (for normal and non-normal distributions, respectively). Independent samples t-test and two-sample Kolmogorov-Smirnov test or Wilcoxon rank-sum test were used for unpaired comparisons of normally and non-normally distributed data, respectively. A binomial test was used to test if the fraction of successes at the population level in a number of statistical test performed at $p = 0.05$ could be due to chance. Bonferroni correction was applied to correct for the multiple testing problem when appropriate. Surrogate data testing was performed as described in the specific methods sections. All tests were two-sided, unless otherwise stated. When reporting descriptive statistics of data distributions, we used either the mean \pm standard deviation (mean \pm s.d.) for normal data or the median \pm median absolute deviation (median \pm m.a.d.) for non-normal data. Datasets reporting average values across experimental sessions were presented as mean \pm standard error of the mean (mean \pm s.e.m.). Bootstrap estimation was performed to identify 95% confidence intervals for mean values and for mean differences (Dekking, Kraaikamp et al. 2005), where appropriate [165]. Effect size was quantified as Cohen's d coefficient (Cohen 1988).

Experimental procedures

Animals All experiments involving animals were approved by the National Council on Animal Care of the Italian Ministry of Health (authorization 61/2019-PR) and carried out in accordance with the guidelines established by the European Communities Council Directive. From postnatal day 30, animals were separated from the original cage and housed in groups of up to five littermates per cage with ad libitum access to food and water in a 12-hour light-dark cycle. Experimental procedures were conducted on animals older than 10 weeks. The number of animals used for each experimental data set is specified in the text or in the figure legends.

AAV injection and chronic hippocampal window surgery Astrocytic-specific GCaMP6f expression was obtained using pZac2.1 gfaABC1D-cyto-GCaMP6f (Addgene viral prep # 52925-AAV5 a gift from Dr. Khakh, [85, 98]). Neuronal-specific jRCaMP1a expression was obtained using pAAV-CAMKII-jRCaMP1a (kindly provided by Dr. O. Yizhar) which was then packaged as AAV serotype 1-2 viral particles [166].

Male C57Bl6/j mice were anesthetized with 2% isoflurane/0.8% oxygen, placed into a stereotaxic apparatus (Stoelting Co, Wood Dale, IL), and maintained on a warm platform at 37 °C for the whole duration of the anesthesia. Before surgery, a bolus of Dexamethasone (4 mg/kg, Dexadreson, MSD Animal Health, Milan, Italy) was provided with an intramuscular injection. After scalp incision, a 0.5 mm craniotomy was drilled on the right hemisphere (1.75 mm posterior, 1.35 mm lateral

to bregma) and the AAV-loaded micropipette was lowered into the hippocampal CA1 region (1.40 mm deep to bregma). 800 nL of AAV solution was injected at 100 nL/min by means of a hydraulic injection apparatus driven by a syringe pump (UltraMicroPump, WPI, Sarasota, FL). Following the viral injection, a stainless-steel screw was implanted on the cranium of the left hemisphere and a chronic hippocampal window was implanted similarly to [124, 128]. A drill was used to open a 3 mm craniotomy centered at coordinates 2.00 mm posterior and 1.80 mm lateral to bregma. The dura was removed using fine forceps, and the cortical tissue overlaying the hippocampus was carefully aspirated using a blunt needle coupled to a vacuum pump. During aspiration, the exposed tissue was continuously irrigated with HEPES-buffered artificial cerebrospinal fluid (ACSF). Aspiration was stopped once the thin fibers of the external capsule were visible. A cylindrical cannula-based optical window was fitted to the craniotomy in contact to the external capsule and a thin layer of silicone elastomer (Kwik-Sil, World Precision Instruments, Sarasota, FL) was used to surround the interface between the brain tissue and the steel surface of the optical window. A custom stainless-steel headplate was attached to the skull using epoxy glue. All the components were secured in place using black dental cement and the scalp incision was sutured to adhere to the implant. Animals received an intraperitoneal bolus of antibiotic (BAYTRIL, Bayer, Germany) at the end of the surgery.

Optical windows were composed of a thin-walled stainless-steel cannula segment (OD, 3 mm; ID, 2.77 mm; height, 1.50 - 1.60 mm). A 3.00 mm diameter round coverslip was attached to one end of the cannula using UV curable optical epoxy (Norland optical adhesive 63, Norland, Cranbury, NJ). Sharp edges and bonding residues were smoothed using a diamond-coated cutter.

Virtual reality A custom virtual reality setup was implemented using the open-source 3D creation suite Blender (blender.org, version 2.78c). Virtual environment rendering was performed using the Blender Game Engine and displayed at video rate (60 Hz). The virtual environment was a linear corridor with the proximal walls characterized by three different white textures (vertical lines, mesh, and circles) on a black background. Distal walls were colored in green and labeled with a black cross. The corridor was 180 cm long and 9 cm wide. The character avatar was a sphere of radius 2 cm with a rectangular cuboid protruding at the equator parallel to the corridor floor (cuboid dimension: $x = 5$ cm, $y = 1$ cm, $z = 1$ cm). The cuboid acted as a virtual touch sensor with the environment. The character point of view (220° horizontal, 80° vertical) was rendered through a composite tiling of five thin bezel-led screens. The virtual corridor implementation described above was used for both monodirectional and bidirectional navigation. In monodirectional virtual navigation, mice navigated the environment running on a custom 3D printed wheel (radius 8 cm, width 9 cm). An optical rotary encoder (Avago AEDB-9140-A14, Broadcom Inc., San Jose, CA) captured motion and a single board microcontroller (Arduino Uno R3, Arduino, Ivrea, Italy) performed USB-HID-compliant conversion

to a serial mouse input. In bidirectional virtual navigation, mice navigated the environment using an air-suspended Styrofoam ball (radius, 10 cm) and a Bluetooth optical mouse (M170, Logitech, Lausanne, Switzerland) was used to read the vertical and horizontal displacement. In both monodirectional and bidirectional navigation, physical motion of the input devices was mapped 1:1 to the virtual environment. To motivate corridor navigation, mice received $4 \mu\text{l}$ water rewards upon reaching specific locations. Rewards were delivered through a custom steel lick-port controlled by a solenoid valve (00431960, Christian Bürkert GmbH & Co., Ingelfingen, Germany) and licks were monitored using a capacitive sensor (MTCH102, Microchip Technology Inc., Chandler, AZ). In monodirectional virtual navigation, rewards were delivered at 115 cm and the mouse was teleported to the beginning of the corridor after reaching the end of the track (inter trial timeout interval 5 s). If the mouse didn't reach the end of the corridor within 120 s, the trial was automatically terminated and the mouse was teleported to the beginning of the corridor after an inter-trial timeout. For bidirectional navigation, rewards were delivered at opposite ends of the track. After getting a reward, the mouse had to reach the opposite end of the virtual corridor to receive the next reward. Virtual reality rendering and two-photon imaging acquisition ran on asynchronous clocks while the command signal of the slow galvanometer was used to synchronize the imaging acquisitions with behavior.

Two-photon imaging during virtual navigation Two-photon calcium imaging was performed using an Ultima Investigator or an Ultima II scanheads (Bruker Corporation, Milan, Italy) equipped with raster scanning galvanometers (6 mm or 3 mm), a 16x/0.8 NA objective (Nikon, Milan, Italy), and multi-alkali photomultiplier tubes. For GCaMP6f imaging, the excitation source was a Chameleon Ultra pulsed laser tuned at 920 nm (80 MHz repetition rate, Coherent, Milan, Italy). Simultaneous GCaMP6f and jRCaMP1a imaging was performed with a two-beam path configuration in which two laser beams of different wavelength simultaneously illuminated the sample. On the Ultima Investigator, two pulsed laser sources were combined through a dichroic mirror (zt98rdc-UF1, Chroma Technology Co., Bellows Falls, VT; $\lambda_1 = 920$ nm, Alcor 920 fiber laser - 80 MHz repetition rate, Spark Lasers, Martillac, France; $\lambda_2 = 1060$ nm, Chameleon Ultra II - 80 MHz repetition rate, Coherent, Milan, Italy). On the Ultima II, two orthogonally polarized pulsed laser sources were combined through a polarizing beam splitter (05FC16PB.5, Newport; $\lambda_1 = 920$ nm, Chameleon Ultra II; $\lambda_2 = 1100$ nm, Chameleon Discovery - 80 MHz repetition rate, Coherent, Milan, Italy). Laser beam intensity was adjusted using Pockel cells (Conoptics Inc, Danbury, USA). Imaging average power at the objective outlet was 80 - 110 mW. Fluorescence emission was collected by multi-alkali PMT detectors downstream of appropriate emission filters (525/70 nm for GCaMP6f, 595/50 nm for jRCaMP1a). Detector signals were digitalized at 12 bits. Imaging sessions were conducted in raster scanning mode at 3 Hz using 5x optical zooming factor. Images contained 256 pixels x 256 pixels field of view (pixel

dwelling-time, 4 μ s; Investigator: pixel size, 0.63 μ m; Ultima II: pixel size, 0.51 μ m).

One or two weeks after surgery the animals were set on a water restricted schedule, receiving approximately 1 ml of water per day. Weight was monitored daily, and remained between 80 - 90 % of the starting weight throughout all procedures. Mouse habituation to the experimenter (handling) started two days after water scheduling and lasted for a minimum of two sessions. Following handling, mice were habituated to the virtual reality setup in successive training sessions. Starting from the second habituation session, the animals were head-tethered for a progressively increasing amount of time, reaching 1 hour in approximately one week. During virtual reality training sessions, mice were exposed to the noise generated by the two-photon imaging setup (e.g., galvanometer scanning noise, shutter noise). Training in the virtual environment lasted until animals routinely ran along the linear track. On experimental days, mice were head-tethered, and the virtual reality session started after a suitable field of view was identified. Three to six temporal series (750 frames/series; t-series duration, 250 s), interleaved by 5 minutes breaks, were acquired during a 1 hour virtual navigation session. Astrocytes and neurons were simultaneously recorded from the same focal plane. At the end of each imaging session, animals were returned to their home cage.

Histology Histology preparations were obtained similarly to [141, 167]. In brief, animals were deeply anesthetized with urethane and transcardially perfused with 0.01 M PBS, pH 7.4, and then 4% paraformaldehyde (PFA) in phosphate buffer (PB; pH 7.4). Brains were post-fixed overnight (ON) at 4°C and subsequently cut to obtain coronal slices of 40-50 μ m thickness. Sections were incubated ON, or for 48 h, at 4°C in primary antibody diluted in a PBS solution containing 5% NGS, 0.3% Triton X-100. Sections were then incubated for 24 h at 4°C in the appropriate secondary antibody solution. Cell nuclei were counterstained incubating the sections with Hoechst 33342 (1: 300) for 20 min at RT, mounted on glass slides using Fluoromount (Sigma Aldrich, Saint Louis, MO) and coverslipped. Primary antibodies were Anti-GFAP (1:300 rabbit, Abcam Ab16997, Cambridge, UK), Anti-NeuN (1:250 mouse, Millipore MAB377, Billerica, MA), Anti-GFP (1:500, chicken, Abcam Ab13970, Cambridge, UK). Alexa-conjugated (Invitrogen, Carlsbad, CA) secondary antibodies were used.

Fluorescence images were acquired with either a Leica SP5 inverted confocal microscope (40x/1.25 NA immersion objective, Leica, Milan, Italy) or with a Nikon A1 inverted confocal microscope (20x/0.8 NA objective, Nikon, Milan, Italy). Hippocampal regions and layers were identified using the anatomical hallmarks provided by cell nuclei counterstaining (Fig. A.1 A, B, Fig. A.11 A, B).

To quantify the extent of astrocytic reactivity in the hippocampus of implanted animals, we bilaterally acquired image-series of the hippocampal formations (3 x 3 tiles, 1024 x 1024 pixels/tile, 154 pixels overlap, pixel size 0.62 μ m/pixel, 8 planes, 1.5 μ m/step; Fig. A.1 A-B top). To avoid biases, image-series of both hemispheres (the implanted one and the control one) were acquired with the same parameters

(e.g., excitation laser power and photodetectors gain). We estimated the fraction of tissue immunoreactive for GFAP on maximum intensity projections. For each pair of projections (one for the implanted hemisphere and one for the non-implanted one), we selected three similar ROIs extending along the mediolateral axis of the hippocampal formation and spanning the dorsoventral extent of either stratum oriens, stratum pyramidale, or stratum radiatum (Fig. A.1 A-D). ROIs selected on each hemisphere were identical. We performed image thresholding on pairs of ROIs (one from the implanted and one from the control hemisphere) from matching hippocampal strata, selecting as cutoff-value the maximum of the threshold values computed on either ROI with the triangle method [168]. Thresholded ROIs were used to compute the fraction of GFAP immunolabeled pixels and their average fluorescence intensity value. Selectivity of GECI expression was assessed on confocal z-image series (9 planes, 2 $\mu\text{m}/\text{step}$) using ImageJ (imagej.nih.gov/ij, [169]) and the Cell-Counter plugin, counting cells immunolabeled for either GFAP or NeuN among GECI-expressing cells.

Chapter 3

Optimizing measures of information encoding in astrocytic calcium signals

3.1 Introduction

Established models of how populations of brain cells encode information consider exclusively the encoding at the level of population of neurons [144–147]. However, this view has been recently challenged by studies of the activity of astrocytes [111]. Astrocytes, the most abundant glial cell type in the mammalian brain, are not electrically excitable but display excitability based on complex dynamics of intracellular calcium (Ca^{2+}) concentration. Astrocytic Ca^{2+} dynamics can be recorded *in vivo* with high spatial resolution using functional two-photon microscopy [108]. Recordings of astrocytes in sensory areas have shown that these cells can encode sensory stimuli [46, 55, 58, 98, 109]. Recently, several laboratories [110–112] begun to investigate how astrocytes encode information about external variables. As an example, our work [111] has shown that astrocytes in hippocampal CA1 recorded during spatial navigation in a virtual environment encode spatial information that is complementary and synergistic to that carried by nearby "place cell" neurons. This additional non-neural reservoir of information suggests the possible presence of novel cellular mechanisms underlying how brain circuits encode information, and invites the inclusion of astrocytes in the models of brain information processing.

To improve our understanding of how astrocytes participate in information encoding it is important to have statistical tools that can be used to clarify whether astrocytes genuinely carry information about specific cognitive variables. Because little is known about how astrocytes encode information, non-parametric analyses that make little assumptions (e.g. linearity) about how information is encoded are particularly desirable at this stage. It has been recently proposed [111] that information theory [113, 114] may be an ideal candidate to this aim. However, the use of information theory with limited size datasets and noisy biological cells is made

difficult by statistical issues [162, 170]. The neural literature has studied, using computer simulations, how to set optimally procedures and parameters of the analysis given the levels of information encoded by neurons and the size of the dataset available [170]. However, such studies have not been performed for astrocytes.

Here, we performed simulations of astrocytic Ca^{2+} dynamics matching the statistical properties of signals recorded from real subcellular regions of interest (ROIs) of hippocampal astrocytes during virtual spatial navigation. We used these simulations to investigate how to optimally apply information theoretic methods to determine the presence and amounts of genuine information encoding by astrocytes. Last, we validated results and predictions of simulations by applying this methodology to *in vivo* recordings of hippocampal astrocytic subcellular Ca^{2+} signals during spatial navigation.

3.2 Computing amount and significance of information in astrocytic calcium activity

Here we introduce the measures of information about external variables carried by astrocytic activity, and we define the parameters of its computation from real data. Suppose we have a two-photon microscopy calcium imaging experiment where a mouse is performing a task or is shown a certain set of sensory stimuli. In this scenario we can record Ca^{2+} signals from astrocytic cellular compartments (for example, a soma or a process) defined as ROIs in a given field of view (FOV). We are interested in quantifying whether the Ca^{2+} response r of the astrocytic ROI, measured at given imaging time frame, encodes information about an external variable s that varies during the task or a stimulus variable that is varied across the experiment. In the experimental dataset that we will use [111], the Ca^{2+} dynamics of hippocampal CA1 astrocytes were recorded while a mouse was navigating in a linear track in a virtual reality environment. With this dataset we were interested in determining whether the astrocytic Ca^{2+} response encoded the position of the mouse along the linear track, similarly to how neurons called place cells do in hippocampus [122]. How selective is an astrocytic ROI with respect to an external variables s can be computed by using the mutual information $I(\mathbf{R}; \mathbf{S})$ between the set of astrocytic responses \mathbf{R} and the set of external variables \mathbf{S} , defined as follows [113]:

$$I(\mathbf{R}; \mathbf{S}) = \sum_s P(s) \sum_r P(r|s) \log_2 \frac{P(r|s)}{P(r)} \quad (3.1)$$

where $P(s)$ is the probability of the external variable taking the value s , $P(r)$ is the probability of measuring an astrocytic response r across all data points, and $P(r|s)$ is the probability of observing a responses r given a value s observed for the external variable. We assume that both astrocytic activity and the external variable take continuous values, and that we have discretized them into a number of bins R and S , respectively. These probabilities can be estimated as normalized histograms of

occurrences of discretized stimulus-response values. Such probabilities are computed from the finite number N of experimentally available datapoints (denoted "trials" hereafter) measuring simultaneously s and r . $I(\mathbf{R}; \mathbf{S})$ measures, in units of bits, how well we can infer the value of s from a single trial observation of the astrocytic response r . Zero bits indicate that no information can be gained from observing r , whereas positive values of information indicate that it is possible to reconstruct with some precision the value of s from the value of r . One bit means a reduction of uncertainty about s of a factor of 2 from a single-trial observation of r .

A first important question that can be addressed with mutual information analysis of astrocytes regards individuating how many and which ROIs carry information about external variables. An information value can be greater than zero even when the considered ROI actually has no information. This can happen because of random fluctuations in probability values generated by the limited number of trials that were sampled [162]. The statistical significance of each mutual information value can be determined by creating a null-hypothesis distribution obtained from surrogate datasets in which the relationship between s and r is destroyed by randomly shuffling the values of s and r across trials. A second important question regards quantifying precisely how much information each ROI carries. This is made difficult by the fact that, because of the limited number of trials available, the "plugin" information measure obtained simply by plugging the experimental probabilities into Eq. 3.1 is affected by a systematic upward bias [158]. Several bias correction procedures can be used to obtain an unbiased estimate mutual information [161, 162, 171–173]. Two widely used methods are Panzeri-Treves bias correction (PT) method [158], which analytically estimates the bias, and the quadratic extrapolation (QE) method [161], which estimates bias through extrapolating the information values obtained with data subsampling.

Thus, free parameters and algorithmic choices of the information analysis include the number of bins S and R , used to discretize the external variable s and the astrocytic Ca^{2+} activity, and the bias correction method used to compute information. Studies considering other types of brain signals have shown that computer simulations, characterized by realistic levels of information content and numerosity of trials, can be used to optimally set the information analysis parameters [162, 170]. However, no such work has been performed for astrocytes. Here, we implemented data-driven simulations to identify optimal parameters to perform mutual information analysis of astrocytic data. To understand how to optimally set information estimation parameters, we simulated set of astrocytic Ca^{2+} responses ($n = 20$) that realistically captured the dependency of astrocytic activity on the position of mouse during spatial navigation in virtual reality. (Astrocytic Ca^{2+} signals simulation software and mutual information software can be found at github.com/jbonato1/AstroSimulation). Ca^{2+} responses were modeled matching statistical parameters (mean and standard deviation) of Ca^{2+} responses of real astrocytic ROIs recorded *in vivo* from the hippocampal CA1 area of mice navigating in a virtual environment [111]. Responses for each spatial position were drawn from

a Gaussian distribution with the parameters found in the data. We evaluated the effects of trial numerosity, number of bins used to discretized the data, and information levels, by systematically modulating these parameters across simulations. The information level in the simulated responses was controlled by a parameter α [170] linearly rescaling the modulation of r by s . $\alpha = 1$ (no rescaling) yields simulated responses with the same response properties and thus information levels as real data, whereas $0 < \alpha < 1$ corresponds to modeling responses with reduced information content, and $\alpha = 0$ (modulation of r by s completely rescaled away) corresponds to no information. We report results of simulations for $\alpha = 1$ (full-information, Fig. 3.1A), $\alpha = 0.5$ (Fig. 3.1B) and $\alpha = 0$ (no-information, Fig. 3.1C).

We first evaluated the performance of the non-parametric shuffling in classifying simulated responses as carrying significant information. We performed these numerical experiments as function of the number of trial per stimulus numerosity (N_s), and information content (Fig. 3.1D-F). For this first study, simulated astrocytic responses were discretized into $R = 4$ equally spaced bins and space in the linear track was discretized into $S = 12$ spatial bins. For each simulated response we computed a null-hypothesis distribution generating 100 shuffles and we set a significance level of $p < 0.05$. When using the *plugin* estimate of mutual information, we found that for the full-information model ($\alpha = 1$) the shuffling procedure classified correctly significance down to $N_s = 64$ ($\log_2(N_s/R) = 4$). When reducing the information content ($\alpha = 0.5$) the shuffling test required more samples to perform correct detection. Finally when the model had no-information we found that false positive rate was stable at the level of 5% set by our statistical threshold. The use of PT bias correction procedure did not affect the statistical power of the non-parametric shuffling test, while QE method resulted in reduced statistical power.

Astrocytic Ca^{2+} signals and position recorded during spatial navigation are continuous variables, and the number of bins into which they are discretized is one of the most delicate parameters of the analysis. A too coarse discretization may wash out all information, and a too fine discretization may make the measures too noisy especially when data are scarce. Thus, S must be chosen to obtain to optimally trade off these two competing effects.

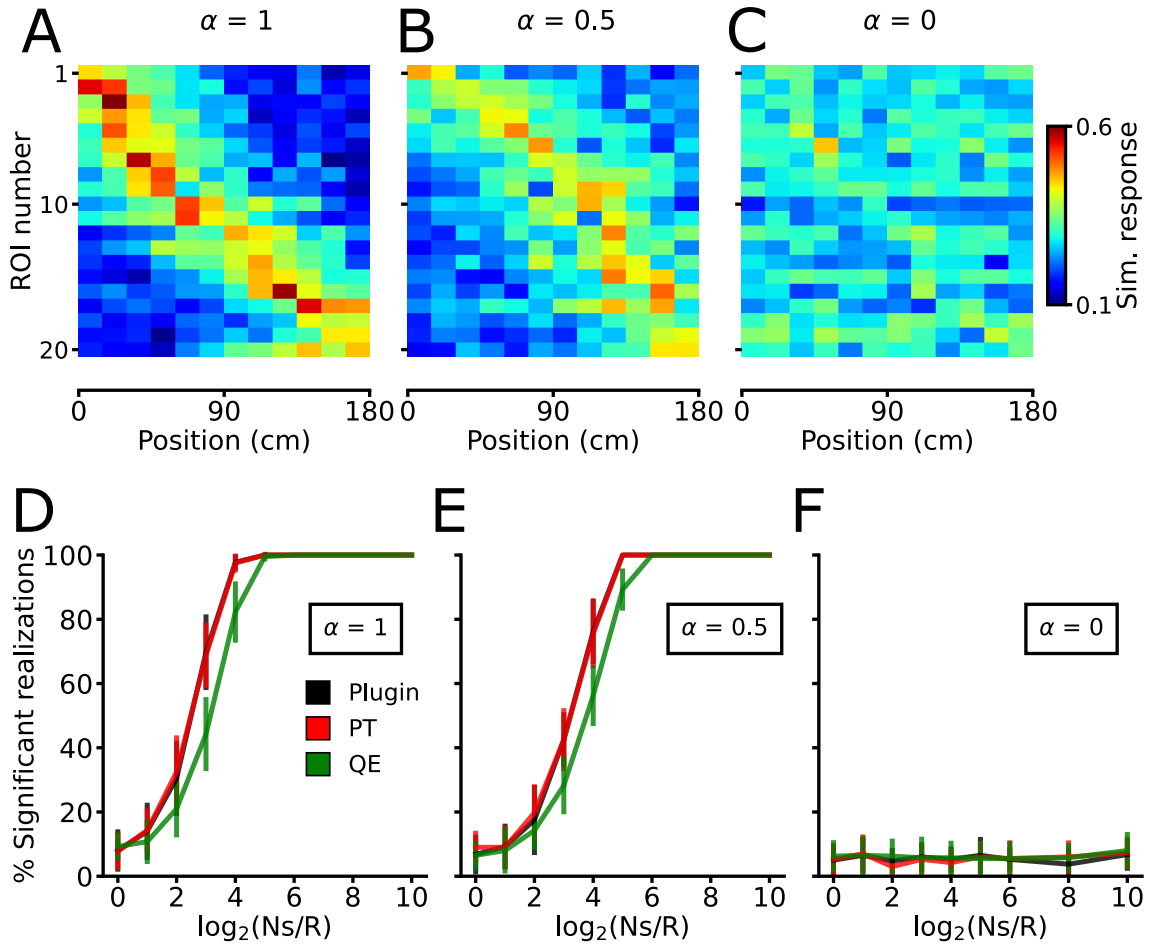


Figure 3.1: Sensitivity of information content measures for realistic simulations of position encoding astrocytic Ca^{2+} signals. (A-C) Mean Ca^{2+} responses across trials as a function of position for simulated astrocytic ROIs ($n = 20$ ROIs) for $\alpha = (1, 0.5, 1)$ models, respectively. The number of trials per spatial positions (Section 3.2, here 64) was varied across simulations. (D-F) Percentage of significant realizations detected using different methods (*plugin*, PT, and QE) as a function of N_s/R ratio for $\alpha = 1, 0.5, 1$ models. For each bias correction method, PT (red lines) and QE (green lines) information value was compared to the shuffled distribution of the corresponding values. 20 iterations of the simulation were generated for each number of trials used.

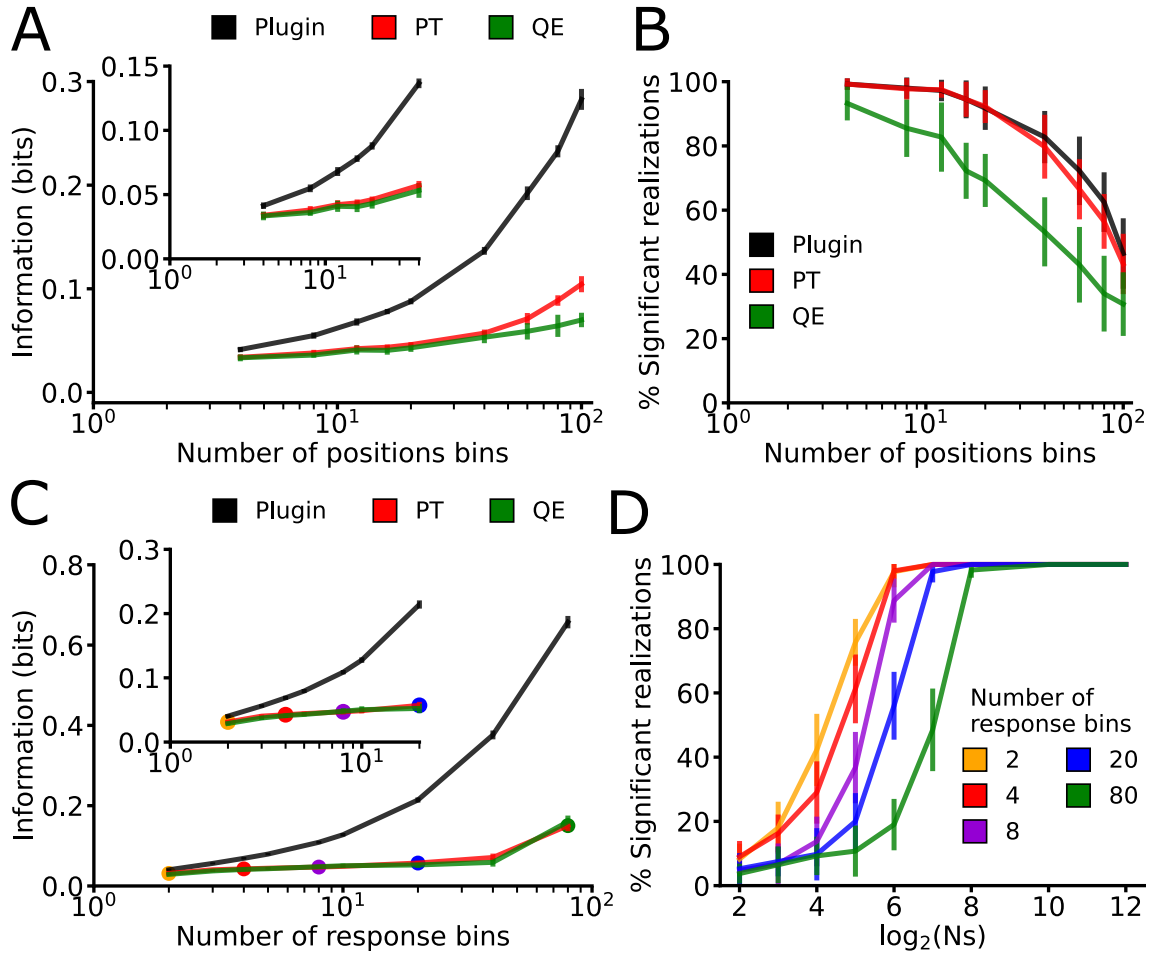


Figure 3.2: Characterization of information theoretic methods applied on simulations of astrocytic Ca^{2+} responses. (A) Average information estimate over 20 simulations as a function of the number of position bins. Simulations were repeated with fixed response discretization ($R = 4$), number of trials resembled experimental data sampling conditions. (B) Percentage of realizations classified as significant as a function of the number of position bins. (C) Average information estimate over 20 simulations as a function of the number of response bins. Simulations were repeated with fixed stimulus discretization ($S=12$) and constant number of trials per stimulus $N_s = 68$. In (A-C) information computations were performed without bias correction (*plugin*, black line), PT (red line) or QE (green line) bias corrections. (D) Percentage of significant realizations as a function of N_s for different values of number of response bins (no bias correction). The corresponding values of information for each R value are indicated by corresponding colored marks in panel (C). Data is shown as (mean \pm std).

We performed simulations using the full-information model ($\alpha = 1$) to generate data with a number of trials per stimulus resembling *in vivo* experimental data [111]. In these simulations we investigated the effect of position discretization while we kept the discretization of the response fixed at ($R = 4$). We found that (Fig. 3.2A) bias-corrected information measures (both PT and QE methods) plateaued

for values of S in the range (4 – 16). Conversely, *plugin* estimates monotonically increased with S , as their value contained an uncorrected upward bias component. For *plugin* estimates, we found that the fraction of realizations correctly detected as significantly informative (100 random shuffles, $p < 0.05$) decreased for S values greater than 16 (Fig. 3.2B), thus indicating insufficient sampling. The PT bias correction procedure did not affect the statistical power of the non-parametric shuffling test, while the QE method resulted in reduced statistical power. Thus, for further statistical tests we used uncorrected *plugin* estimators.

We characterized the effect of response discretization performing numerical experiments in which we simulated a realistic number of trials per stimulus ($N_s = 68$, equal to the average number of trials per stimulus in real data, see Section 3.4), while the position discretization was set within the information estimate plateau identified before ($S = 12$). We found that (Fig. 3.2C) bias-corrected information measures (both PT and QE methods) plateaued over a large range of R , whereas *plugin* estimates were strongly affected by bias. Statistical power was strongly dependent on the selection of discretization parameters (Fig. 3.2D) showing, in these sampling conditions, adequate power up to $R = 8$. Further increasing R would be possible only with much larger number of trials to avoid underestimation of significant astrocytes ROIs.

3.3 Measuring conditional mutual information to evaluate genuine information encoding

In many cases, cognitive tasks rely on several correlated external variables. An important question is how to determine whether astrocytic activity is genuinely informative about each such correlated variable. For example, in the mentioned spatial navigation experiments different parts of the track have different visual cues to aid navigation [111, 123, 124], thus there is a correlation between position s and visual cue identity v (Fig 3.3A). How do we determine for example if the astrocyte encodes genuinely spatial information above and beyond what can be explained by its possible tuning to the visual cue v ? One way to address this issue it to compute the conditional mutual information (CMI) [170] of an astrocytic response r about a stimulus s conditioned on the value of a visual stimulus v . This quantifies the amount of information encoded in responses \mathbf{R} about positions \mathbf{S} that cannot be explained by the tuning to a set of visual stimuli \mathbf{V} and it is defined as:

$$I(\mathbf{R}; \mathbf{S} | \mathbf{V}) = \sum_v P(v) \sum_{r,s} P(r, s | v) \log_2 \frac{P(r, s | v)}{P(r | v) P(s | v)} \quad (3.2)$$

where $P(r, s | v)$ is the joint probability of observing response r and stimulus s at fixed visual stimulus v . A non-zero value of CMI denotes genuine tuning of the astrocyte to s . The statistical significance of a CMI value can be assessed against a null-hypothesis distribution obtained shuffling the relationship between r and s

within each specific v . We evaluated the performances of CMI statistical testing

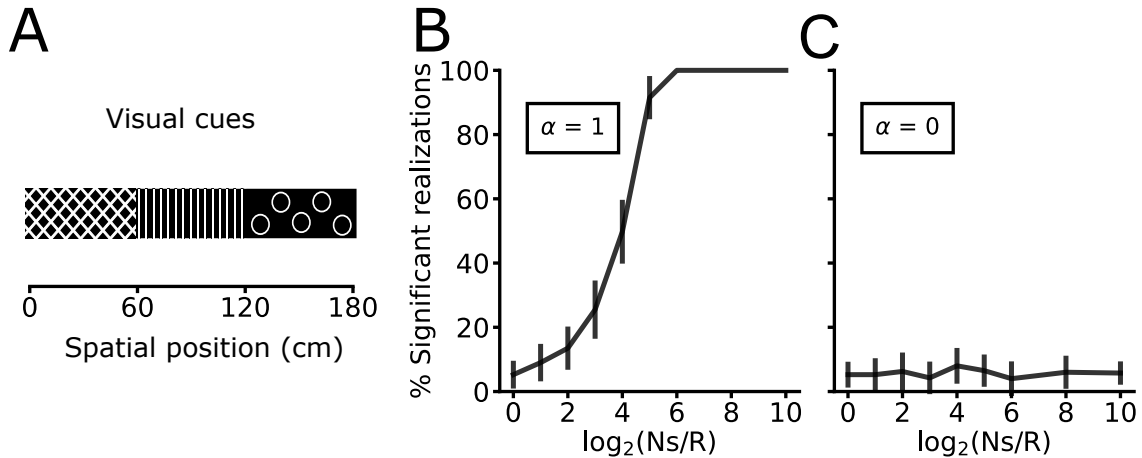


Figure 3.3: Determining the significance of conditional mutual information. (A) Schematic of a virtual track containing three distinct visual patterns [111, 123, 124]. (B-C) Percentage of significant realizations classified with the shuffling test and without bias correction (*plugin*) for models with genuine spatial information (B) and without spatial information (C). Data is shown as (mean \pm std).

in classifying simulated responses as bearing genuine spatial information. We used numerical experiments leveraging on the full information model ($\alpha = 1$), simulating astrocytic Ca^{2+} signals bearing spatial information. We found that, to achieve robust CMI significance detection, it is required to sample approximately 256 trials per stimulus (Fig. 3.3B). Then, we quantified the extent of false positives reported by the CMI statistical testing. We performed numerical experiments generating astrocytic Ca^{2+} signals devoid of spatial information ($\alpha = 0$). We found that the false positive rate was stable at 5% set by our statistical threshold (Fig. 3.3C).

3.4 Spatial information in CA1 astrocytes during spatial navigation

Here we apply the information theoretical formalism presented in Sections 3.2 and 3.3 to investigate information encoding in astrocytic Ca^{2+} dynamics using real two-photon functional imaging data. We used the dataset of [111], in which subcellular Ca^{2+} dynamics of hippocampal CA1 astrocytes (specifically labeled with the genetically encoded Ca^{2+} indicator GCaMP6f [57, 79, 85]) were recorded from head-fixed mice navigating in a monodirectional virtual corridor (Fig. 3.4A-B).

First, we investigated the influence of stimulus-response discretization on mutual information estimation and statistical significance detection on real data. We estimated the underlying probabilities for a grid of discretization parameters S (8, 12, 16, 20, 40, 60, 80) and R (2, 4, 6, 8, 10). We used a uniform-count binning procedure for positions and an equally-spaced binning procedure for responses. We found that

correcting the information measures for the limited sampling bias with PT method yield stable results over a wide range of discretization parameter S (4 – 16) (Fig. 3.4C), confirming the efficacy of the the PT method in accurately estimating the information value.

Significant realizations were affected by both S and R parameters. We found consistent results for $R > 2$ ($\sim 90\%$ of significant realizations) over the range of S (4 – 16) (Fig. 3.4D). This suggests that trial numerosity in this dataset limited the statistical power at more granular discretization conditions. These results are stable in the range (4 – 16) for S and in (4 – 10) for R confirming that performing mutual information measures within these parameters represents an optimal choice.

The virtual corridor used in the generation of this dataset [111] had three distinct visual cues extending 60 cm each (Fig. 3.4A). Thus, to test for genuine spatial information encoding, we applied the formalism described in Section 3.3. We performed the CMI significance test, for a set of position discretization conditions ($S = (9, 12, 15, 18, 30, 60)$) while responses were discretized with $R = 4$. For both discretization procedures we used equally spaced bins. We found that a large fraction (~ 40 to 55%) of astrocytic ROIs carried significantly genuine spatial information over a range (9 – 18) of position discretization conditions (Fig. 3.4E).

3.5 Conclusions

We created simulations of astrocytic responses with realistic dependencies of activity on external variables to investigate how to optimally set parameters and analyses procedures for a given experiment. While we do not wish to claim that such parameters will be always optimal, our results and simulation software provides a mean to set such parameters given certain easily measurable primary features of astrocytic data. Our results show that simple discretization and use of direct estimates, obtained from plugging in the empirical probabilities into the information equations, work well with reasonably high statistical power and with a rate of false positives that never exceeds the set p-value selection threshold.

Applications of these procedures to *in vivo* astrocytic functional imaging data demonstrated that a large fraction of astrocytic subcellular compartments in the CA1 region of the hippocampus carries genuine information about the spatial position, giving support to the emerging concept of astrocytic place cells as a part of the network computations performed in the hippocampus.

Future technical work includes investigating how to combine our information computations and selection criteria with other conservative criteria used for ruling out effects of data non-stationarities, such as reliability of Ca^{2+} activity across trial blocks [111].

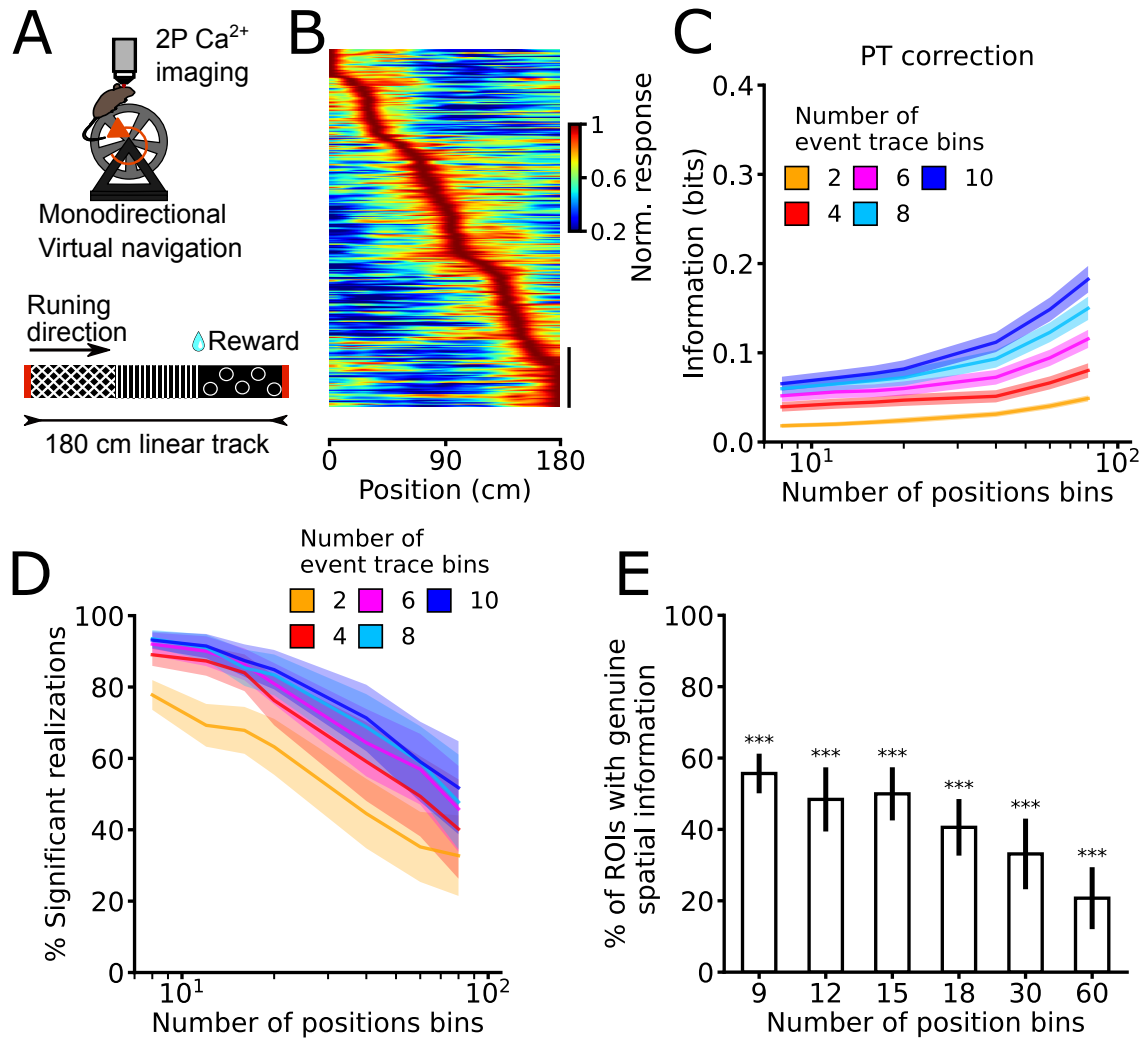


Figure 3.4: Spatial information encoding in CA1 astrocytes during virtual navigation. (A) 2-photon Ca^{2+} imaging was performed in head-fixed mice running along a 180 cm virtual track [111]. (B) Normalized astrocytic Ca^{2+} responses as a function of position for ROIs with significant spatial information computed with $R=4$ and $S=12$ ($n = 311$ ROIs out of 356 total ROIs, 7 imaging sessions from 3 animals). Responses are ordered according to the position of the maximum of the Ca^{2+} responses. Vertical scale: 50 ROIs. (C) Mutual information values with PT bias correction as a function of the number of position bins. (D) Percentage of ROIs classified significant as a function of the number of bins for the stimulus. (E) Fraction of astrocytic ROIs showing a significant decrease in their information content when position is shuffled within the same visual cue (Binomial test with 0.05 probability of success; *, $p < 0.05$; **, $p \leq 0.01$; ***, $p \leq 0.001$). Data are mean \pm s.e.m. from 7 imaging sessions in 3 animals.

Chapter 4

Rapid spatiotemporal analysis of astrocytic calcium dynamics using deep learning

4.1 Introduction

Astrocytes tile the entire central nervous system in non-overlapping domains [31] interacting with neurons, vasculature, and other glial cells. Astrocytes exhibit a form of excitability based on changes in the intracellular concentration of calcium (Ca^{2+}) [52, 75]. These calcium signals are tightly related to synaptic activity [5, 76, 134], are boosted by sensory inputs [46, 58, 109], and are instrumental for cognitive performance enhancement [174]. More recently, astrocytic Ca^{2+} signals have been shown to encode information about external, behavioral relevant, variables [110–112].

Astrocytic Ca^{2+} signals can be monitored with high spatial resolution in the intact brain of awake animals using two-photon microscopy and chemical or genetically encoded calcium (GECI) indicators [58, 98, 129, 175]. The spatial features of astrocytic Ca^{2+} signals are intrinsically related to the elaborated morphology of these cells, which is characterized by a highly ramified structure of thin processes stemming from the soma and covering a tissue volume of $\sim 70\text{-}100\ \mu\text{m}$ diameter. Within this tissue volume, astrocytic processes contact few neural cell bodies, hundreds of dendrites, and thousands of synapses [34]. Astrocytic Ca^{2+} dynamics that can be localized to specific subcellular compartments including the cell body and portions of processes [92, 93] and can have different spatial and temporal characteristics [59, 93, 118].

Available methods to measure astrocytic Ca^{2+} dynamics at subcellular level in individual astrocytes such as GECI-Quant [98] and CHIPS [58]¹ provide semantic segmentation of astrocytes, but heavily depend on data acquisition conditions, require several user-defined parameters, and need significant computational time.

¹CHIPS identifies only processes of astrocytes whereas somata have to be segmented manually

Alternative approaches (e.g., AQuA) identify Ca^{2+} events within and across astrocytes as coherent, spatially-confined activity regions, based on pixel-wise fluorescence dynamics [176]. Event-based approaches are computationally demanding, still require a posteriori segmentation to relate identified events to astrocytic morphology, and have not been validated on large fields-of-view comprising large networks of astrocytes. Altogether, currently available approaches limit reproducibility, generalization, and scalability of the analysis of astrocytic Ca^{2+} signals both within individual cells and across populations. Therefore, developing fast, automatic, and reliable image segmentation methods for analyzing astrocytic Ca^{2+} signals within individual cells and across large population of astrocytes is of utmost importance for the field.

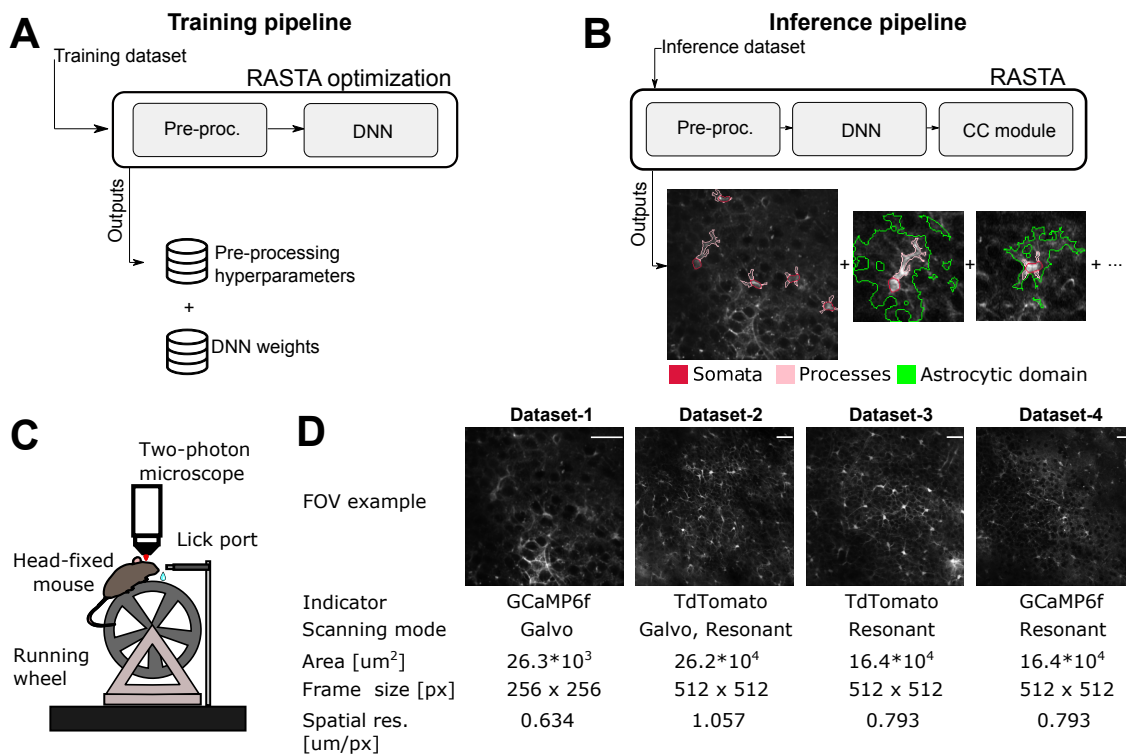


Figure 4.1: RASTA: a machine learning algorithm for fast and automatic semantic segmentation of astrocytes. A-B) Flow-charts of RASTA segmentation pipelines for training (A) and inference (B). At the end of the training pipeline, pre-processing hyperparameters and DNN weights are saved. At the end of the inference pipeline spatial coordinates corresponding to somata, processes, and cross-correlated regions are saved. C) Two-photon Ca^{2+} imaging of hippocampal and cortical astrocytes was performed in head-fixed mice running on a wheel. D) Four datasets were initially used for RASTA training and testing. Details of each dataset are listed in the figure. Each dataset was manually segmented by 3 expert annotators. White bars on the top-right of each image represents the scale bars. Dataset-1 $40 \mu\text{m}$, Dataset-2 $50 \mu\text{m}$ Dataset-3 $40 \mu\text{m}$, and Dataset-4 $40 \mu\text{m}$.

Similar challenges are faced in neuronal Ca^{2+} imaging, where most advanced segmentation methods include both unsupervised and supervised machine learning approaches [177–182]. Unsupervised methods like principal component analysis (PCA), independent component analysis (ICA), clustering based methods (Suite2p), and constrained nonnegative matrix factorization (CNMF, CaImAn Batch, CaImAn Online) focus on detecting and de-mixing active neuronal signal sources. Recently, supervised deep learning approaches based on 2-dimensional (2D) CNNs (UNet2DS) or 3-dimensional (3D) CNNs (STNeuroNet), have been applied for neuronal segmentation [180, 182]. UNet2DS learns spatial footprints of neurons from datasets directly labelled on the mean temporal projection of the recorded t-series. Although computationally convenient, the mean temporal projection of the t-series lacks temporal information about the dynamics of calcium signals. This issue was addressed adopting 3D-CNNs which learn spatiotemporal informative features of neurons [182]. However, it is unlikely that approaches specifically developed for segmentation of neuronal calcium imaging t-series can be readily applied to the analysis of astrocytic Ca^{2+} signals, because the spatial and temporal features of astrocytic Ca^{2+} signals are intrinsically different from those of neurons.

Here we present RASTA, Rapid Astrocytic calcium Spatio-Temporal Analysis, a novel machine learning-based software to perform fast, reliable, precise, and automatic semantic segmentation of astrocytic two-photon imaging t-series. RASTA combines feature engineering and a deep learning algorithm to enable scalable and repeatable analysis. RASTA performs cell detection (identification of visible somata of astrocytes) and semantic segmentation (labeling of cell soma and proximal processes) with near-human performance. RASTA outperforms state-of-the-art software for the analysis of astrocytic and neuronal signals, can be combined with event-based analytical approaches for a posteriori anatomical identification, and generalizes across indicators and acquisition conditions. RASTA has been validated on four new datasets recorded in awake head-fixed animals and labeled by 3 expert annotators. These datasets and their annotation are shared to establish the first astrocytic annotation challenge (Neurofinder challenge), with the aim to promote future improvements of astrocytes detection and segmentation algorithms. RASTA source-code is available at <https://github.com/jbonato1/RASTA>².

4.2 Results

RASTA: structure and analysis workflow

RASTA combines supervised and unsupervised techniques to provide a fully automatic segmentation of spatiotemporal information in astrocytes imaged in t-series using two-photon fluorescence microscopy. RASTA includes a training pipeline and an inference pipeline (Fig. 4.1 A-B). Each pipeline analyzes a dedicated dataset

²The repository is not public yet. Send an email to bonato.jimi@gmail.com with your github username to request the access.

called training set or inference set. The training set is a subset of the FOVs in the dataset that is used to optimize the algorithm. The inference set is the subset of FOVs in the dataset that is used to evaluate algorithm performance. The training pipeline (see Methods for details) optimizes RASTA hyper-parameters and the deep neural network. This optimization procedure removes human supervision from the RASTA inference pipeline. The inference pipeline comprises three main steps: i) pre-processing; ii) semantic segmentation; iii) subcellular cross-correlation analysis. The pre-processing step (Methods) computes a bi-dimensional reconstruction of the recorded field-of-view (FOV), compressing spatial and temporal features into a highly informative spatiotemporal projection. The outputs of the pre-processing step feed the second step, semantic segmentation, which employs a deep neural network (DNN) to perform subcellular semantic segmentation of astrocytic somata and processes. To this aim, we developed a U-Net-based [116] DNN architecture (Methods), which semantically segments astrocytes identifying and distinguishing somata from processes. Conventional two-photon imaging datasets have too small of the size to lead proper optimization of any deep learning-based method. Thus to optimally tune the DNN, we opted for efficient feature-engineering during the pre-processing and transfer-learning step using a DNN encoder pretrained [183–185] on ImagNet dataset [186] (see Methods for details). Finally, subcellular cross-correlation analysis, identifies regions of the astrocytic domain showing fluorescence signals that are statistically correlated to the one present in the semantically segmented regions of the astrocyte (see Methods for details). The output of the inference pipeline consists of three classes of ROIs: somata, processes, and cross-correlated regions (Fig. 4.1 B). RASTA is thus an end-to-end algorithm for the analysis of morphological and dynamical properties of astrocytes in two-photon fluorescence imaging t-series.

Generation of the consensus annotation

We evaluated RASTA performance against manual consensus annotation of the whole dataset. Three expert annotators detected and segmented astrocytes, labelling somata and individual processes. Annotators had access to both the raw t-series and the bi-dimensional projections of the t-series obtained during the pre-processing step (see above and Methods). Annotators detected astrocytes on the t-series, while segmenting subcellular structures on bi-dimensional projections. Manual annotation was executed on four datasets of two-photon fluorescence hippocampal imaging in awake head-fixed mice running on a wheel (Fig. 4.1C). The four datasets differed for the type of fluorophore which was expressed in astrocytes (e.g., GCaMP6f, Td-Tomato), imaged area (from $26.3 \times 10^3 \mu\text{m}^2$ to $26.2 \times 10^4 \mu\text{m}^2$), and acquisition conditions (galvanometric mirror-based imaging vs resonant scanning imaging and pixel resolution from $0.63 \mu\text{m}/\text{pixel}$ to $1.06 \mu\text{m}/\text{pixel}$, Fig. 4.1 D).

To generate an appropriate ground truth, we first identified the variability of human manual annotations, an inherent characteristic of manual data curation [181].

Annotators were then asked to reach a consensus resolving each single annotation discrepancy (see Methods for details). This procedure generated the “consensus annotation”, which was used as ground truth to quantify the performance of RASTA and of each annotator (Fig. B.2). The four datasets and their annotation by graders provides, to the best of our knowledge, the first systematically annotated dataset which will be shared to the astrocyte community.

Somata detection performance of human annotators was highly accurate (high F1-score), demonstrating an overall agreement on astrocyte somata detection. Conversely, segmentation performance of human annotators showed lower F1-scores. This was especially true for processes, confirming that annotation by single human grader can be unreliable for benchmarking purposes (App. B Tab. S1, Tab. S4, Tab. S5, and Tab. S6). We thus used the consensus annotation as a more reliable comparative standard [182].

RASTA achieves human performance

To test RASTA performance we used dataset-1, which comprises a set of 24 two-photon calcium imaging recordings of the CA1 hippocampal region recorded in head-tethered awake mice, which were spontaneously walking on a wheel (Fig. 4.1C). In the hippocampal CA1 region, astrocytes expressed the genetically encoded calcium indicator GCaMP6f after adeno-associate viral transduction. GCaMP6f signals were collected from a FOV of area $26 \times 103 \mu\text{m}^2$ with a spatial sampling of $0.634 \mu\text{m}/\text{pixel}$ (Fig. 4.1D, see also Methods for details).

We tested RASTA on dataset-1 using the leave-one-out cross-validation method, which consists of iteratively removing one FOV from the dataset, training the algorithm on the $N-1$ FOVs, and testing the algorithm on the removed FOV. Fig. 4.2A and 2B show an example of annotations obtained by RASTA on a representative FOV compared to the consensus ground truth. Importantly, Precision, Recall, and F1-score of RASTA detection was high and not significantly different from that of annotators (Fig. 4.2C, App. B Tab. S1). Segmentation F1-score was high for somata and similar to the one of two of the three annotators (Fig. 4.2D, Fig. B.3 A-B, App. B Tab. S2). Segmentation F1-score was lower for processes but similar to the one of all annotators (Fig. 4.2D, Fig. S5 A-B, App. B Tab. S2). Overall, these results indicate that RASTA detection and segmentation accuracy levels are comparable to those of human annotators.

RASTA outperforms state-of-the-art algorithms for the analysis of astrocytic and neuronal signals

We benchmarked RASTA against most of the available methods for analysis of two-photon fluorescence recordings of astrocytes and neurons (Fig. B.4): GECl-Quant [98], AQuA [176], STNeuroNet [182], UNet2DS [180], and CaImAn [181].

We first compared RASTA performance with that of GECI-Quant, a threshold-based user-supervised software [98] used for the analysis of astrocyte fluorescence images. For each FOVs, one annotator manually identified astrocytic somata and astrocytic domain, and defined the thresholds to segment somata and processes according to GECI-Quant documentation [98] (Fig. B.5 A). Given that one annotator manually identified the regions of analysis and given that the detection performance of RASTA were not significantly different from that of all annotators (Fig. 4.2C), the detection F1-score of GECI-Quant was not significantly different from that of RASTA (two-sided Wilcoxon rank sum test $N=24$, Fig. B.5 B). In contrast, segmentation performances of GECI-Quant were lower than those of RASTA for both somata and processes (Fig. 4.2E and Fig. B.5 C-D, App. B Tab. S2, two-sided Wilcoxon rank sum test $N= 24$).

We then compared the performance of RASTA to that of AQuA [176], a recent event-based algorithm for the analysis of astrocytic Ca^{2+} signals. AQuA focuses on the identification of calcium events, defined as spatially coherent signal dynamics across pixels. Although AQuA definition of events does not consider morphological constraints, we reasoned that a subset of the group of pixels classified as one event must belong to astrocytic somata and processes. We thus reconstructed astrocytic morphology from the spatio-temporal map of Ca^{2+} events identified by AQuA, and we compared it to astrocyte segmentation obtained by RASTA (see Methods for details). We found that precision, recall and F1-score for identified astrocytic morphology was higher for RASTA compared to AQuA (Fig. 4.2F, App. B Tab. S3, two-sided Wilcoxon rank sum test, $N= 24$). Taken together, these results demonstrate that RASTA outperforms state-of-the-art methods used for the analysis of astrocytes data in identifying astrocytic somata and processes.

We finally compared RASTA performance with STNeuroNet, UNet2DS, and CaImAn, three state-of-the-art algorithms for neuron segmentation, which perform binary classification (foreground vs background) of pixels in FOVs identifying neuronal ROIs. Since in most applications these algorithms are used to detect neuronal cell somata, we used them for astrocyte somata detection (Fig. 4.2G, App. B Tab. S2). Since in both pre-processing and post-processing STNeuroNet constrains source detection using parameters based on neuronal calcium imaging signal dynamics, we adjusted these steps to account for astrocytes signal dynamics and morphology (see App. B). We found that somata detection performance (quantified as the F1-score) of UNet2DS (mean \pm sem, 0.65 ± 0.04 , $N = 24$) was significantly higher than that of CaImAn (mean \pm sem, 0.20 ± 0.04 , $N = 24$) and STNeuroNet (mean \pm sem 0.27 ± 0.05 , $N = 24$, two-sided Wilcoxon rank sum test). Importantly, somata detection performance of STNeuroNet, UNet2DS, and CaImAn was significantly smaller than that of RASTA (Fig. 4.2G, two-sided Wilcoxon rank sum test, $N = 24$, indicating that our approach outperforms available analysis methods specifically developed for neuronal datasets).

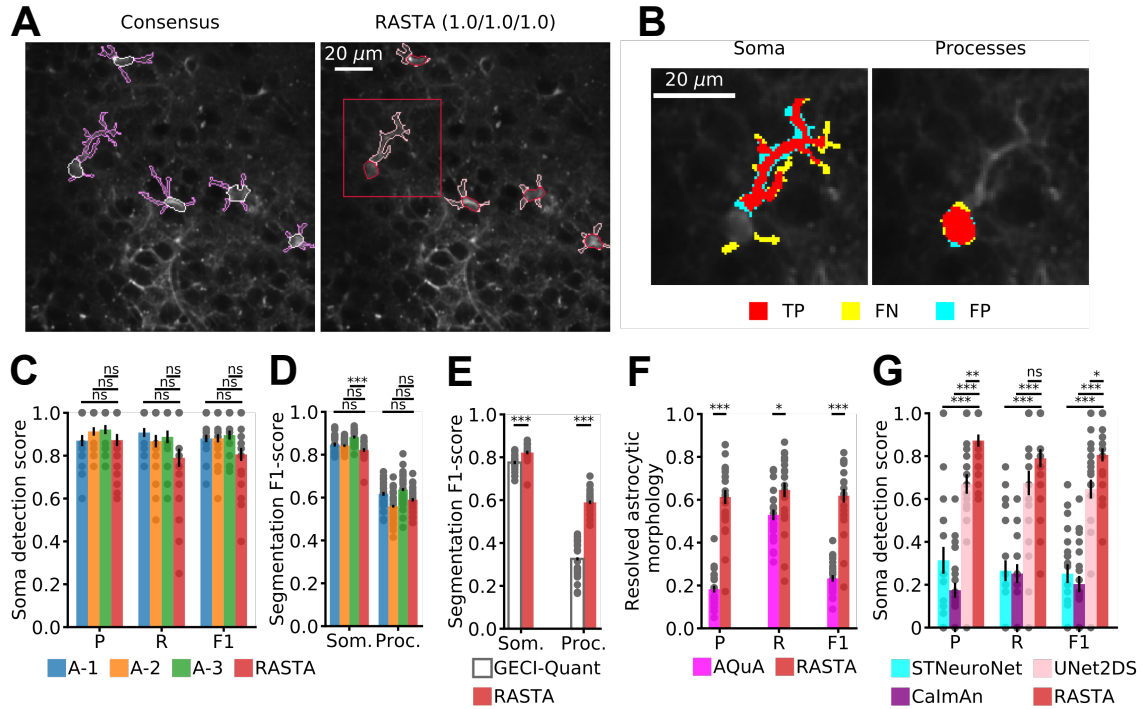


Figure 4.2: Evaluation and benchmarking of RASTA on dataset-1. A) Representative comparison of consensus annotations (left, FOV id: 2) and RASTA semantic segmentation (right). On the top of right image are reported somata detection precision, recall and F1-score for FOV id:2. B) Representative example of the comparison of somata and processes segmentations between RASTA and the consensus annotations. True positive pixels (red), false negative pixels (green), and false positive (cyan) are shown. C) Performance of the three annotators A-1, A-2, and A-3 against RASTA. Precision (P), recall (R), and F1-score (F1) are shown. Two-sided Wilcoxon rank sum test $N=24$; leave-one-out cross validation (LOOCV) results. In this as well as in following figures: n.s., not significant, $*P < 0.05$, $**P < 0.005$ and $***P < 0.0005$. D) F1-score for somata and processes segmentation for annotators and RASTA. Two-sided Wilcoxon rank sum test $N=24$, LOOCV results. E) F1-score for somata and processes segmentation of GECI-Quant and RASTA. Two-sided Wilcoxon rank sum test $N=24$; LOOCV results. F) Astrocytic morphology reconstructed using RASTA segmentations and AQuA event detection. Two-sided Wilcoxon rank sum test $N=24$; LOOCV results. G) Soma detection performance of STNeuroNet, CalmAn, UNet2DS, and RASTA. Two-sided Wilcoxon rank sum test $N=24$; LOOCV results. See also table S1 and S2.

Identification of functional domains of individual astrocytes using RASTA

Thin (diameter $< 1 \mu\text{m}$) astrocytic processes display information-rich Ca^{2+} dynamics [59, 98, 117]. However, the identification of these thin structures is challenging, because of the lack of an anatomical reference due to the subresolved dimension of these small cellular compartments. Here we propose to use a statistical correlation measure to reliably and reproducibly identify the extent of an astrocytic functional domain, including somata, main processes, subresolved cellular compartments. We named this analytical step within RASTA “subcellular cross-correlation analysis” and it automatically selects pixels within the extent of a domain of an individual astrocyte (see Methods for details) whose fluorescence dynamics are correlated to the pixels belonging to the semantically segmented ROIs (either somata or processes) of that same astrocyte (Fig. 4.3A). The output of this analytical procedure is a ROI of correlated pixels (Fig. 4.3A), which includes cell somata and processes and which resembles anatomically defined astrocytic domains [31].

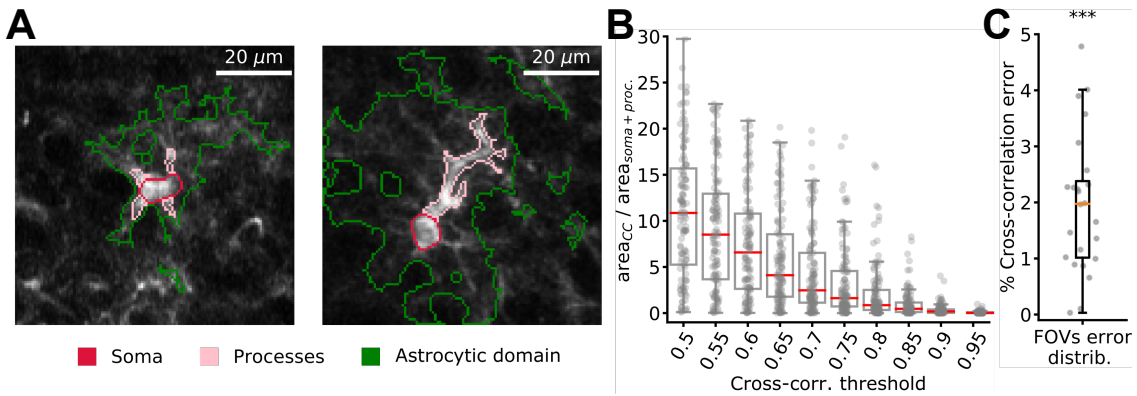


Figure 4.3: Identification of correlated calcium signals in astrocytic domains using RASTA. A) Two representative examples of statistically correlated regions in the astrocytic domain identified with the cross-correlation module (FOV (Id:2)). ROIs corresponding to somata and processes are colored in red and pink, respectively. ROIs extracted using cross correlation are shown in green. B) Ratio of ROI area extracted using the cross-correlation module and ROIs area obtained by summing soma and processes ROIs together as a function of the cross-correlation threshold. C) Cross correlation error distribution. The cross-correlation error was estimated as the mean percentage of false-positive pixels selected in each FOV sampling 1000 pixels outside astrocytes domains, which were not used to tune the cross-correlation threshold. Two-sided Wilcoxon rank sum test $N=24$.

We investigated how the area of the identified astrocytic domain depended on the value of the cross-correlation threshold (Fig. 4.3B). In the low threshold values regime more pixels were selected, including those belonging to neuronal structures (i.e., neuronal cell somata [31, 34]). Conversely, in the high threshold values regime the number of selected pixels decreased, neglecting potentially meaningful astrocytic structures. To set an appropriate threshold value, we programmed RASTA

to dynamically auto-tune the cross-correlation threshold for each FOV, in order to minimize the false positive selection. To this aim, a set of pixels sampled outside the astrocytic domains, whose intensities fluctuations were assumed to be independent from the ones of the ROIs pixels, was used as proxy to evaluating the percentage of false positive pixels selected given a threshold. The auto-tuning strategy identified the minimum threshold with false positive percentage error $< 5\%$ (see Methods for details). To benchmark the cross-correlation module, we estimated the fraction of selected pixels in the region outside putative astrocyte domains (false positive) of each FOVs using the consensus annotations as reference ROIs (see also Methods). We observed that the cross-correlation module selected false positive pixels with an average percentage error of $2.0 \pm 0.2 \%$ (mean \pm sem, two-sided Wilcoxon rank sum test $N=24$, Fig. 4.3C).

Finally, we reasoned that the functional domains of individual astrocytes identified RASTA could be used to seed the event-based analysis performed by AQUA. In (Fig. B.6), we show examples of astrocytic domain identified by RASTA that are used as priors instruct cell-specific AQUA analysis. Taken together these findings demonstrate that RASTA can be used to identify functional domains of individual astrocytes encompassing the cell somata, main processes, and thin astrocytic structures. Moreover, combining RASTA with event-based analysis software (e.g., AQUA) allows overlaying anatomical with functional analysis of astrocytic domains, enabling the extraction of previously hidden morpho-functional information from individual astrocytes two-photon GCaMP imaging experiments.

RASTA performance across signal-to-noise ratio conditions

To investigate RASTA performance as a function of the quality of two-photon images, we performed a set comparative RASTA analyses in t-series in which we artificially modified the peak signal-to-noise ratio (PSNR) of fluorescent signals. Specifically, we manipulated dataset-1 increasing or decreasing noise levels, thus generating six simulated datasets (Fig. 4.4A, see also Methods for more details). RASTA detection F1-score significantly decreased when the PSNR was strongly reduced (Fig. 4.4B, two-sided Wilcoxon rank sum test $N = 24$). However, the F1-score for the segmentation of somata and processes remained unaltered (Fig. 4.4C, Fig. B.7 A-B). These results that RASTA semantic segmentations was not affected by decreased PSNR. In contrast, an increase of the PSNR resulted in an improvement of the F1-score for detection (Fig. 4.4B, two-sided Wilcoxon rank sum test $N = 24$) and of the F1-score for segmentation of processes (Fig. 4.4C, Fig. B.7 A-B; two-sided Wilcoxon rank sum test $N = 24$), with no significant change of the F1-score for somata segmentation.

We also evaluated the state-of-the-art detection and segmentation methods described before on artificial datasets with different PSNR. We first tested GECl-Quant detection and segmentation performance under high PSNR conditions (1.81 of PSNR, Fig. B.8 A-D). To this aim, each FOVs one annotator manually defined

astrocytes soma region and astrocyte domain (Fig. B.8E). We found that the detection F1-score of GECI-Quant was significantly lower than that of RASTA (Fig. B.8A, two-sided Wilcoxon rank sum test $N = 24$). GECI-Quant F1-scores for process segmentation was also lower than that of RASTA (Fig. B.8D, two-sided Wilcoxon rank sum test $N = 24$). We then tested algorithm developed for the analysis of neuronal datasets. We found that STNeuroNet and CaImAn showed lower performance across all PSNR conditions when compared with RASTA (Fig. B.8 F-G, two-sided Wilcoxon rank sum test on all artificial datasets, $N = 24$, compared with real data). UNet2DS showed lower F1-score compared to RASTA, but this decrease was significant only for $\text{PSNR} = 0.88$ (Fig. B.8H, two-sided Wilcoxon rank sum test $N = 24$). However, since UNet2DS use only the mean projection in time of the recorded videos the injected gaussian noise does not affect this projection. Hence, the network performances remain stable across all noise conditions.

Overall, these results show that RASTA performance remains stable under low PSNR conditions and superior compared to the performance of state-of-the-art methods for the analysis of astrocytic and neuronal functional signals.

Data preprocessing contributes to increase RASTA performance

RASTA retrieves spatial and temporal information about fluorescence signals from the spatiotemporal projection of the t-series, which is performed in the preprocessing step. Here, we sought to investigate the impact of the spatial and temporal preprocessing step on RASTA segmentation performance (Fig. B.9 A-B). To this aim, we first tested RASTA directly on the raw median projection of the t-series, hence removing all the pre-processing steps (RASTA-Naive in Fig. 4.4D-E and Fig. B.9 C-D). We observed that the detection and segmentation performance of RASTA-Naive decreased when compared to RASTA (Fig. 4.4D-E, two-sided Wilcoxon rank sum test $N = 24$). We then investigated how the enhancing of temporal information, which is performed in the preprocessing step contributes to perform to RASTA performance. We removed the temporal pre-processing steps and we observed a significant decrease in processes segmentation F1-score results (RASTA-Spatial in Fig. 4.4 D-E and Fig. B.9 C-D, two-sided Wilcoxon rank sum test $N = 24$). These results highlight the importance of the preprocessing step and of spatial and temporal information in RASTA performance.

Duration of t-series: RASTA operative range

The length of the recordings is a fundamental parameter which can vary from one experiment to another. Since this parameter can impact the effectiveness of the preprocessing step, we investigated RASTA performance as a function of the number of frames in the t-series (Fig. B.10), shortening acquired t-series to movies containing 400, 300, 200, 100, and 50 frames, respectively. RASTA performance was

2 comprises a set of eight two-photon imaging recordings collected in either resonant- or galvanometric mirror-based scanning in the hippocampus of head-fixed awake animals, which were spontaneously walking on a wheel (Fig. 4.1A). In this dataset, hippocampal astrocytes specifically expressed TdTomato and fluorescence signals were collected from a FOV of area $26.2 \times 104 \mu\text{m}^2$ with pixel size of $1.06 \mu\text{m}/\text{pixel}$ (Fig. 4.1B, see also Methods for details). Dataset-3 is composed of a set of seven two-photon imaging recordings collected in resonant scanning mode in the hippocampus of head-tethered awake animals spontaneously walking on a wheel (Fig. 4.1A). Hippocampal astrocytes specifically expressed TdTomato and fluorescence signals were collected from a FOV of area $16.4 \times 103 \mu\text{m}^2$ with a pixel size of $0.79 \mu\text{m}/\text{pixel}$ (Fig. 4.1B). Dataset-4 includes a set of ten two-photon calcium imaging t-seris collected in the resonant scanning modality in head-fixed awake animals free to run on a wheel (Fig. 4.1A). Hippocampal astrocytes specifically expressed GCaMP6f and fluorescence signals were collected from a FOV of area $16.4 \times 103 \mu\text{m}^2$ with a pixel size of $0.79 \mu\text{m}/\text{pixel}$ (Fig. 4.1B). We tested RASTA on dataset-2 using leave-one-out cross-validation method (Fig. B.11) whereas for dataset-3 (Fig. B.12) and dataset-4 (Fig. 4.5, App. B Tab. S6) the training of the algorithm was performed on dataset-1. In all cases, the detection F1-score of RASTA was comparable to the annotators' ones (Fig. B.11C, Fig. B.12C, Fig. 4.5C, and App. B Tab. S4, S5, S6). Similarly, the F1-score for somata and process segmentation achieved the accuracy level of human annotators (Fig. B.11F, Fig. B.12F, Fig. 4.5D, and App. B Tab. S4, S5, S6). Overall, these results demonstrate that RASTA detections and segmentation performance remains comparable to that of human annotators on never-before-seen datasets, regardless of the indicator and of the acquisition parameters used.

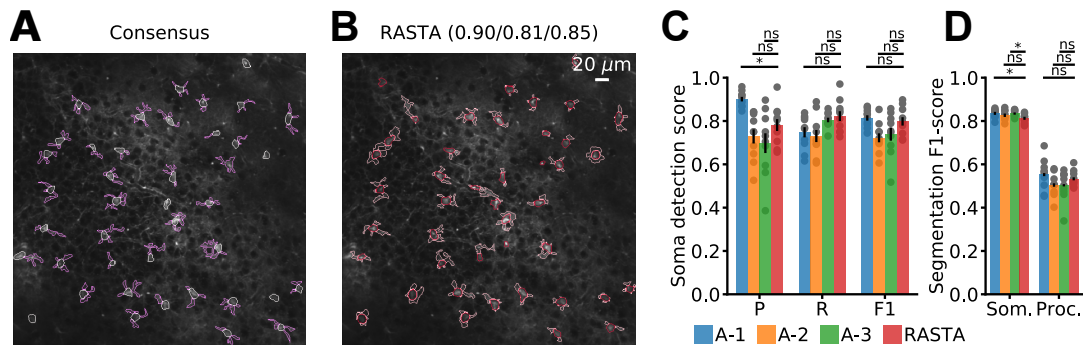


Figure 4.5: RASTA performance on never-before-seen data. A) Consensus annotation of FOV (Id: 1, dataset-4). B) RASTA segmentation on the same FOV shown in A. C) Soma detection performance is reported as precision (P), recall (R), and F1-score (F1) for the three human annotators (A-1, A-2, and A-3) and for RASTA. Two-sided Wilcoxon rank sum test $N=10$; LOOCV results. D) F1-score for segmentation of somata and processes for the three human annotators (blue, yellow, and green) and RASTA (red). Two-sided Wilcoxon rank sum test $N=10$; LOOCV results. See also table S5.

4.3 Methods

RASTA

RASTA is a semantic segmentation algorithm for astrocytic imaging data, its analysis workflow is characterized by two phases: training and inference. These two phases are organized in two analytic pipelines (Fig. 4.6 A-B). Each pipeline analyzes a dedicated dataset called training set and inference set, respectively. The training set is a subset of FOVs in the dataset used to optimize the algorithm. The inference set is the fraction of FOVs in the dataset used to evaluate the algorithm performance. The 2-photon time series recordings of astrocytes in the training set undergo a pre-processing procedure (Fig. 4.7 A); preprocessed data are used to optimize the DNN weights. Similarly, inference-phase starts with pre-processing where data are denoised and enhanced (Fig. 4.7 A). Then, the algorithm proceeds detecting putative cells which are segmented by the DNN. Following a detailed description of the modules that compose RASTA, and the two analytic pipelines.

Spatial Sharpening Module. This module consists in spatial sharpening and pixel intensity standardization of the median projection in time-series recording. First, the module subtracts from each frame the 10th percentile of the pixel intensities [58], then it computes the median projection on the entire stack. The median projection is useful to remove the residual motion artifacts that remain after motion correction and it enhances all the pixels that have localized activity during the entire time series. In order to standardize the images pixel values in the dataset, pixel intensity values have been rescaled as a 16-bit integer (i.e. within the interval [0; 216]). Image contrast has been improved by using clipping limited adaptive histogram equalization (CLAHE). To further improve the resolution of cell substructure this technique is combined with a sharpening kernel convolution (App. B Algorithm details: Spatial Sharpening Module). Overall, spatial sharpening module condenses information about the spatial location of astrocytic signals collected over time into a single, highly informative, spatial map.

Activity Map Generation Module. This module detects regions in FOVs characterized by spatially-localized high fluorescence intensity (see below), generating a putative “activity map”. To start, the input FOV is subsampled in overlapping patches (Fig. 4.7 B), each subject to independent statistical analysis. Each patch is a 3D tensor in time and space in which the intensity value of each 3D voxel is considered an independent sample. For each time t , Voxels- $v_{i,j}[t]$ where i,j are indexes over the patch dimension- are binarized setting their value to 1 if their fluorescence intensity value is greater than the N -th percentile of the voxels intensity distribution within the patch or to 0 otherwise. The N -th percentile is selected by optimization of the activity map generator performances on the training set (see below). Finally, a bi-dimensional (spatial) average projection of the binarized 3D tensors is generated

reporting the fraction of time in which the voxels $v_{i,j}$ were classified to 1. In the areas of patch overlap in the a bi-dimensional average projection, for each pixel the spatial average has been computed as the average value across patches. To provide biologically relevant constraints to this statistical filter, the number of astrocytes in each FOVs can be estimated as the ratio of the FOVs surface with respect to the area of an astrocytic domain. Here, each astrocytic domain is approximated as a circle of surface $\pi(d/2)^2$, where d is the characteristic diameter of an astrocytic domain (approx. $40\mu\text{m}$; [31]). The estimated number of astrocytes represents a lower bound for the number of active zones; in fact, the number of identified clusters can be greater than the estimated number of astrocytes because of portions of astrocytic bodies visible in the FOV or blood vessels appearing as active areas. Last, the algorithm identifies all the spatially contiguous active clusters of pixels on the bi-dimensional (spatial) average projection of the binarized 3D tensors, selecting clusters with surface greater or equal than a putative somata (approx. $40\mu\text{m}^2$). As a conservative initialization, pixels are considered active if their average projection value is greater than 0.6 (i.e. being classified to 1 on 60% of time frames). If the number of clusters identified is smaller than the estimated number of astrocytes the algorithm decreases by 0.03 the threshold for selecting active pixels. For each new threshold the putative somata surface area is decreased iteratively by $4\mu\text{m}^2$ starting from $40\mu\text{m}^2$ to $20\mu\text{m}^2$. This tuning process stops when the number of identified clusters is equal or greater than the estimated number of astrocytes the algorithm. This procedure aims to minimize the difference between the number of detected active regions and the theoretical astrocyte number.

The N-th percentile used to binarize the 3D tensor is tuned optimizing the performances of the activity map generator module on the training set. Performances of this module are evaluated computing the F1-score value between consensus somata annotations (see Manual Dataset Annotation section) and active zones identified in each FOV of the training-set. The performances are computed for a set of percentiles (30,40,50,60,70,80,90) and the one which maximize the F1-score is selected.

To sum up, this approach implements statistically auto-tuned local thresholds which detect regions in FOVs characterized by spatially localized high intensity of fluorescence. Moreover, it makes use of biological constraints providing a robust end-to-end strategy which does not require any manual parameter to set beyond pixel size.

Putative Bounding Boxes Extraction Module. This module computes centroids of high intensity of fluorescence zones detected by the activity map generation module and generates bounding boxes (BBs) surrounding them. BBs are $\approx 55\mu\text{m}$ high and wide with center in the coordinates of the centroids. These BBs are used to extract from t-series and spatial sharpened maps respectively (putative) single-cell recordings and (putative) single-cell spatial map.

Local Activity Filtering Module. This module performs a fine local time filtering. The first step, is to select the most active parts in the putative single-cell fluorescence recordings considering each pixel value in time in the 3D tensor an independent sample. It uses as threshold the 90th percentile of the pixels intensity distribution and binarizes the tensor. Then it selects pixels that are active for at least the $\alpha_1\%$ of the frames. Then the procedure is repeated setting to zero the previously selected pixels from the starting distribution and identifying pixels that are active for at least $\alpha_2\%$ of the frames. The binary mask obtained from the summation of the two previous set of pixels is used to generate a map (1 active 0 non-active pixels) to filter background regions from spatial single cell images. The filtering procedures were based on percentage of frames rather than absolute number of frames. This compensates for differences in frame numbers when considering different FOVs. $\alpha_1\%$ and $\alpha_2\%$ thresholds on activity are used to remove the background and eventually artifacts generated by spatial sharpening. The thresholds used in this module are tuned on the training set. The module explores a series of $\alpha_1\%$ and $\alpha_2\%$ couples in order to limit the number of removed consensus pixel under the 5% for both soma and processes (i.e. $\alpha_1=25$ and $\alpha_2=10$ for dataset-1). It is important to notice that concatenating 2 filters allows greater flexibility in the identification of background pixels and limits the bias to remove active regions characterized by low intensity of fluorescence (App. B Algorithm details: Local Activity Filtering Module).

Deep Neural Network Module. Astrocytes have a complex and articulated morphology composed by heterogeneous spatial patterns. Somata are compact structures with a simple geometric shape resembling an ellipsoid. Astrocyte arborizations conversely have extremely ramified structure that extends around the soma in a variety of shapes and directions. To segment these different structures, here we propose a new U-net [116] shape deep neural network (DNN) with new encoder building-blocks and new up sampling layers. Our design of this new DNN begun from a U-net [116] architecture with an encoder part (the descending part of the U shape in Fig. 4.7 C) that analyses the input image and a decoder (the ascending part of the U shape in Fig. 4.7 C)) that takes the information from the encoder and up-samples it to classify the pixels of the input image. The first two blocks of the encoder (L1 and L2 of the left part in Fig. 4.7 C) are two basic U-net blocks that analyze input image using convolutional filters. We then nested three pretrained Inception-Resnet-v2 modules [187] in our network (L3 to L5 levels in the left part in Fig. 4.7 C) changing its encoder backbone[188, 189]. This allows the encoder to incorporate a wider range of spatial dimensions simultaneously.

The decoder part of the U-Net (right part of Fig. 4.7 C) implements in 5 levels (L5 to L1), an up-sampling strategy that is a fundamental transformation operation to obtain a pixel-level prediction of the class with which each pixel should be labeled. In the Decoder part, we adopted Dense Up-sampling Convolution (DUC) to reduce the decoder number of weights [190].

To train all layers of both the encoder and decoder parts, we made use of a strong

data augmentation to limit algorithm overfitting problems caused by the relatively small size of the dataset. During training we used standard transformations [191] of input images: rotation by 90° , 180° , 270° , gaussian blurring with a 3×3 pixels kernel and $\sigma=3$, gaussian noise sampling values from a Gaussian distribution with $\mu = 0$ and $\sigma = 0.3$, salt and pepper noise on 4% of pixels, scaling of image size by factor 0.8 and 1.4, horizontal and vertical flipping, pixels intensity scaling by factors 3 and 0.5. Moreover we used morphological transformations, that alter the spatial structure of input images: elastic [116], barrel and pincushion transformations. This approach helps the net generalization process during training, since we are generating morphological new samples with realistic transformations (App. B Algorithm details: Data Augmentation). We combined a Binary-Cross-Entropy (BCE) loss with soft Dice loss [192]; BCE was applied to all the three classes soma, process, and background. Soft Dice has been applied only on soma and processes:

$$\mathcal{L}(X, \hat{X}) = -\frac{1}{N_b} \sum_{i=1}^{N_b} \left\{ \left(\sum_{c=1}^3 X_{ic} \log \hat{X}_{ic} \right) + \left[\sum_{c=1}^2 \left(1 - \frac{2 * X_{ic} * \hat{X}_{ic} + \epsilon}{X_{ic} + \hat{X}_{ic} + \epsilon} \right) \right] \right\} \quad (4.1)$$

where X and \hat{X} represent user defined mask tensor and prediction mask tensor, $\epsilon = 0.5$ is constant that preserve the numerical stability, N_b is the batch size and $c=1,2,3$ is the class index for: processes, soma and background. The role of DNN is to assign small region to the correct class, hence, the soft dice loss represents a proper metric to measure area overlapping accuracy. We trained the DNN using Adam Optimizer [193] and learning rate (lr, see App. B Tab. S7) using the 30% of the training set as validation set to monitor the the loss of the DNN. The number of training epochs is $N = N1+N2$. In the first $N1$ epochs of training the weights of pretrained blocks (Reduction Blocks and InceptionResNet Blocks) are not updated. During the remaining $N2$ epochs we performed a fine tuning of the entire net weights. All the filters that are trained since the first epochs are initialized as described in [188]. Training parameters are reported in App. B Tab. S7. $N1$ and $N2$ were chosen because the validation loss within these epochs always converged to a plateau within these epochs.

Cross Correlation Module. This module analyzes fluorescence intensity dynamics of pixels within the putative domain surrounding the semantically segmented astrocytic soma and processes ROIs (i.e. a circular region of radius approx. $38 \mu\text{m}$). We refer to the intensity fluctuations in time of each pixel as $s_I^l[t]$. This module is composed by two blocks - cross-correlation computation and threshold optimization- that are called iteratively. The cross-correlation computation block classifies a set of input $s_I^l[t]$ for $l = 1, \dots, L$ as correlated to a set of reference $s_R^k[t]$ for $k = 1, \dots, K$ given a threshold th_{cc} ; where L is the number of inputs and K is the number of references. The block computes the normalized cross correlation between each (l,k) pair (Eq. 4.2) and selects its maximum value (Eq.4.3). Then, the cross-correlation

matrix M_{cc} is defined as follow:

$$cc_{lk}[n] = \frac{1}{\sigma_I^l \sigma_R^k} (s_I^l[t] - \mu_I^l) \cdot (s_R^k[t+n] - \mu_R^k) \quad \text{for } n \in [-5, 5] \quad (4.2)$$

where μ_I^l and σ_I^l are respectively mean and standard deviation of $s_I^l[t]$ and μ_R^k and σ_R^k are respectively mean and standard deviation of $s_R^k[t]$.

$$m_{lk} = \max_n cc_{lk}[n] \quad (4.3)$$

and M_{cc} is defined as follow:

$$M_{cc} = \begin{bmatrix} m_{11} & \dots & m_{K1} \\ \vdots & \ddots & \vdots \\ m_{1L} & \dots & m_{KL} \end{bmatrix}$$

M_{cc} is then binarized selecting only values greater than threshold th_{cc} . $s_I^l[t]$ is classified cross-correlated if at least one element in the l th-row of M_{cc} is equal to one.

The threshold optimization block selects an optimal threshold using an iterative approach. A set of 250 pixels is sampled outside astrocyte domains in each FOV and their $s[t]$ are collected. This set represents a proxy over which we can compute the number of false positive selections obtained from the cross-correlation computation block using as a reference set the $s[t]$ extracted from ROIs pixels. Since pixels are sampled outside astrocytes domains these cannot belong to any subcellular region of astrocytes detected in the FOV. For this reason, we assume that the sampled pixels $s[t]$ are independent from the ones of the semantically segmented ROIs pixels. In the threshold optimization block the sampling-selection strategy is repeated 5 times for each threshold value in the range 0.60 to 0.95 with minimum spacing between values of 0.05. Finally, for each threshold the mean number of false positive pixels is computed. Then, this block selects as optimum threshold th_{Op} as the smallest threshold value with average false positive percentage error less than %5. Finally, for each detected cell the cross-correlation module collects all the pixel $s[t]$ in the circular region that surround it and all the ROIs pixels $s[t]$; then it applies the cross-correlation computation block on these two $s[t]$ sets using th_{Op} as threshold.

Training Pipeline. The training-phase is organized as a series of steps that end with the DNN training as shown in Fig. 4.6 A. First of all, the spatial sharpening module applied to the training FOVs generates spatial sharpened maps. Since cells in the training set are already mapped in the consensus segmentation the Putative Bounding Boxes Extraction module generates the BBs using the somata annotated in the consensus segmentation as input. In the BBs extracted from these maps there are no false positive cell so the DNN can be trained on unbiased samples. The Putative Bounding Box Extraction module generates a set of single cell spatial maps

and a set of single-cell recordings. The Local Activity Filtering module analyzes the single-cell recordings obtaining binary masks of foreground/background pixels. Finally, single cell images extracted from the spatial maps are filtered with these binary masks. This filter further denoise and enhance the so-obtained single cell spatial maps. Putative Bounding Boxes Extraction and Local Activity filtering modules are useful to take advantage of the temporal information of all the astrocyte calcium fluctuations, which had been compressed using the median projection. This pipeline ends after the training of the DNN with the so obtained single cell filtered spatial map images.

Inference Pipeline. The inference-phase starts with a pre-processing which generates of a set of putative filtered single-cell map from the inference set, as shown in Fig. 4.6 B. The pre-processing is organized in several steps where Spatial Sharpening, Activity Map Generation, Putative Bounding Boxes Extraction and Activity Filtering modules are applied. For each FOV, the spatial map and the activity map are generated by the Spatial Sharpening module and by the Activity Map Generation module, respectively (Fig. B.1 A). Then, the Putative Bounding Boxes Extraction module extracts the putative single-cell spatial maps and the putative single-cell recordings. Finally, the Activity Filtering module analyzes single-cell recordings and identifies non-informative zones. These zones are filtered from the single-cell spatial map (Fig. B.1 B). Subsequently, the filtered single-cell spatial maps are used to reconstruct a filtered spatial map of the entire FOV.

The DNN analyses the filtered single-cell spatial maps and, for each FOV these results are collected in as segmentation results. Then, the DNN analyses the FOV filtered spatial map providing for each cell the probability of being a true- or a false-positive. Cell probability is computed as the mean probability of pixels inside somata ROIs of being classified as soma-type pixels by the DNN. Cells with probability smaller than 0.9 are filtered from the FOV segmentation results (App. B Algorithm details: Cell-wise probability map). Finally, the segmented regions obtained are spatially filtered including only cells with identified soma area greater than $0.9 \cdot A_{min}$ and smaller than $1.1 \cdot A_{max}$, where A_{min} is the smallest somata area measured in the training dataset whereas A_{max} is the greatest somata area measured. Finally, identified processes are filtered if not spatially connected to an identified soma (App. B Algorithm details: Removal of DNN artifacts).

The last optional step consists in the refinement of the ROIs so obtained using the cross-correlation module. In fact, it identifies regions where calcium signals are cross-correlated with the semantically segmented ROIs signals in the FOV.

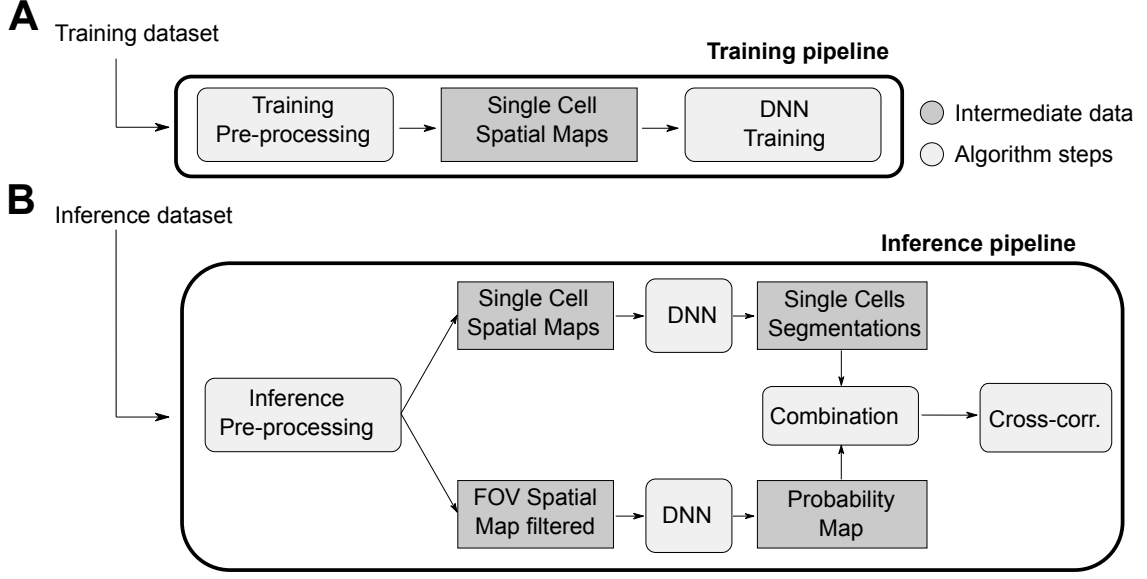


Figure 4.6: RASTA pipelines. A-B) Flowcharts of the training (A) and inference (B) pipeline.

Detection and Segmentation Metrics

We evaluated the detection performances of our algorithm by comparing RASTA somata segmentations with the manual consensus labels, as described in [181, 182]. We quantified three somata detection metrics: recall, precision, and F1 score, defined as follows:

$$Precision = \frac{N_{TP}}{N_{detected}} \quad (4.4)$$

$$Recall = \frac{N_{TP}}{N_C} \quad (4.5)$$

$$F1 = 2 \cdot \frac{Precision \cdot Recall}{Precision + Recall} \quad (4.6)$$

We defined these quantities as follows: number of manually labelled somata (consensus somata, N_C), number of true positive somata (N_{TP}) and number of somata detected ($N_{detected}$) [181, 182]. We matched masks between the consensus labels and the detected masks using the Intersection-over-Union (IoU) metric along with the Hungarian algorithm [194]. We computed the IoU metrics for 2 binary masks M_1 and M_2 as follows:

$$IoU(M_1, M_2) = \frac{|M_1 \cap M_2|}{|M_1 \cup M_2|} \quad (4.7)$$

Then we computed the distance matrix between any pair of masks in GT manual annotations set and in RASTA annotations set as described in [181, 182]. Each

element of this matrix has been computed as follows:

$$d(M_i^{GT}, M_j) = \begin{cases} 1 - IoU(M_i^{GT}, M_j) & \text{if } IoU(M_i^{GT}, M_j) \geq 0.5 \\ 0 & \text{if } M_i^{GT} \subseteq M_j \text{ or } M_i^{GT} \supseteq M_j \\ \infty & \text{if otherwise} \end{cases} \quad (4.8)$$

A distance of infinity corresponds to non-matching masks due to their small IoU score. Finally, we solved the matching problem applying the Hungarian algorithm to the distance matrix. The number of matched masks correspond to N_{TP} . Segmentation scores have been computed at the pixel level to quantify how complex structures like processes are segmented by RASTA. For each FOV we computed the segmentation score considering only the detected cell; when no detected cells were available in a FOV the segmentation score was discarded. The segmentation score was quantified by three metrics: recall, precision, and F1 score, defined in eq.4.4, eq.4.5, eq.4.6. We defined N_C number of manually labelled pixels, N_{TP} number of true positive pixels in the RASTA segmentation and $N_{detected}$ the number of pixels segmented by RASTA. We compute the F1-score for both somata and processes pixel-classes.

Cross-Correlation Error evaluation

Error estimation for the cross-correlation module has been performed computing the number of pixels outside astrocyte domains that are cross-correlated with the consensus ROIs pixels in each FOV. For each cell in the FOVs we sampled 1000 pixels outside the domain of the astrocytes avoiding pixels which were used to tune the cross-correlation threshold. This set is fundamental to compute the number of false positive selections for each astrocyte. Domains are estimated as a circular region of radius $38 \mu\text{m}$ surrounding each cell in FOVs. Then, we compute the number of false positive pixel per FOVi as:

$$FP(FOV_i) = \frac{\sum_{\substack{j=num. \\ of \\ cells}} fp(cell_j)}{N_C} \quad (4.9)$$

Where fp is the number of false positive pixels selected for cellj and N_C is the number of cells in FOV_i. We repeated this analysis for 100 iterations for each FOV.

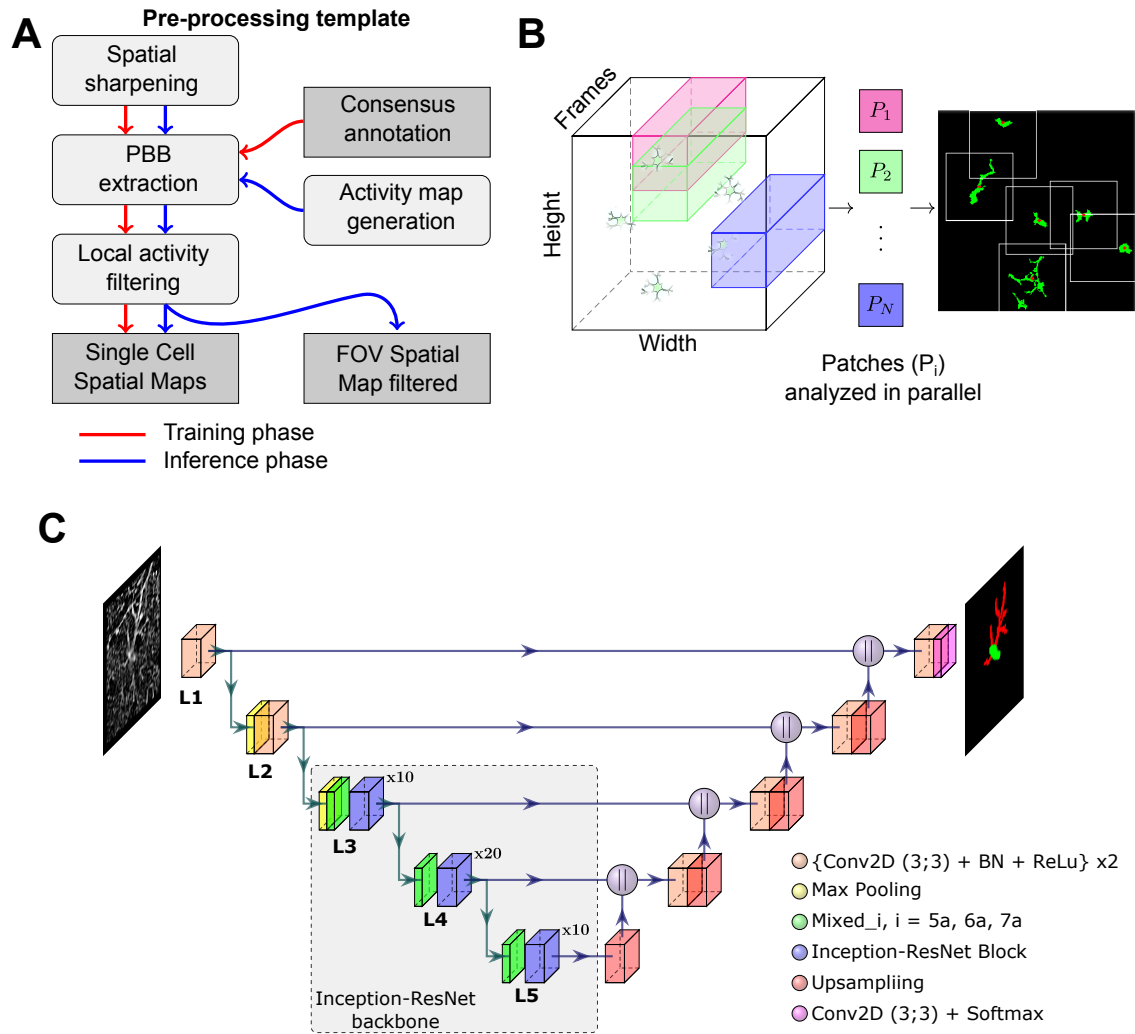


Figure 4.7: Schematic representation of RASTA modules. A) Flowchart of the pre-processing steps: i) generation of the spatial sharpening map (Spatial Sharpening); ii) extraction of putative bounding boxes (PBB Extraction); and iii) local activity filtering (LA Filtering) of single-cell images. Please note that extraction of single-cell images during pre-processing of the training set relies on ground-truth segmentation. Extraction of single-cell images during pre-processing of the inference set relies on the activity map generator (Activity Map Generation). B) Schematic representation of RASTA activity map generator: i) patch extraction; ii) patch parallel analysis; iii) clustering of active pixels. C) RASTA DNN architecture. In each level L_i with $i = (1, 2, 3, 4, 5)$, height (H) and width (W) of the input image is reduced by a factor $2i - 1$. Conv2D+BN+ReLu: this block is composed of two consecutive sequences of 3×3 convolutional filters (Conv2D) followed by batchnorm normalization (BN) and rectified linear unit (Relu). Caption continues on the next page.

Figure 4.7: Max Pooling: we used a kernel-size of (2,2), the size of the sliding window where the maximum value of the input tensor is taken, resulting in input tensor of dimensions H and W reduced to $H/2$ and $W/2$. Mixed-i: in L3 we used Mixed-5a, in L4 we used Mixed-6a and in L5 we used Mixed-7a from Inception-ResNetv2 implementation in [187]. Inception-ResNet Block: in L3 the block is composed as (Inception-ResNet-A, Block35)x10, in L4 the block is composed by (Inception-ResNet-B, Block 17)x20 and in L5 the block is composed by (Inception-ResNet-C, Block8)x10 from Inception-ResNetv2 implementation in [187]. Upsampling: we adopted dense upsampling convolution (DUC, [190]) to perform the upsampling on the input tensor. The input tensor dimensions are $H \times W \times D$ and they are transformed to $(2H) \times (2W) \times (D/4)$. Conv2D+Softmax: this block is composed by a 3x3 convolutional filter and a Softmax transformation.

Reconstruction of astrocytic morphology from spatio-temporal map of AQuA

Starting from the spatio-temporal map of Ca^{2+} events resulted from AQuA [176] we reconstructed astrocytic morphology since a subset of pixels classified as events should in principle belong to astrocytic somata and processes. For each astrocyte detected in the consensus annotation, we run AQuA in circular regions of radius 38 μm surrounding these cells, thus limiting the analysis to the putative astrocytic domain. Using putative Ca^{2+} events detected by AQuA we select the pixels belonging to a minimum number of events. For each astrocyte the minimum number of events was tuned as the value that maximize F1-score between the selected set of pixels and the consensus annotation (soma+processes). Hence, we computed precision, recall and F1-score between the best reconstruction and the consensus annotation. This strategy provides the F1-score upper bound for the reconstruction astrocytic morphology using AQuA.

Time Analysis

We measured RASTA processing time for the whole inference pipeline, repeating the analysis over 10 iterations. We used the following computing architecture, a Linux based workstation (Ubuntu 18.04.3 LTS distribution) equipped with 20 Intel(R) Core (TM) i9-9900X CPU clocked @ 3.50GHz, 130 GB of RAM, and 3 INVIDIA GeForce RTX 2080 Ti GPUs. To allow for performance comparison across different configurations of hardware resources, we used a $26.3 \times 103 \mu\text{m}^2$ FOV, changing artificially the t-series length from 300 to 700 frames. We compared three computational resource configurations: 4 CPUs, 20 CPUs, and 20 CPUs + 1 GPU (Fig. B.14 A). These configurations were chosen to investigate RASTA performance across hardware settings, from laptop-like performance (i.e., 4 CPUs) to high-performance workstation equipped with computing accelerators (i.e., 20 CPUs and 20 CPUs + 1 GPU).

We found, as expected, that for detecting and semantically segment somata

and processes of astrocytes the 4 CPUs configuration was the slowest configuration (mean \pm std 12.33 \pm 0.08 s for 700 frames), whereas on the 20 CPUs configuration the usage of a GPU accelerator reduces the processing time of RASTA (mean \pm std with GPU 7.27 \pm 0.03 s, without GPU 10.80 \pm 0.09s for 700 frames).

The cross-correlation module is a very time-consuming block in the inference pipeline, as pixels in astrocyte domains are classified as correlated or uncorrelated with the semantically segmented astrocyte pixels ROIs. We found that GPU computational power can be used to sensibly reduce the execution time (mean \pm std 0.919 \pm 0.004 s for 90s t-series) if compared to 20 CPUs implementations (mean \pm std 19.23 \pm 0.09 s for 90s t-series) and 4 CPUs implementation (mean \pm std 26.39 \pm 0.04 s for 90s t-series; Fig. B.14 B).

We also measured the processing time for detecting and semantically segment somata and processes of astrocytes for large scale and high sampling rate recordings using the 20 CPUs + 1 GPU computational resources configuration. These recordings are challenging data due to either the large number of astrocytes in the mesoscopic FOV or the number of frames obtained with resonant-galvo scanning. We measured processing time of the inference pipeline for 10 iterations on 0.16 mm² and 0.26mm² changing artificially the t-series length from 1000 to 5000 frames (Fig. B.14 C). We found that RASTA can analyze fast these large scale and high sampling rate recordings (mean \pm std 22.1 \pm 0.3 s for 0.16 mm² FOV and 25.7 \pm 0.1s for 0.16 mm² FOV both composed by 5000 frames).

Overall, RASTA enables rapid semantic segmentation of astrocytes in two-photon t-series, facilitating the analysis of astrocytic calcium signals in vivo and enabling new experimental approaches on mesoscopic FOVs. Clearly, more computational resources, such as those available in High Performance Computing clusters, can further reduce the computation time of RASTA (Fig. B.14 D), however RASTA can already analyze t-series faster than the duration of t-series without requiring large amount of computational resources.

DATASET

Mice. All experiments involving living animals were approved by the National Council on Animal Care of the Italian Ministry of Health and carried out in accordance with the guidelines established by the European Communities Council Directive authorization (61/2019-PR). All data were collected from male C57BL/6J mice (Charles River, Calco, Italy). From postnatal days 30, animals were separated from the original cage and housed in groups of up to five littermates per cage with ad libitum access to food and water in a 12-hours light-dark cycle. All the preparative and experimental procedures were conducted on animals older than 10 weeks.

AAV injection and chronic hippocampal window surgery. Animals were anesthetized with 2% isoflurane 0.8 % oxygen, placed into a stereotaxic apparatus (Stoelting Co, Wood Dale, IL), and maintained on a warm platform at 37°C for the

whole duration of the anesthesia. Before surgery, a bolus of Dexamethasone (Dexadreson, 4 gr/kg) was injected in the animal's hamstring. After scalp incision, a 0.5 mm craniotomy was drilled on the right hemisphere (1.75 mm posterior, 1.35 mm lateral to bregma), the AAV-loaded micropipette was lowered into the hippocampal CA1 region (1.40 mm deep to bregma). 0.8 μ l of AAV solution containing pZac2.1 gfaABC1D-cyto-GCaMP6f (Addgene viral prep - 52925-AAV5) was injected at 100 nL/min by means of a hydraulic injection apparatus driven by a syringe pump (UltraMicroPump, WPI, Sarasota, FL). Following the viral injection, a stainless-steel screw was implanted on the cranium of the left hemisphere and a chronic hippocampal window was implanted on the contralateral hemisphere similarly to [124, 128]. In brief, a trephine drill was used to open a 3 mm craniotomy centered at coordinates 2.00 mm posterior and 1.80 mm lateral to bregma. The dura was removed using fine forceps, and the cortical tissue overlaying the hippocampus slowly aspirated using a blunt needle coupled to a vacuum pump. During aspiration the exposed tissue was continuously irrigated with normal HEPES-buffered artificial cerebrospinal fluid (ACSF). Aspiration was stopped once the thin fibers of the external capsule were exposed. An optical window was fitted to the craniotomy in contact to the external capsule and a thin layer of silicone elastomer (Kwik-Sil, World Precision Instruments) was used to surround the interface between the brain tissue and the steel surface of the optical window. A custom stainless-steel head-plate was attached to the skull using epoxy glue. All the components were finally fixed in place using black dental cement and the scalp incision was sutured to adhere to the implant. All the animals received an intraperitoneal bolus of antibiotic (BAYTRIL, Bayer, Germany) to prevent postsurgical infections.

Optical windows. Optical windows were composed of a thin-walled stainless-steel cannula segment (OD, 3 mm; ID, 2.77 mm; height, 1.50 - 1.60 mm). A 3.00 mm diameter round coverslip was attached to one end of the cannula using UV curable optical epoxy. Sharp edges and bonding residues were smoothed using a diamond coated burr.

2-photon imaging in awake head-restrained mice. The optical setup for 2-photon imaging was composed of a pulsed laser source (Chameleon Ultra, 80 MHz repetition rate tuned at 920 nm, Coherent) and Bruker Ultima Investigator equipped with 6 mm raster scanning galvanometers, movable objective mount, 16x/0.8 NA objective (CFI75 LWD 16X W, Nikon, Milan), and multi-alkali photomultiplier tubes. Laser beam intensity was adjusted using a Pockel cell (Conoptics Inc, Danbury). Laser beam power at the objective outlet was 90-110 mW. GCaMP6f or TdTomato emission signal was collected by the PMT detector after band-pass filtering (525/70 nm) and digitalized in 12 bits. Imaging sessions have been conducted in raster scanning mode. One or two weeks after surgery the animals were handled by the operator for a minimum of two days and then were habituated to the imaging setup. Starting from the second session, the animals were head-restrained for a progres-

sively increasing amount of time reaching 1 hour in approximately one week. Mice were free to run on a custom 3D printed ABS wheel. Experimental sessions lasted approximately one hour. After each session, animals were returned to their home cages.

Motion correction . t-series were motion corrected using a customized implementation of the open-source up-sampled phase cross-correlation algorithm [154, 155]. We used the t-series median projection as reference frame.

Dataset-1. The first 2-photon calcium imaging dataset used to test our algorithm is composed by 24 FOVs of hippocampal astrocytes expressing GCamp6f indicator recorded in awake mice with galvo microscope. The dataset was recorded from head-fixed mice running on a wheel. It is composed by 15 FOVs with 550 frames and 9 FOVs with 750 frames each 256x256 pixels resolution ($0.634 \mu\text{m}/\text{pixel}$). The temporal sampling rate of t-series in this dataset is 3.0 frames/s.

Dataset-2. The second 2-photon calcium imaging dataset used to test our algorithm is composed by 8 FOVs of hippocampal astrocytes expressing TdTomato indicator recorded in awake mice. The dataset was recorded from head-fixed mice running on a wheel. It is composed by 4 FOVs recorded with galvo microscope and 4 FOVs recorded with resonant microscope. FOVs dimensions are 512x512 pixels with $1.057 \mu\text{m}/\text{pixel}$ of resolution. FOVs recorded with galvo microscope are composed by 250 frames. In the 4 FOVs recorded with resonant microscope subset there are 2 FOVs with 5500 frames, a FOV with 1200 frames and a FOV with 9000 frames. The temporal resolution of t-series recorded with galvo microscope is 0.8 ± 0.1 frames/s whereas the temporal resolution of t-series recorded with resonant microscope is 30.2 ± 0.2 frames/s.

Dataset-3. The third 2-photon calcium imaging dataset used to test our algorithm is composed by 7 FOVs of hippocampal astrocytes expressing TdTomato indicator recorded in awake mice with resonant microscope. The dataset was recorded from head-fixed mice running on a wheel. It is composed by 5 FOVs with 5500 frames, a FOV with 4500 frames and a FOV with 9000 frames each 512x512 pixels resolution ($0.793 \mu\text{m}/\text{pixel}$). The temporal resolution of t-series in this dataset is 29.9 frames/s.

Dataset-4. The fourth 2-photon calcium imaging dataset used to test our algorithm is composed by FOVs of hippocampal astrocytes expressing GCamp6f indicator recorded in awake mice with resonant microscope. The dataset was recorded from head-fixed mice running on a wheel. It is composed by 10 FOVs with 9000 frames each 512x512 pixels resolution ($0.793 \mu\text{m}/\text{pixel}$). The temporal resolution of t-series in this dataset is 29.9 frame/s.

Simulated datasets. We performed a set comparative analyses manipulating the noise levels into FOV t-series. Specifically, starting from dataset-1 we generated 4 artificial datasets with increased noise levels. We started estimating the standard deviation σ for each pixel in the FOVs, then we computed a novel temporal intensity trace adding zero mean gaussian noise with $\beta \cdot \alpha$ standard deviation to the observed raw trace. Each artificial dataset was characterized by a different β noise scaling factor (0.5, 1, 1.5, 2). Then, we generated 2 datasets with reduced background pixels intensity. For each FOV we defined as background all the pixels outside the consensus annotations. We scaled background pixel intensity by a factor λ , exploring two λ values (0.75 and 0.5).

PSNR evaluation. We evaluated the peak signal to noise ratio (PSNR) of a FOV with N astrocytes as follow:

$$PSNR(FOV_i) = \frac{1}{N} \sum_{j=0}^N \frac{\max_t y_j[t]}{\sigma_j^{baseline}} \quad (4.10)$$

Where $y_j[t]$ is the mean fluorescence signal in astrocyte ROIs and $\sigma_j^{baseline}$ is the standard deviation of the baseline distribution of fluorescence values of the astrocyte. To compute the baseline distribution of each astrocytes we considered only pixels inside the astrocyte domain (circular area of radius approx. $38 \mu\text{m}$). The values of these pixels across time form the full fluorescence distribution. Then the baseline distribution consists in all the fluorescence value smaller than the 80-percentile of the full fluorescence distribution.

Manual dataset annotation. Motion corrected t-series were pre-processed with the spatial sharpening module. The consensus generation process is composed by 2 steps. As a preliminary step 3 expert annotator independently labeled the dataset using the freehand and ROI Manager tools of Fiji [195] following these rules: first, annotators used the recordings to detect visible astrocytic somata. Then the spatial maps have been used to select and label region of interests (ROIs) identifying visible astrocytic somata and processes; last, annotators sequentially added ROIs defining the contours of the optically resolved proximal processes showing active calcium dynamics and presumably belonging to the same astrocyte. Hence, as second step they solved the inconsistencies between their annotations reaching a final consensus [181] as follows. The annotations of the 3 annotators have been combined in overlapping masks (Fig. B.2), highlighting annotators discrepancies. Each soma or process identified by less than 3 annotators has been added or removed from final consensus after an ad-hoc review where the annotators observed both the preprocessed spatial maps and motion corrected t-series. Finally, consensus ROIs have been generated ex-novo starting from the somata and processes ROIs accepted consensually by annotators. Consensus ROIs have been reviewed and accepted by all the annotators during the generation.

Algorithm Open-source implementation and Datasets availability

RASTA has been developed in Python3.6[164] and PyTorch 1.2[196], the code is publicly available at (<https://github.com/jbonato1/RASTA>). The repository contains documentations, Docker [197] image for fast installation, jupyter notebook tutorials, bindings for widely used software (Fiji[195] and MATLAB (MathWorks)), visualization and analysis tools, and a message/discussion board. DNN weights are available for all the datasets used in this study, allowing novel users to run analysis on new small datasets. RASTA uses several open-source libraries like OpenCV [198], scikit-learn [199], scikit-image [155] and Scipy [200].

Quantification and Statistical Analysis

For all the statistical test of detection and segmentation performances, we performed two-sided Wilcoxon rank test; n.s., not significant, * $P < 0.05$, ** $P < 0.005$ and *** $P < 0.0005$. When we performed multiple statistical comparisons between detection and segmentation performances between annotators and RASTA we corrected the statistical test results using Holm–Bonferroni method [201]. We did not remove any data from statistical analyses as outliers.

Chapter 5

Conclusions

5.1 Complementary encoding of spatial information in hippocampal astrocytes

We have shown for the first time that information encoding during virtual spatial cognition is not a phenomenon restricted to neural circuits, but also involves the nearby astrocytic network. We observed that spatial information was encoded in both somata and processes of astrocytes, consistent with the complexity and compartmentalization of calcium signals in astrocytes [59, 75, 92, 93, 98, 118]. Interestingly, individual astrocytes can encode multiple place fields through their different subcellular compartments. This phenomenon suggests how multiple neuronal spatial representations can be integrated by astrocytes. Moreover, we observed that astrocytic and neuronal signals are both complementary and synergistic, and their combination significantly increases the amount of information about the animal's position. The diversity of position tuning and position-dependent correlations between astrocytic and neuronal ROIs represents the mechanism by which it is possible to observe complementary and synergistic information, as previously observed by [131] on neuronal ROIs. Another source of complementarity may be the integration of several different neuronal inputs encoding different stimuli [202–204].

A widely accepted model of tripartite synapses [134, 139] describes how neuronal neurotransmitter release at the synaptic cleft can activate receptors in the plasma membrane of astrocytic processes. Astrocytic receptors, which enwrap both the presynaptic and postsynaptic terminals, can cause the release of intracellular calcium ions after activation. Consistent with this model, previous *in vivo* studies of astrocytic calcium signaling described that astrocyte activity reflects nearby neuron activity [46, 58, 109]. However, our study [111] has used an information-theoretic approach to show that spatial information in astrocytes is complementary to that encoded by nearby neurons. This fundamental finding opens up a number of important questions about molecular, anatomical, and functional aspects of astrocytic networks and how these networks relate to neuronal networks in the CNS. For example, the different molecular mechanisms regulating intracellular calcium

signaling in astrocytes and neurons may be involved in information complementarity. In fact, presynaptically released neurotransmitters reach postsynaptic neuronal terminals in the synaptic cleft and also thin astrocytic processes outside the cleft. Could these two distinct channels of signal transduction be involved in generating information complementarity? These open questions need to be addressed in future studies combining both experimental and modeling work.

Our information-theoretic approach has revealed some statistical properties such as complementarity and synergy of neuronal and astrocytic networks, but it is not sufficient to reveal any causal relationships between information encoded in astrocytes and circuit function or behavior. For this reason, it is critical to investigate how perturbation of astrocyte activity affects the neural network and its spatial representation to elucidate how both networks function [140]. One possible experiment is to manipulate astrocytic calcium dynamics with high spatial and temporal resolution [141–143] using the pharmacogenetics [174, 205] technique while imaging pyramidal neurons in the CA1 hippocampal region of head-fixed mice walking in a virtual corridor. If perturbation of astrocytic calcium dynamics affects the neuronal representation of space, the complementary/synergistic place dependence of astrocytic calcium dynamics may play a crucial role in the emergence of dynamic, context-dependent changes in the population coding of CA1 neurons. For these reasons, manipulation experiments and a comprehensive analysis of information processing in the neuronal network are essential for clarifying the relationships between neuronal and astrocytic networks in the hippocampus.

Recent models describing hippocampal functions consider only populations of neurons [144–147]. These populations encode information about the external environment which are essential for spatial navigation or memory formation. This representation of the hippocampus, in which only neurons play a fundamental role in encoding spatial information during spatial navigation tasks, needs to be updated to include astrocytic activity. Indeed, using an information-theoretic analysis, we found that spatial information is also encoded in the calcium dynamics of astrocytes (nonneuronal elements) and in their position-dependent interaction with neurons. Moreover, this information is not available in CA1 neuron activity or in their interactions. This nonneuronal information reservoir and the information-coding interaction between neurons and astrocytes represent two novel and unanticipated cellular mechanisms in hippocampal circuitry.

A key aspect concerning neuronal place cells in the hippocampus is the change in their firing patterns in response to seemingly minor changes in sensory or cognitive input, termed "remapping" by Muller and colleagues (see [206]), as place cells remapped their representation of space (see [207] for a review). Depending on changes in sensory or cognitive input, place fields may appear, disappear, or move to unpredictable locations [206]. It has been observed the place cells remapping when animals are placed in a new environment. A random set of $\approx 25\%$ of neurons in the entire population encodes the new environment [208–214], these new place cells cannot be predicted based on the place cells of the familiar environment. Remapping

has also been observed in the same environment but under light and dark conditions [215]. In general, the occurrence of remapping depends on several factors, including the extent of differences between environments [210], the prior training experience of the animals [215, 216], and also task switching in the same environment [217]. In addition, the motivational state of the animal and the behavioural context also play a role when remapping was observed in hippocampal place cells [218].

This phenomenon, which occurs in response to changes in behavioural context, suggests that the animal is able to create alternative representations of space in terms of different consequences associated with similar stimuli. However, Does this phenomenon occur also in astrocytes? If so, how does remapping take place in astrocytes and how is it related to nearby neurons? Investigating and characterising these aspects in relation to astrocytes exhibiting spatial encoding is essential to clarify how space is encoded in the hippocampus between the neuronal and astrocytic networks.

These aspects are also closely related to the mechanism of place cell formation in the hippocampus (review [219]). The cellular and circuit mechanisms that contribute to the formation of new place fields in the CA1 hippocampal area when animals are exposed to novel environments are an active area of research in neuroscience [208–214]. 3 functional neuron types were observed to occur in a novel environment [213, 220–222]. The instant place cells fire somatic action potentials (AP) during the first animal crossings of the place field. The delayed place cells fire somatic AP only after the animal has crossed the field several times. Finally, there are silent cells that rarely fire somatic APs even after multiple crossings of the place field. Are these 3 classes of neurons present in astrocytic networks? The mechanism of formation of spatial position encoding in astrocytes is a fundamental aspect that has to be investigated together with the neuronal one. In fact, astrocytes can modulate the activity of surrounding synapses and neurons and this may play an important role during place cells formation.

5.2 Optimizing measures of information encoding in astrocytic calcium signals

In [115] we generated astrocytic Ca^{2+} responses with realistic dependences of activity on external variables. Thanks to these simulations, we investigated how to use information theory to optimally tune hyperparameters and analysis procedures for a given experiment.

The direct estimates of mutual information obtained by plugging the empirical probabilities into the information equations and using a simple discretization of either the Ca^{2+} signals or the behavioural data work well. In fact, we measured quite high statistical power with a false positive detection rate that never exceeds the specified selection threshold for the p-value.

Application of these techniques to astrocytic functional imaging data in vivo [111]

reliably demonstrated how a number of subcellular astrocytic compartments in the CA1 hippocampus carry information about spatial position that is also genuine and unrelated to visual stimuli. These results support the emerging new view of the computational network in the hippocampus, in which not only neurons are involved in information processing, but also astrocytes form an additional network involved in these computations.

The effects of data non-stationarity, such as changes in the spatial alignment of ROIs over time, can be explored in future technical work by combining our information calculations and selection criteria with conservative criteria that rule out these effects. For example, the "reliability" criteria of Ca^{2+} activity across trial blocks (used in [111]) measures the stability of the spatial field of ROIs and classifies them as reliable or not.

Theoretical work has shown that correlations between neurons significantly affect the amount of information encoded in a population of neurons. A fundamental technical work that can be explored to expand this study is the effect of correlations between pairs of astrocytic ROIs and how to optimally set the hyperparameters of the information theoretic measurements for this scenario. In the simulations used in this work, it is possible to include pairwise correlations between Ca^{2+} signals from two simulated ROIs.

In neuronal literature, the role of pairwise correlation has been extensively studied, and two types of pairwise correlations have been formalized [223]. The first are signal correlations, which measure the similarity of stimulus tuning between neurons. Neurons tuned to the same stimuli, for example, have high signal correlations. The second is noise correlations, which quantify the neurons' correlation in single trial responses for a given stimulus (see review [224]).

Noise correlations capture correlations that go beyond the stimulus tuning shared by neurons. For example, if two neurons exhibit a positive noise correlation, on a single trial one neuron typically responds more strongly than usual to a given stimulus if the other neuron also responds more strongly than usual, and similarly if the response of both neurons is less strong than usual [132, 225–228]. Importantly the relationship between signal and noise correlations is a crucial factor that determine the amount of information encoded in a population. When signal and noise correlations are both positive or negative, signal and noise have similar response distributions, so the overlap between the response distributions will increase compared to a scenario without noise correlations. If, on the other hand, signal and noise correlations have opposite signs, such as in a pair of neurons that respond more strongly to different stimuli (negative signal correlation) but have a positive noise correlation, then the overlap between the response distributions to different stimuli will decrease thanks to the noise correlation. In this case, the amount of encoded information increases. Moreover, if noise correlations are stimulus-dependent, they can act as a complementary coding mechanism in addition to the firing rates of individual neurons [132, 225, 229, 230], which increases the information encoded in the population activity.

Thus, a first important open problem is to generate astrocytic simulations in which the signal and noise correlations are realistic and can be varied covering all the possible combination of signs. These types of simulations are fundamental to the study of the sufficient amount of data and optimal discretization strategy that must be used to investigate information processing in astrocyte populations in order to obtain reliable results.

5.3 Rapid spatiotemporal analysis of astrocytic calcium dynamics using deep learning

Thanks to advances in calcium imaging technology, this experimental imaging method has become one of the most important approaches for studying astrocyte calcium dynamics. RASTA provides experimenters with a scalable, machine learning-based, and reproducible tool to study circuitual components of astrocytes. The main purpose of chapter 4 is to present a detailed description of the RASTA method and its performances on various datasets.

RASTA is organized into fast training and inference pipelines combining efficient preprocessing, deep neural network (DNN), and numerical approaches. Overall, RASTA provides a valuable tool for rapid segmentation of astrocytes, allowing precise identification of somata, processes, and regions temporally correlated with them.

RASTA preprocessing performs efficient feature engineering on 2-photon images of astrocytes and extracts spatial and temporal features of astrocytes in the FOVs. Thanks to this preprocessing and transfer learning optimization strategy, the DNN embedded in RASTA can be optimized on a relatively small training set when compared to the standard state-of-the-art datasets used in computer vision [186, 231–233]. The performance of RASTA strongly depends on the efficient extraction of spatial and temporal information from the 2-photon images. Indeed, we found a significant drop in performance when the preprocessing steps were systematically excluded from the RASTA pipelines. Moreover, this configuration of RASTA allows for high robustness to noise, which is extremely important for *in vivo* recordings. When simulating different signal-to-noise regimes, we observed a significant decrease in recognition performance only in dataset with high noise. Nevertheless, we measured an increase in the detection and processes segmentation performance of RASTA when the signal-to-noise ratio was artificially increased.

Finally, RASTA is a fast and scalable end-to-end analysis tool. Its pipeline blocks have been massively parallelized on GPUs, which significantly reduces computation time for both training and inference.

To evaluate the performance of RASTA under different conditions, we used 4 datasets that differ in spatial magnification, scanning mode, and fluorophore types. These 4 datasets are provided to aid in the development of future tools for analysing astrocyte calcium dynamics.

We also used 3 different annotators to identify and segment somata and processes in these datasets. We combined these annotations into a consensus annotation that represents the best approximation to ground truth segmentation of astrocytes. Clearly the identification of the consensus ground truth is a fundamental step to optimize RASTA output, which ideally requires a community based effort.

Compared to the consensus annotation, the annotator results show a comparable level of disagreement in all the datasets used. This highlights two fundamental problems with human annotation: the difficulty of the manual annotation process and the non-reproducibility of this laborious task. Clearly, the analysis of astrocyte dynamics should not be hindered by these problems, and the development of scalable and reproducible software for the identification and segmentation of astrocyte circuit components is of paramount importance. Once trained on an accepted ground truth, RASTA provided reliable and reproducible segmentation, avoiding human operator-dependent variability.

RASTA achieved near-human performance in both detection and segmentation tasks in each of the 4 datasets used, regardless of spatial magnification, scanning mode, and fluorophore types. These results demonstrate flexibility of RASTA in detecting and segmenting astrocytes under different experimental conditions. Moreover, dataset- 3 and 4 results in both detection and segmentation tasks show the generalization capabilities of RASTA to new experiments, characterized by different spatial magnification and scanning mode, without any further optimization. In fact in these two cases, the optimization of RASTA hyper-parameters and DNN has been performed on dataset-1. However, when data features change drastically from the dataset for which RASTA was originally optimized (e.g., spatial magnification in dataset-2 or astrocytes are imaged from a cortical area instead of the hippocampus), further training is essential to achieve approximately human performance. In addition, it is fast, reproducible, and free of user-defined parameters, which can consequently improve both the scalability and reproducibility of astrocyte dynamics analysis pipelines. Furthermore, we have shown that RASTA outperforms state-of-the-art neuron detection software [177–182]. The failure of these models on these datasets can be attributed to 2 main differences between neurons and astrocytes, the extremely complex spatial morphology of astrocytes and the completely different dynamics of calcium signals between neurons and astrocytes. Similarly, RASTA outperforms state-of-the-art astrocyte segmentation software [98], which relies heavily on user-defined parameters.

Studies on the relationship between Ca^{2+} signals from astrocytes in their circuit components and surrounding neural circuits can benefit from RASTA outputs. In fact, identification of somata, processes, and correlated regions is the first step after which circuit components can be isolated from astrocytes. On the other hand, a recent algorithm, Astrocyte Quantitative Analysis (AQuA [176]), allows to identify and characterize spatio-temporal patterns of Ca^{2+} signaling in astrocytes through the detection of local increase-decrease of Ca^{2+} . However, these local fluorescence fluctuations cannot be readily related to morphological dynamics analysis unless the

circuit components of astrocytes have already been classified. Therefore, RASTA and Ca^{2+} event detection methods such as AQUA offer complementary approaches for the analysis of calcium signals in astrocytes. In fact, RASTA results are fully compatible with Aqua, where identified ROIs and correlated regions can be used as a morphological map where Ca^{2+} events detection can be performed.

Increasing evidence shows that activity-dependent astrocytic calcium signals are very information-rich and involved in high-level network responses [46, 86, 109, 175]. Therefore, semantic segmentation with RASTA is a valuable tool to study how different astrocytic subregions encode information [111, 112]. In addition, the rapid and automated workflow of RASTA enables rapid analysis of extensive recordings of astrocytic calcium signals, allowing for time-critical experimental approaches.

Bibliography

1. Morrison, R. S. & de Vellis, J. Growth of purified astrocytes in a chemically defined medium. *Proceedings of the National Academy of Sciences* **78**, 7205–7209 (1981).
2. Bowman, C. L. & Kimelberg, H. K. Excitatory amino acids directly depolarize rat brain astrocytes in primary culture. *Nature* **311**, 656–659 (1984).
3. Kettenmann, H, Backus, K. H. & Schachner, M. Aspartate, glutamate and γ -aminobutyric acid depolarize cultured astrocytes. *Neuroscience Letters* **52**, 25–29 (1984).
4. Cornell-Bell, A. H., Finkbeiner, S. M., Cooper, M. S. & Smith, S. J. Glutamate Induces Calcium Waves in Cultured Astrocytes: Long-Range Glial Signaling. *Science* **247**, 470–473 (1990).
5. Araque, A., Sanzgiri, R. P., Parpura, V. & Haydon, P. G. Calcium Elevation in Astrocytes Causes an NMDA Receptor-Dependent Increase in the Frequency of Miniature Synaptic Currents in Cultured Hippocampal Neurons. *The Journal of Neuroscience* **18**, 6822 –6829 (1998).
6. Bezzi, P *et al.* Prostaglandins stimulate calcium-dependent glutamate release in astrocytes. *Nature* **391**, 281–285 (1998).
7. Barres, B. A. The Mystery and Magic of Glia: A Perspective on Their Roles in Health and Disease. *Neuron* **60**, 430–440 (2008).
8. Kim, S. U. & de Vellis, J. Microglia in health and disease. *Journal of Neuroscience Research* **81**, 302–313 (2005).
9. Kettenmann Hand Hanisch, U.-K., Noda, M & Verkhratsky, A. Physiology of Microglia. *Physiological Reviews* **91**, 461–553 (2011).
10. Filiano, A. J, Gadani, S. P & Kipnis, J. Interactions of innate and adaptive immunity in brain development and function. *Brain Research* **1617**, 18–27 (2015).
11. Nimmerjahn, A., Kirchhoff, F. & Helmchen, F. Resting Microglial Cells Are Highly Dynamic Surveillants of Brain Parenchyma in Vivo. *Science* **308**, 1314–1318 (2005).

12. Parkhurst, C. N. *et al.* Microglia Promote Learning-Dependent Synapse Formation through Brain-Derived Neurotrophic Factor. *Cell* **155**, 1596–1609 (2013).
13. Torres Land Danver, J *et al.* Dynamic microglial modulation of spatial learning and social behavior. *Brain, Behavior, and Immunity* **55**, 6–16 (2016).
14. Kierdorf, K & Prinz, M. Microglia in steady state. *The Journal of Clinical Investigation* **127**, 3201–3209 (2017).
15. Elmore, M. R. *et al.* Colony-Stimulating Factor 1 Receptor Signaling Is Necessary for Microglia Viability, Unmasking a Microglia Progenitor Cell in the Adult Brain. *Neuron* **82**, 380–397 (2014).
16. Elmore, M. R. P., Lee, R. J., West, B. L. & Green, K. N. Characterizing Newly Repopulated Microglia in the Adult Mouse: Impacts on Animal Behavior, Cell Morphology, and Neuroinflammation. *PLOS ONE* **10**, e0122912 (2015).
17. Bruttger, J *et al.* Genetic Cell Ablation Reveals Clusters of Local Self-Renewing Microglia in the Mammalian Central Nervous System. *Immunity* **43**, 92–106 (2015).
18. Nave, K.-A. Myelination and support of axonal integrity by glia. *Nature* **468**, 244–252 (2010).
19. Ffrench-Constant, C & Raff, M. C. Proliferating bipotential glial progenitor cells in adult rat optic nerve. *Nature* **319**, 499–502 (1986).
20. Dimou, L., Simon, C., Kirchhoff, F., Takebayashi, H. & Götz, M. Progeny of Olig2-Expressing Progenitors in the Gray and White Matter of the Adult Mouse Cerebral Cortex. *The Journal of Neuroscience* **28**, 10434–10442 (2008).
21. Rivers, L. E. *et al.* PDGFRA/NG2 glia generate myelinating oligodendrocytes and piriform projection neurons in adult mice. *Nature Neuroscience* **11**, 1392–1401 (2008).
22. Psachoulia, K., Jamen, F., Young, K. M. & Richardson, W. D. Cell cycle dynamics of NG2 cells in the postnatal and ageing brain. *Neuron Glia Biology* **5**, 57–67 (2009).
23. Simon, C., Götz, M. & Dimou, L. Progenitors in the adult cerebral cortex: Cell cycle properties and regulation by physiological stimuli and injury. *Glia* **59**, 869–881 (2011).
24. Hughes, E. G., Kang, S. H., Fukaya, M. & Bergles, D. E. Oligodendrocyte progenitors balance growth with self-repulsion to achieve homeostasis in the adult brain. *Nature Neuroscience* **16**, 668–676 (2013).
25. Bergles, D. E., Roberts, J. D. B., Somogyi, P. & Jahr, C. E. Glutamatergic synapses on oligodendrocyte precursor cells in the hippocampus. *Nature* **405**, 187–191 (2000).

26. Sun, W & Dietrich, D. Synaptic integration by NG2 cells. *Frontiers in Cellular Neuroscience* **7**, 1–13 (2013).
27. De Biase, L. M., Nishiyama, A. & Bergles, D. E. Excitability and Synaptic Communication within the Oligodendrocyte Lineage. *The Journal of Neuroscience* **30**, 3600–3611 (2010).
28. Herculano-Houzel, S. The glia/neuron ratio: How it varies uniformly across brain structures and species and what that means for brain physiology and evolution. *Glia* **62**, 1377–1391 (2014).
29. Batiuk, M. Y. *et al.* Identification of region-specific astrocyte subtypes at single cell resolution. *Nature Communications* **11**, 1220 (2020).
30. Lundgaard, I, Osório, M. J., Kress, B. T., Sanggaard, S & Nedergaard, M. White matter astrocytes in health and disease. *Neuroscience* **276**, 161–173 (2014).
31. Bushong, E. A., Martone, M. E., Jones, Y. Z. & Ellisman, M. H. Protoplasmic Astrocytes in CA1 Stratum Radiatum Occupy Separate Anatomical Domains. *Journal of Neuroscience* **22**, 183–192 (2002).
32. Nagelhus, E. A & Ottersen, O. P. Physiological Roles of Aquaporin-4 in Brain. *Physiological Reviews* **93**, 1543–1562 (2013).
33. Verkhratsky, A, Nedergaard, M & Hertz, L. Why are Astrocytes Important? *Neurochemical Research* **40**, 389–401 (2015).
34. Halassa, M. M., Fellin, T. & Haydon, P. G. The tripartite synapse: roles for gliotransmission in health and disease. *Trends in Molecular Medicine* **13**, 54–63 (2007).
35. Sofroniew, M. V. & Vinters, H. V. Astrocytes: biology and pathology. *Acta Neuropathologica* **119**, 7–35 (2010).
36. Abbott, N. J., Rönnbäck, L & Hansson, E. Astrocyte–endothelial interactions at the blood–brain barrier. *Nature Reviews Neuroscience* **7**, 41–53 (2006).
37. Ballabh, P., Braun, A. & Nedergaard, M. The blood–brain barrier: an overview: Structure, regulation, and clinical implications. *Neurobiology of Disease* **16**, 1–13 (2004).
38. Beck, D. W., Vinters, H. V., Hart, M. N. & Cancilla, P. A. Glial Cells Influence Polarity of the Blood-Brain Barrier. *Journal of Neuropathology & Experimental Neurology* **43**, 219–224 (1984).
39. Savidge, T. C. *et al.* Enteric Glia Regulate Intestinal Barrier Function and Inflammation Via Release of S-Nitrosoglutathione. *Gastroenterology* **132**, 1344–1358 (2007).
40. Weidenfeller, C., Svendsen, C. N. & Shusta, E. V. Differentiating embryonic neural progenitor cells induce blood–brain barrier properties. *Journal of Neurochemistry* **101**, 555–565 (2007).

41. Araya, R. *et al.* BMP signaling through BMPRIA in astrocytes is essential for proper cerebral angiogenesis and formation of the blood–brain-barrier. *Molecular and Cellular Neuroscience* **38**, 417–430 (2008).
42. Gordon, G. R. J., Mulligan, S. J. & MacVicar, B. A. Astrocyte control of the cerebrovasculature. *Glia* **55**, 1214–1221 (2007).
43. Iadecola, C. & Nedergaard, M. Glial regulation of the cerebral microvasculature. *Nature Neuroscience* **10**, 1369–1376 (2007).
44. Koehler, R. C., Roman, R. J. & Harder, D. R. Astrocytes and the regulation of cerebral blood flow. *Trends in Neurosciences* **32**, 160–169 (2009).
45. McVicar, B. A. & Newman, E. A. Astrocyte Regulation of Blood Flow in the Brain. *Cold Spring Harbor Perspectives in Biology* **7** (2015).
46. Schummers, J., Yu, H & Sur, M. Tuned Responses of Astrocytes and Their Influence on Hemodynamic Signals in the Visual Cortex. *Science* **320**, 1638–1643 (2008).
47. Wolf, F. & Kirchhoff, F. Imaging Astrocyte Activity. *Science* **320**, 1597–1599 (2008).
48. Phelps, C. H. Barbiturate-induced glycogen accumulation in brain. An electron microscopic study. *Brain Research* **39**, 225–234 (1972).
49. Peters A Palay SL, W. H. The fine structure of the nervous system. *Third edn.* Oxford University Press, NewYork (1991).
50. Brown, A. M. & Ransom, B. R. Astrocyte glycogen and brain energy metabolism. *Glia* **55**, 1263–1271 (2007).
51. Suh, S. W. *et al.* Astrocyte Glycogen Sustains Neuronal Activity during Hypoglycemia: Studies with the Glycogen Phosphorylase Inhibitor CP-316,819 ([R-R*,S*]-5-Chloro-N-[2-hydroxy-3-(methoxymethylamino)-3-oxo-1-(phenylmethyl)propyl]-1H-indole-2-carboxamide). *Journal of Pharmacology and Experimental Therapeutics* **321**, 45–50 (2007).
52. Araque, A. *et al.* Gliotransmitters Travel in Time and Space. *Neuron* **81**, 728–739 (2014).
53. Kofuji, P. & Araque, A. Astrocytes and Behavior. *Annu Rev Neurosci* (2021).
54. Durkee, C. A. *et al.* $G_{i/o}$ protein-coupled receptors inhibit neurons but activate astrocytes and stimulate gliotransmission. *Glia* **67**, 1076–1093 (2019).
55. Lines, J, Martin, E. D., Kofuji, P, Aguilar, J & Araque, A. Astrocytes modulate sensory-evoked neuronal network activity. *Nat. Commun.* **11**, 3689 (2020).
56. Perez-Alvarez, A, Navarrete, M, Covelo, A, Martin, E. D. & Araque, A. Structural and Functional Plasticity of Astrocyte Processes and Dendritic Spine Interactions. *The Journal of Neuroscience* **34**, 12738–12744 (2014).

57. Shigetomi, E. *et al.* Imaging calcium microdomains within entire astrocyte territories and endfeet with GCaMPs expressed using adeno-associated viruses. *J. Gen. Physiol.* **141**, 633–647 (2013).
58. Stobart, J. L. *et al.* Cortical Circuit Activity Evokes Rapid Astrocyte Calcium Signals on a Similar Timescale to Neurons. *Neuron* **98**, 726–735.e4 (2018).
59. Mariotti, L. *et al.* Interneuron-specific signaling evokes distinctive somatostatin-mediated responses in adult cortical astrocytes. *Nat Commun* **9**, 82 (2018).
60. Araque, A., Parpura, V., Sanzgiri, R. P. & Haydon, P. G. Tripartite synapses: glia, the unacknowledged partner. *Trends in Neurosciences* **22**, 208–215 (1999).
61. Perea, G., Navarrete, M. & Araque, A. Tripartite synapses: astrocytes process and control synaptic information. *Trends in Neurosciences* **32**, 421–431 (2009).
62. De Pittà, M., Brunel, N. & Volterra, A. Astrocytes: Orchestrating synaptic plasticity? *Neuroscience* **323**, 43–61 (2016).
63. Khakh, B. S. & Deneen, B. The Emerging Nature of Astrocyte Diversity. *Annual Review of Neuroscience* **42**, 187–207 (2019).
64. Sibille, J., Pannasch, U. & Rouach, N. Astroglial potassium clearance contributes to short-term plasticity of synaptically evoked currents at the tripartite synapse. *The Journal of Physiology* **592**, 87–102 (2014).
65. Nwaobi, S. E., Cuddapah, V. A., Patterson, K. C., Randolph, A. C. & Olsen, M. L. The role of glial-specific Kir4.1 in normal and pathological states of the CNS. *Acta Neuropathologica* **132**, 1–21 (2016).
66. Nielsen, S. *et al.* Specialized Membrane Domains for Water Transport in Glial Cells: High-Resolution Immunogold Cytochemistry of Aquaporin-4 in Rat Brain. *The Journal of Neuroscience* **17**, 171–180 (1997).
67. Risher, W. C., Andrew, R. D. & Kirov, S. A. Real-time passive volume responses of astrocytes to acute osmotic and ischemic stress in cortical slices and in vivo revealed by two-photon microscopy. *Glia* **57**, 207–221 (2009).
68. Danbolt, N. C. Glutamate uptake. *Progress in Neurobiology* **65**, 1–105 (2001).
69. Herman, M. A. & Jahr, C. E. Extracellular Glutamate Concentration in Hippocampal Slice. *The Journal of Neuroscience* **27**, 9736–9741 (2007).
70. Charles, A. C., Merrill, J. E., Dirksen, E. R. & Sanderson, M. J. Intercellular signaling in glial cells: calcium waves and oscillations in response to mechanical stimulation and glutamate. *Neuron* **6**, 983–992 (1991).
71. Smith, S. J. in *Neuronal-Astrocytic Interactions* (eds Yu, A. C., Hertz, L., Norenberg, M. D., Syková, E. & Waxman, S. G.) 119–136 (Elsevier, 1992).
72. Smith, S. J. Neural Signalling: Neuromodulatory astrocytes. *Current Biology* **4**, 807–810 (1994).

73. Fiacco, T. A., Agulhon, C. & McCarthy, K. D. Sorting Out Astrocyte Physiology from Pharmacology. *Annual Review of Pharmacology and Toxicology* **49**, 151–174 (2009).
74. Khakh, B. S. & McCarthy, K. D. Astrocyte Calcium Signaling: From Observations to Functions and the Challenges Therein. *Cold Spring Harbor Perspectives in Biology* **7**, a020404 (2015).
75. Volterra, A., Liaudet, N. & Savtchouk, I. Astrocyte Ca(2)(+) signalling: an unexpected complexity. *Nat Rev Neurosci* **15**, 327–335 (2014).
76. Bazargani, N. & Attwell, D. Astrocyte calcium signaling: the third wave. *Nat Neurosci* **19**, 182–9 (2016).
77. Shigetomi, E., Patel, S. & Khakh, B. S. Probing the Complexities of Astrocyte Calcium Signaling. *Trends in Cell Biology* **26**, 300–312 (2016).
78. Paredes, R. M., Etzler, J. C., Watts, L. T., Zheng, W. & Lechleiter, J. D. Chemical calcium indicators. *Methods* **46**, 143–151 (2008).
79. Chen, T. W. *et al.* Ultrasensitive fluorescent proteins for imaging neuronal activity. *Nature* **499**, 295–300 (2013).
80. Denk, W. *et al.* Anatomical and functional imaging of neurons using 2-photon laser scanning microscopy. *Journal of Neuroscience Methods* **54**. Imaging Techniques in Neurobiology, 151–162 (1994).
81. Helmchen, F. & Denk, W. Deep tissue two-photon microscopy. *Nature Methods* **2**, 932–940 (2005).
82. Svoboda, K. & Yasuda, R. Principles of Two-Photon Excitation Microscopy and Its Applications to Neuroscience. *Neuron* **50**, 823–839 (2006).
83. Zipfel, W. R., Williams, R. M. & Webb, W. W. Nonlinear magic: multiphoton microscopy in the biosciences. *Nature Biotechnology* **21**, 1369–1377 (2003).
84. Yang, W. & Yuste, R. In vivo imaging of neural activity. *Nature Methods* **14**, 349–359 (2017).
85. Hausteiner, M. D. *et al.* Conditions and Constraints for Astrocyte Calcium Signaling in the Hippocampal Mossy Fiber Pathway. *Neuron* **82**, 413–429 (2014).
86. Paukert, M. *et al.* Norepinephrine Controls Astroglial Responsiveness to Local Circuit Activity. *Neuron* **82**, 1263–1270 (2014).
87. Shigetomi, E., Kracun, S., Sofroniew, M. V. & Khakh, B. S. A genetically targeted optical sensor to monitor calcium signals in astrocyte processes. *Nature Neuroscience* **13**, 759–766 (2010).
88. Shigetomi, E., Tong, X., Kwan, K. Y., Corey, D. P. & Khakh, B. S. TRPA1 channels regulate astrocyte resting calcium and inhibitory synapse efficacy through GAT-3. *Nature Neuroscience* **15**, 70–80 (2012).

89. Stobart, J. L. *et al.* Long-term In Vivo Calcium Imaging of Astrocytes Reveals Distinct Cellular Compartment Responses to Sensory Stimulation. *Cerebral Cortex* **28**, 184–198 (2018).
90. Jiang, R., Diaz-Castro, B., Looger, L. L. & Khakh, B. S. Dysfunctional Calcium and Glutamate Signaling in Striatal Astrocytes from Huntington's Disease Model Mice. *The Journal of Neuroscience* **36**, 3453–3470 (2016).
91. Perea, G. & Araque, A. Properties of Synaptically Evoked Astrocyte Calcium Signal Reveal Synaptic Information Processing by Astrocytes. *Journal of Neuroscience* **25**, 2192–2203 (2005).
92. Di Castro, M. A. *et al.* Local Ca²⁺ detection and modulation of synaptic release by astrocytes. *Nature Neuroscience* **14**, 1276 (2011).
93. Panatier, A. *et al.* Astrocytes Are Endogenous Regulators of Basal Transmission at Central Synapses. *Cell* **146**, 785–798 (2011).
94. Straub, S. V., Bonev, A. D., Wilkerson, M. K. & Nelson, M. T. Dynamic Inositol Trisphosphate-mediated Calcium Signals within Astrocytic Endfeet Underlie Vasodilation of Cerebral Arterioles. *Journal of General Physiology* **128**, 659–669 (2006).
95. Dunn, K. M., Hill-Eubanks, D. C., Liedtke, W. B. & Nelson, M. T. TRPV4 channels stimulate Ca²⁺-induced Ca²⁺-release in astrocytic endfeet and amplify neurovascular coupling responses. *Proceedings of the National Academy of Sciences* **110**, 6157–6162 (2013).
96. Ding, F. *et al.* α 1-Adrenergic receptors mediate coordinated Ca²⁺ signaling of cortical astrocytes in awake, behaving mice. *Cell Calcium* **54**, 387–394 (2013).
97. Nimmerjahn, A., Mukamel, E. A. & Schnitzer, M. J. Motor Behavior Activates Bergmann Glial Networks. *Neuron* **62**, 400–412 (2009).
98. Srinivasan, R. *et al.* Ca(2+) signaling in astrocytes from Ip3r2(-/-) mice in brain slices and during startle responses in vivo. *Nat Neurosci* **18**, 708–17 (2015).
99. Mehina, E. M. F., Murphy-Royal, C. & Gordon, G. R. Steady-State Free Ca²⁺ in Astrocytes Is Decreased by Experience and Impacts Arteriole Tone. *The Journal of Neuroscience* **37**, 8150–8165 (2017).
100. Rosenegger, D., Tran, C. H. T., Wamsteeker Cusulin, J. I. & Gordon, G. R. Tonic Local Brain Blood Flow Control by Astrocytes Independent of Phasic Neurovascular Coupling. *The Journal of Neuroscience* **35**, 13463–13474 (2015).
101. Zheng, K. *et al.* Time-Resolved Imaging Reveals Heterogeneous Landscapes of Nanomolar Ca²⁺ in Neurons and Astroglia. *Neuron* **88**, 277–288 (2015).
102. Chen, N. *et al.* Nucleus basalis-enabled stimulus-specific plasticity in the visual cortex is mediated by astrocytes. *Proceedings of the National Academy of Sciences* **109**, E2832–E2841 (2012).

103. Perea, G., Yang, A., Boyden, E. S. & Sur, M. Optogenetic astrocyte activation modulates response selectivity of visual cortex neurons in vivo. *Nature Communications* **5**, 3262 (2014).
104. Nagai, J. *et al.* Hyperactivity with Disrupted Attention by Activation of an Astrocyte Synaptogenic Cue. *Cell* **177**, 1280–1292.e20 (2019).
105. Padmashri, R., Suresh, A., Boska, M. D. & Dunaevsky, A. Motor-Skill Learning Is Dependent on Astrocytic Activity. *Neural Plasticity* **2015**, 938023 (2015).
106. Mu, Y *et al.* Glia Accumulate Evidence that Actions Are Futile and Suppress Unsuccessful Behavior. *Cell* **178**, 27–43.e19 (2019).
107. Deemyad, T., Lüthi, J. & Spruston, N. Astrocytes integrate and drive action potential firing in inhibitory subnetworks. *Nature Communications* **9**, 4336 (2018).
108. Yu, X, Nagai, J & Khakh, B. S. Improved tools to study astrocytes. *Nat. Rev. Neurosci.* **21**, 121–138 (2020).
109. Wang, X. *et al.* Astrocytic Ca²⁺ signaling evoked by sensory stimulation in vivo. *Nat Neurosci* **9**, 816–823 (2006).
110. Merten, K., Folk, R. W., Duarte, D. & Nimmerjahn, A. Astrocytes encode complex behaviorally relevant information. *bioRxiv 2021.10.09.463784* (2021).
111. Curreli, S., Bonato, J., Romanzi, S., Panzeri, S. & Fellin, T. Complementary encoding of spatial information in hippocampal astrocytes. *PLOS Biol.* **20**, e3001530 (2022).
112. Doron, A. *et al.* Hippocampal astrocytes encode reward location. *Nature* **609**, 772–778 (2022).
113. Shannon, C. E. A mathematical theory of communication. *Bell Syst. Tech. J.* **27**, 379–423 (1948).
114. Quiroga, R. Q. & Panzeri, S. Extracting information from neuronal populations: information theory and decoding approaches. *Nat. Rev. Neurosci.* **10**, 173–185 (2009).
115. Bonato, J., Curreli, S., Fellin, T. & Panzeri, S. Optimizing Measures of Information Encoding in Astrocytic Calcium Signals. *Brain Informatics. BI 2022. Lecture Notes in Computer Science (Springer International Publishing)* **13406**, 117–128 (2022).
116. Ronneberger, O., Fischer, P. & Brox, T. *U-Net: Convolutional Networks for Biomedical Image Segmentation in Medical Image Computing and Computer-Assisted Intervention – MICCAI 2015* (Springer International Publishing, 2015), 234–241.
117. Agarwal, A. *et al.* Transient Opening of the Mitochondrial Permeability Transition Pore Induces Microdomain Calcium Transients in Astrocyte Processes. *Neuron* **93**, 587–605 e7 (2017).

118. Bindocci, E. *et al.* Three-dimensional Ca(2+) imaging advances understanding of astrocyte biology. *Science* **356** (2017).
119. Hirase, H., Qian, L., Bartho, P. & Buzsaki, G. Calcium dynamics of cortical astrocytic networks in vivo. *PLoS Biol* **2**, E96 (2004).
120. Dayan, P. & Abbott, L. F. *Theoretical neuroscience: computational and mathematical modeling of neural systems* (Mass: MIT Press, Cambridge, 2011).
121. Panzeri, S., Macke, J. H., Gross, J. & Kayser, C. Neural population coding: combining insights from microscopic and mass signals. *Trends Cogn Sci* **19**, 162–172 (2015).
122. O’Keefe, J & Dostrovsky, J. The hippocampus as a spatial map. Preliminary evidence from unit activity in the freely-moving rat. *Brain Res.* **34**, 171–175 (1971).
123. Harvey, C. D., Collman, F., Dombeck, D. A. & Tank, D. W. Intracellular dynamics of hippocampal place cells during virtual navigation. *Nature* **461**, 941–6 (2009).
124. Dombeck, D. A., Harvey, C. D., Tian, L, Looger, L. L. & Tank, D. W. Functional imaging of hippocampal place cells at cellular resolution during virtual navigation. *Nat. Neurosci.* **13**, 1433–1440 (2010).
125. Gu, L. *et al.* Long-term in vivo imaging of dendritic spines in the hippocampus reveals structural plasticity. *J Neurosci* **34**, 13948–53 (2014).
126. Attardo, A., Fitzgerald, J. E. & Schnitzer, M. J. Impermanence of dendritic spines in live adult CA1 hippocampus. *Nature* **523**, 592–596 (2015).
127. Saleem, A. B., Diamanti, E. M., Fournier, J., Harris, K. D. & Carandini, M. Coherent encoding of subjective spatial position in visual cortex and hippocampus. *Nature* **562**, 124–127 (2018).
128. Sheffield, M. E. & Dombeck, D. A. Calcium transient prevalence across the dendritic arbour predicts place field properties. *Nature* **517**, 200–4 (2015).
129. Dombeck, D. A., Khabbaz, A. N., Collman, F., Adelman, T. L. & Tank, D. W. Imaging large-scale neural activity with cellular resolution in awake, mobile mice. *Neuron* **56**, 43–57 (2007).
130. Runyan, C. A., Piasini, E., Panzeri, S. & Harvey, C. D. Distinct timescales of population coding across cortex. *Nature* **548**, 92–96 (2017).
131. Stefanini, F. *et al.* A Distributed Neural Code in the Dentate Gyrus and in CA1. *Neuron* **107**, 703–716 e4 (2020).
132. Pola, G., Thiele, A., Hoffmann, K. P. & Panzeri, S. An exact method to quantify the information transmitted by different mechanisms of correlational coding. *Network* **14**, 35–60 (2003).

133. Magri, C., Whittingstall, K., Singh, V., Logothetis, N. K. & Panzeri, S. A toolbox for the fast information analysis of multiple-site LFP, EEG and spike train recordings. *BMC Neurosci* **10**, 81 (2009).
134. Haydon, P. G. GLIA: listening and talking to the synapse. *Nat Rev Neurosci* **2**, 185–193 (2001).
135. Bowser, D. N. & Khakh, B. S. ATP excites interneurons and astrocytes to increase synaptic inhibition in neuronal networks. *J Neurosci* **24**, 8606–8620 (2004).
136. Bergles, D. E. & Jahr, C. E. Synaptic activation of glutamate transporters in hippocampal astrocytes. *Neuron* **19**, 1297–1308 (1997).
137. Mishima, T. & Hirase, H. In vivo intracellular recording suggests that gray matter astrocytes in mature cerebral cortex and hippocampus are electrophysiologically homogeneous. *J Neurosci* **30**, 3093–3100 (2010).
138. Carmignoto, G., Pasti, L. & Pozzan, T. On the role of voltage-dependent calcium channels in calcium signaling of astrocytes in situ. *J Neurosci* **18**, 4637–4645 (1998).
139. Santello, M. & Volterra, A. Synaptic modulation by astrocytes via Ca²⁺-dependent glutamate release. *Neuroscience* **158**, 253–259 (2009).
140. Panzeri, S., Harvey, C. D., Piasini, E., Latham, P. E. & Fellin, T. Cracking the Neural Code for Sensory Perception by Combining Statistics, Intervention, and Behavior. *Neuron* **93**, 491–507 (2017).
141. Forli, A. *et al.* Two-Photon Bidirectional Control and Imaging of Neuronal Excitability with High Spatial Resolution In Vivo. *Cell Rep* **22**, 3087–3098 (2018).
142. Robinson, N. T. M. *et al.* Targeted Activation of Hippocampal Place Cells Drives Memory-Guided Spatial Behavior. *Cell* **183**, 1586–1599 e10 (2020).
143. Forli, A., Pisoni, M., Printz, Y., Yizhar, O. & Fellin, T. Optogenetic strategies for high-efficiency all-optical interrogation using blue-light-sensitive opsins. *Elife* **10** (2021).
144. Hartley, T., Lever, C., Burgess, N. & O’Keefe, J. Space in the brain: how the hippocampal formation supports spatial cognition. *Philos Trans R Soc Lond B Biol Sci* **369**, 20120510 (2014).
145. Moser, M.-B., Rowland, D. C. & Moser, E. I. Place cells, grid cells, and memory. *Cold Spring Harbor perspectives in biology* **7**, a021808 (2015).
146. Moser, E. I., Moser, M. B. & McNaughton, B. L. Spatial representation in the hippocampal formation: a history. *Nat Neurosci* **20**, 1448–1464 (2017).
147. Bellmund, J. L. S., Gardenfors, P., Moser, E. I. & Doeller, C. F. Navigating cognition: Spatial codes for human thinking. *Science* **362** (2018).

148. Papouin, T., Dunphy, J., Tolman, M., Foley, J. C. & Haydon, P. G. Astrocytic control of synaptic function. *Philos Trans R Soc Lond B Biol Sci* **372** (2017).
149. Nagai, J. *et al.* Behaviorally consequential astrocytic regulation of neural circuits. *Neuron* **109**, 576–596 (2021).
150. Salinas, E. & Thier, P. Gain modulation: a major computational principle of the central nervous system. *Neuron* **27**, 15–21 (2000).
151. Swinehart, C. D. & Abbott, L. F. Supervised learning through neuronal response modulation. *Neural Comput* **17**, 609–631 (2005).
152. Salinas, E. & Abbott, L. F. Transfer of coded information from sensory to motor networks. *J Neurosci* **15**, 6461–6474 (1995).
153. Stroud, J. P., Porter, M. A., Hennequin, G. & Vogels, T. P. Motor primitives in space and time via targeted gain modulation in cortical networks. *Nat Neurosci* **21**, 1774–1783 (2018).
154. Guizar-Sicairos, M., Thurman, S. T. & Fienup, J. R. Efficient subpixel image registration algorithms. *Optics letters* **33**, 156–158 (2008).
155. Van der Walt, S. *et al.* scikit-image: image processing in Python. *PeerJ* **2**, e453 (2014).
156. Brondi, M. *et al.* High-Accuracy Detection of Neuronal Ensemble Activity in Two-Photon Functional Microscopy Using Smart Line Scanning. *Cell Rep* **30**, 2567–2580 e6 (2020).
157. Optican, L. M., Gawne, T. J., Richmond, B. J. & Joseph, P. J. Unbiased measures of transmitted information and channel capacity from multivariate neuronal data. *Biol Cybern* **65**, 305–310 (1991).
158. Panzeri, S & Treves, A. Analytical estimates of limited sampling biases in different information measures. *Network: Computation in Neural Systems* **7**, 87–107 (1996).
159. Quenouille, M. H. Notes on bias in estimation. *Biometrika* **43**, 353–360 (1956).
160. Tukey, J. Bias and confidence in not quite large samples. *Ann. Math. Statist.* **29**, 614 (1958).
161. Strong, S. P., Koberle, R, de Ruyter van Steveninck, R. R. & Bialek, W. Entropy and Information in Neural Spike Trains. *Phys. Rev. Lett.* **80**, 197–200 (1998).
162. Panzeri, S, Senatore, R, Montemurro, M. A. & Petersen, R. S. Correcting for the Sampling Bias Problem in Spike Train Information Measures. *J. Neurophysiol.* **98**, 1064–1072 (2007).
163. Virtanen, P. *et al.* SciPy 1.0: fundamental algorithms for scientific computing in Python. *Nature methods* **17**, 261–272 (2020).
164. Van Rossum, G. & Drake, F. L. *Python 3 Reference Manual* (CreateSpace, 2009).

165. Calin-Jageman, R. J. & Cumming, G. Estimation for Better Inference in Neuroscience. *eNeuro* **6** (2019).
166. Thalhammer, A. *et al.* Alternative Splicing of P/Q-Type Ca(2+) Channels Shapes Presynaptic Plasticity. *Cell Rep* **20**, 333–343 (2017).
167. Vecchia, D. *et al.* Temporal Sharpening of Sensory Responses by Layer V in the Mouse Primary Somatosensory Cortex. *Curr Biol* **30**, 1589–1599 e10 (2020).
168. Zack, G. W., Rogers, W. E. & Latt, S. A. Automatic measurement of sister chromatid exchange frequency. *J Histochem Cytochem* **25**, 741–753 (1977).
169. Schneider, C. A., Rasband, W. S. & Eliceiri, K. W. NIH Image to ImageJ: 25 years of image analysis. *Nat Methods* **9**, 671–675 (2012).
170. Ince, R. A. A., Mazzoni, A., Bartels, A., Logothetis, N. K. & Panzeri, S. A novel test to determine the significance of neural selectivity to single and multiple potentially correlated stimulus features. *J. Neurosci. Meth.* **210**, 49–65 (2012).
171. Nemenman, I., Shafee, F. & Bialek, W. *Entropy and Inference in Revisited Advances in Neural Information Processing Systems*, edited by: Dietterich T. G. and Becker S. and Ghahramani Z. **14** (Cambridge, MA: MIT Press, 2002), 95–100.
172. Nemenman, I, Bialek, W & de Ruyter van Steveninck, R. Entropy and information in neural spike trains: progress on the sampling problem. *Phys. Rev. E* **69**, 056111 (2004).
173. Paninski, L. Estimation of Entropy and Mutual Information. *Neural Comput.* **15**, 1191–1253 (2003).
174. Adamsky, A. *et al.* Astrocytic Activation Generates De Novo Neuronal Potentiation and Memory Enhancement. *Cell* **174**, 59–71.e14 (2018).
175. Slezak, M. *et al.* Distinct Mechanisms for Visual and Motor-Related Astrocyte Responses in Mouse Visual Cortex. *Current Biology*, 3120–3127.e5.
176. Wang, Y. *et al.* Accurate quantification of astrocyte and neurotransmitter fluorescence dynamics for single-cell and population-level physiology. *Nature Neuroscience* **22**, 1936–1944 (2019).
177. Mukamel, E. A., Nimmerjahn, A. & Schnitzer, M. J. Automated Analysis of Cellular Signals from Large-Scale Calcium Imaging Data. *Neuron* **63**, 747–760 (2009).
178. Pnevmatikakis, E. A. *et al.* Simultaneous Denoising, Deconvolution, and Demixing of Calcium Imaging Data. *Neuron* **89**, 285–299 (2016).
179. Pachitariu, M. *et al.* Suite2p: beyond 10,000 neurons with standard two-photon microscopy. *bioRxiv* (2017).

180. Klibisz, A., Rose, D., Eicholtz, M., Blundon, J. & Zakharenko, S. *Fast, Simple Calcium Imaging Segmentation with Fully Convolutional Networks in Deep Learning in Medical Image Analysis and Multimodal Learning for Clinical Decision Support* (Springer International Publishing, 2017), 285–293.
181. Giovannucci, A. *et al.* CaImAn an open source tool for scalable calcium imaging data analysis. *eLife* **8**, e38173 (2019).
182. Soltanian-Zadeh, S., Sahingur, K., Blau, S., Gong, Y. & Farsiu, S. Fast and robust active neuron segmentation in two-photon calcium imaging using spatiotemporal deep learning. *Proceedings of the National Academy of Sciences* **116**, 8554–8563 (2019).
183. Donahue, J. *et al.* DeCAF: A Deep Convolutional Activation Feature for Generic Visual Recognition in *Proceedings of the 31st International Conference on International Conference on Machine Learning - Volume 32* (JMLR.org, 2014), I–647–I–655.
184. Yosinski, J., Clune, J., Bengio, Y. & Lipson, H. in *Advances in Neural Information Processing Systems 27* 3320–3328 (Curran Associates, Inc., 2014).
185. Mathis, A. *et al.* DeepLabCut: markerless pose estimation of user-defined body parts with deep learning. *Nature Neuroscience* **21**, 1281–1289 (2018).
186. Deng, L. The mnist database of handwritten digit images for machine learning research. *IEEE Signal Processing Magazine* **29**, 141–142 (2012).
187. Szegedy, C., Ioffe, S., Vanhoucke, V. & Alemi, A. A. *Inception-v4, inception-ResNet and the Impact of Residual Connections on Learning in Proceedings of the Thirty-First AAAI Conference on Artificial Intelligence* (AAAI Press, 2017), 4278–4284.
188. He, K., Zhang, X., Ren, S. & Sun, J. Deep residual learning for image recognition. *Proceedings of the IEEE Computer Society Conference on Computer Vision and Pattern Recognition*, 770–778 (2016).
189. Zhou, Z., Siddiquee, M. M. R., Tajbakhsh, N. & Liang, J. UNet++: Redesigning Skip Connections to Exploit Multiscale Features in Image Segmentation. *IEEE Transactions on Medical Imaging* **39**, 1856–1867 (2020).
190. Wang, P. *et al.* Understanding Convolution for Semantic Segmentation. *2018 IEEE Winter Conference on Applications of Computer Vision (WACV)*, 1451–1460 (2018).
191. Perez, L. & Wang, J. The Effectiveness of Data Augmentation in Image Classification using Deep Learning. *arXiv* (2017).
192. Milletari, F., Navab, N. & Ahmadi, S.-A. V-Net: Fully Convolutional Neural Networks for Volumetric Medical Image Segmentation. *2016 Fourth International Conference on 3D Vision (3DV)*, 565–571 (2016).

193. Kingma, D. P. & Ba, J. *Adam: A Method for Stochastic Optimization* in *3rd International Conference on Learning Representations, ICLR 2015, San Diego, CA, USA, May 7-9, 2015, Conference Track Proceedings* (2015).
194. Kuhn, H. W. The Hungarian Method for the Assignment Problem. *Naval Research Logistics Quarterly* **2**, 83–97 (1955).
195. Schindelin, J. *et al.* Fiji: an open-source platform for biological-image analysis. *Nature Methods* **9**, 676 (2012).
196. Paszke, A. *et al.* in *Advances in Neural Information Processing Systems 32* 8024–8035 (2019).
197. Merkel, D. Docker: lightweight linux containers for consistent development and deployment. *Linux journal* **2014**, 2 (2014).
198. Bradski, G. The OpenCV Library. *Dr. Dobb's Journal of Software Tools* (2000).
199. Pedregosa, F. *et al.* Scikit-learn: Machine learning in Python. *the Journal of machine Learning research* **12**, 2825–2830 (2011).
200. Jones, E., Oliphant, T., Peterson, P. & Others. *SciPy: Open Source Scientific Tools for Python, 2001* (<http://www.scipy.org/>) 2015.
201. Holm, S. A Simple Sequentially Rejective Multiple Test Procedure. *Scandinavian Journal of Statistics* **6**, 65–70 (1979).
202. Gauthier, J. L. & Tank, D. W. A Dedicated Population for Reward Coding in the Hippocampus. *Neuron* **99**, 179–193 e7 (2018).
203. McNaughton, B. L., Barnes, C. A. & O'Keefe, J. The contributions of position, direction, and velocity to single unit activity in the hippocampus of freely-moving rats. *Exp Brain Res* **52**, 41–9 (1983).
204. Gois, Z. & Tort, A. B. L. Characterizing Speed Cells in the Rat Hippocampus. *Cell Rep* **25**, 1872–1884 e4 (2018).
205. Kol, A. *et al.* Astrocytes contribute to remote memory formation by modulating hippocampal–cortical communication during learning. *Nature Neuroscience* **23**, 1229–1239 (2020).
206. Muller, R. U., Kubie, J. L., Bostock, E. M., Taube, J. S. & Quirk, G. J. in *Brain and space*. 296–333 (Oxford University Press, 1991).
207. Colgin, L. L., Moser, E. I. & Moser, M.-B. Understanding memory through hippocampal remapping. *Trends in Neurosciences* **31**, 469–477 (2008).
208. Bostock, E., Muller, R. U. & Kubie, J. L. Experience-dependent modifications of hippocampal place cell firing. *Hippocampus* **1**, 193–205 (1991).
209. Cohen, J. D., Bolstad, M. & Lee, A. K. Experience-dependent shaping of hippocampal CA1 intracellular activity in novel and familiar environments. *eLife* **6**, e23040 (2017).

210. Fyhn, M., Hafting, T., Treves, A., Moser, M.-B. & Moser, E. I. Hippocampal remapping and grid realignment in entorhinal cortex. *Nature* **446**, 190–194 (2007).
211. Leutgeb, S., Leutgeb, J. K., Treves, A., Moser, M.-B. & Moser, E. I. Distinct Ensemble Codes in Hippocampal Areas CA3 and CA1. *Science* **305**, 1295–1298 (2004).
212. Leutgeb, S. *et al.* Independent Codes for Spatial and Episodic Memory in Hippocampal Neuronal Ensembles. *Science* **309**, 619–623 (2005).
213. Sheffield, M. E., Adoff, M. D. & Dombeck, D. A. Increased Prevalence of Calcium Transients across the Dendritic Arbor during Place Field Formation. *Neuron* **96**, 490–504.e5 (2017).
214. Muller, R. & Kubie, J. The effects of changes in the environment on the spatial firing of hippocampal complex-spike cells. *Journal of Neuroscience* **7**, 1951–1968 (1987).
215. Quirk, G., Muller, R. & Kubie, J. The firing of hippocampal place cells in the dark depends on the rat's recent experience. *Journal of Neuroscience* **10**, 2008–2017 (1990).
216. Wills, T. J., Lever, C., Cacucci, F., Burgess, N. & O'Keefe, J. Attractor Dynamics in the Hippocampal Representation of the Local Environment. *Science* **308**, 873–876 (2005).
217. Radvansky, B. A., Oh, J. Y., Climer, J. R. & Dombeck, D. A. Behavior determines the hippocampal spatial mapping of a multisensory environment. *Cell Reports* **36** (2021).
218. Markus, E. *et al.* Interactions between location and task affect the spatial and directional firing of hippocampal neurons. *Journal of Neuroscience* **15**, 7079–7094 (1995).
219. Sheffield, M. E. & Dombeck, D. A. Dendritic mechanisms of hippocampal place field formation. *Current Opinion in Neurobiology* **54**. Neurobiology of Learning and Plasticity, 1–11 (2019).
220. Frank, L. M., Stanley, G. B. & Brown, E. N. Hippocampal Plasticity across Multiple Days of Exposure to Novel Environments. *Journal of Neuroscience* **24**, 7681–7689 (2004).
221. Hill, A. First occurrence of hippocampal spatial firing in a new environment. *Experimental Neurology* **62**, 282–297 (1978).
222. Monaco, J. D., Rao, G., Roth, E. D. & Knierim, J. J. Attentive scanning behavior drives one-trial potentiation of hippocampal place fields. *Nature Neuroscience* **17**, 725–731 (2014).
223. Gawne, T. & Richmond, B. How independent are the messages carried by adjacent inferior temporal cortical neurons? *Journal of Neuroscience* **13**, 2758–2771 (1993).

224. Panzeri, S., Moroni, M., Safaai, H. & Harvey, C. D. The structures and functions of correlations in neural population codes. *Nature Reviews Neuroscience* **23**, 551–567 (2022).
225. Panzeri, S., Schultz, S. R., Treves, A. & Rolls, E. T. Correlations and the encoding of information in the nervous system. *Proceedings of the Royal Society of London. Series B: Biological Sciences* **266**, 1001–1012 (1999).
226. Averbeck, B. B. & Lee, D. Effects of Noise Correlations on Information Encoding and Decoding. *Journal of Neurophysiology* **95**, 3633–3644 (2006).
227. Averbeck, B. B., Latham, P. E. & Pouget, A. Neural correlations, population coding and computation. *Nature Reviews Neuroscience* **7**, 358–366 (2006).
228. Abbott, L. F. & Dayan, P. The Effect of Correlated Variability on the Accuracy of a Population Code. *Neural Computation* **11**, 91–101 (1999).
229. Shamir, M. & Sompolinsky, H. Implications of Neuronal Diversity on Population Coding. *Neural Computation* **18**, 1951–1986 (2006).
230. Azeredo da Silveira, R. & Rieke, F. The Geometry of Information Coding in Correlated Neural Populations. *Annual Review of Neuroscience* **44**, 403–424 (2021).
231. Lin, T.-Y. *et al.* *Microsoft COCO: Common Objects in Context BT - Computer Vision – ECCV 2014* in (eds Fleet, D., Pajdla, T., Schiele, B. & Tuytelaars, T.) (Springer International Publishing, Cham, 2014), 740–755.
232. Liu, Z., Luo, P., Wang, X. & Tang, X. *Deep Learning Face Attributes in the Wild* in *Proceedings of International Conference on Computer Vision (ICCV)* (2015).
233. Russakovsky, O. *et al.* ImageNet Large Scale Visual Recognition Challenge. *International Journal of Computer Vision* **115**, 211–252 (2015).
234. Delgado-Escueta, A. V. The Fine Structure of the Nervous System: Neurons and Their Supporting Cells. Alan Peters , Sanford L. Palay , Henry de F. Webster. *The Quarterly Review of Biology* **67**, 80 (1992).
235. Otsu, Y. *et al.* Calcium dynamics in astrocyte processes during neurovascular coupling. *Nature Neuroscience* **18**, 210–218 (2015).
236. Bishop, C. M. *Pattern recognition and machine learning* (springer, 2006).
237. Cohen, J. *Statistical power analysis for the behavioral sciences* 2nd (Lawrence Erlbaum, Hillsdale, NJ; Hove, 1988).
238. Dana, H. *et al.* Sensitive red protein calcium indicators for imaging neural activity. *Elife* **5** (2016).
239. Ziv, Y. *et al.* Long-term dynamics of CA1 hippocampal place codes. *Nat Neurosci* **16**, 264–266 (2013).
240. Wilson, M. A. & McNaughton, B. L. Dynamics of the Hippocampal Ensemble Code for Space. *Science* **261**, 1055–1058 (1993).

241. Wood, E. R., Dudchenko, P. A. & Eichenbaum, H. The global record of memory in hippocampal neuronal activity. *Nature* **397**, 613–616 (1999).

Appendix A

Chapter 2: Supplementary material

Question	Approach	Results	Controls	Figures
Do astrocytes encode spatial information in their intracellular Ca ²⁺ dynamics?	<ul style="list-style-type: none"> Combination of functional two-photon microscopy and virtual spatial navigation in head-fixed mice. Test spatial information content and spatial tuning properties of CA1 astrocytic Ca²⁺ signals during monodirectional virtual navigation. Test spatial information content and spatial tuning properties of CA1 astrocytic Ca²⁺ signals during bidirectional virtual navigation. 	<ul style="list-style-type: none"> In the mouse hippocampus, astrocytic Ca²⁺ signals encode information about position in space during virtual navigation. Astrocytic spatial response profiles are reliable. Astrocytic spatial response profiles tile the whole virtual corridor. Astrocytic calcium dynamics convey information about position beyond proximal visual cues location. 	<ul style="list-style-type: none"> Quantification of information content is performed across a grid of 77 binning parameter combinations. Non-parametric permutation testing is used to assess statistical significance. Astrocytic spatial responses are robust to resampling approaches. Non-parametric testing is used to assess statistical difference between decoding results before and after disruption of position within single visual cues. 	Fig. 1, 4 Extended data Fig: 2, 5, 10
Is spatial information encoded in astrocytic Ca ²⁺ signals organized at the subcellular level?	<ul style="list-style-type: none"> Classification of astrocytic subcellular ROIs according to their anatomical identity (somata vs. processes) to quantitatively compare spatial tuning properties at the subcellular level. 	<ul style="list-style-type: none"> Astrocytic somata and processes show significant spatial information encoding in their responses. Single astrocytes can have different place fields in distinct topographically organized subcellular locations. 	<ul style="list-style-type: none"> Quantification of information content is performed across a grid of 77 binning parameter combinations. Non-parametric permutation testing is used to assess statistical significance. 	Fig. 2 Extended data Fig: 4, 6
Can spatial information encoded in astrocytic Ca ²⁺ signals be used to decode animals' position?	<ul style="list-style-type: none"> Deployment of a support vector machine (SVM) model to perform classification of animals' position given a set of astrocytic Ca²⁺ signals: <ol style="list-style-type: none"> during monodirectional virtual navigation. during bidirectional virtual navigation. Quantification of the impact of astrocytic Ca²⁺ signal correlations on the decoding of animals' position. 	<ul style="list-style-type: none"> Animals' position is efficiently decoded from astrocytic calcium signals. Disruption of signal correlations of astrocytic population vectors reduce information content. 	<ul style="list-style-type: none"> Decoding analysis is performed across multiple classification granularities. Decoding results are systematically above chance level estimates using non-parametric permutation testing for all granularities. Non-parametric testing is used to assess statistical difference between decoding results before and after disruption of signal correlations. 	Fig. 3 Extended data Fig: 8, 9 Tables: 2, 6
How does astrocytic representation of spatial information relate to that of neuronal cells?	<ul style="list-style-type: none"> Combination of dual color functional two-photon microscopy and virtual spatial navigation in head fixed mice to simultaneously image astrocytic and neuronal activity. Quantitative comparison of astrocytic and neuronal spatial tuning properties during monodirectional virtual navigation. 	<ul style="list-style-type: none"> Astrocytic and neuronal response profiles cover the virtual corridor The majority of spatial information in astrocytes and neurons is genuine spatial information that cannot be explained by tuning to visual cues 	<ul style="list-style-type: none"> Quantification of information content is performed across a grid of 77 binning parameters combinations. Non-parametric permutation testing is used to assess statistical significance. Non-parametric testing is used to assess statistical difference between decoding results before and after disruption of position within single visual cues. 	Fig.5 Extended data Fig: 12, 14, 15, 17, 18. Table: 7, 8, 9
Is the information encoded in astrocytic calcium signals a redundant representation of space-encoding neuronal activity?	<ul style="list-style-type: none"> Pairwise investigation of information encoding comparing astrocytic, neuronal, and mixed ROI pairs. Information Breakdown analysis Deployment of a support vector machine (SVM) model to perform classification of animals' position given different sets of Ca²⁺ signals during monodirectional virtual navigation: <ol style="list-style-type: none"> Using astrocytic signals. Using neuronal signals. 	<ul style="list-style-type: none"> Astrocytic and neuronal responses encode information sharing, a position-dependent correlation component. Astrocytic and neuronal spatial responses provide synergistic and 	<ul style="list-style-type: none"> Decoding analysis is performed across multiple classification granularities. Decoding results are systematically above chance level estimates using non-parametric permutation testing for all granularities. Non-parametric testing is used to assess statistical difference between 	Fig.5 Extended data Fig: 19, 20, 21 Tables: 3, 4, 5, 7, 10

<p>3. Using both astrocytic and neuronal signals.</p> <ul style="list-style-type: none"> Quantification of the impact of Ca^{2+} signal correlations on position decoding. 	<p>complementary spatial information.</p> <ul style="list-style-type: none"> Astrocytes carry information about space that is not available in any of the nearby neurons. 	<p>decoding results before and after disruption of signal correlations.</p>
---	--	---

Table 1. Outline and summary of experiments.

	Permutation type	p G = 4	p G = 8	p G = 12	p G = 16	p G = 20	p G = 24
Decoded	Chance	1E-3	1E-3	1E-3	1E-3	1E-3	1E-3
Information	Trial-shuff.	2E-3	2E-3	2E-3	2E-3	2E-3	2E-3
Decoding Accuracy	Chance	1E-3	1E-3	1E-3	1E-3	1E-3	1E-3
	Trial-shuff.	2E-3	2E-3	2E-3	2E-3	2E-3	2E-3

Table 2. Hypothesis testing: decoding performance about animal’s spatial location from astrocytic calcium signals during monodirectional virtual navigation. p-values for one-tailed non-parametric permutation tests as a function of decoding granularity for decoded information (see Fig. 3B) and decoding accuracy (Extended data Fig. 6). For each imaging session and each granularity, null distributions were obtained with 1000 and 500 iterations to estimate chance level and trial-shuffling, respectively (see Methods). Data from 7 imaging sessions from 3 animals.

Pair type	Comparison	Mean	lower-bound (bits)	Upper-bound (bits)	Cohen's d	p
A-A	I-I _{LIN}	0.0036	0.0023	0.0049	1.847	1E-3
N-N	I-I _{LIN}	0.0029	0.0014	0.0044	1.327	5E-3
A-N	I-I _{LIN}	0.0052	0.0035	0.0069	2.032	1E-3
A-A	I-I _{MAX}	0.0067	0.0039	0.0096	1.579	1E-3
N-N	I-I _{MAX}	0.0182	0.0128	0.0235	2.280	1E-3
A-N	I-I _{MAX}	0.0114	0.0079	0.0150	2.171	1E-3

Table 3: Complementary and synergistic spatial information encoding in astrocytic and neuronal calcium signals. Information about position carried by pairs of ROIs (I) is compared to the sum (I_{LIN}) or to the maximum (I_{MAX}) of the information separately encoded by each member of the pair. A-A, pair composed of two astrocytic ROIs; N-N, pair composed of two neuronal ROIs; A-N, mixed pair composed of one astrocytic and one neuronal ROI. We summarize, mean difference between groups, confidence interval limits, Cohen's d effect size estimate, and p value for Wilcoxon signed-rank test. Data are from 11 imaging sessions on 7 animals.

	p G = 4	p G = 8	p G = 12	p G = 16	p G = 20	p G = 24
Astrocytes vs. Astrocytes + Neurons	6E-7	6E-7	4E-7	6E-7	6E-7	1E-6
Neurons vs. Astrocytes + Neurons	3E-4	5E-4	2E-3	1E-3	1E-3	2E-3

Table 4. Comparison of decoding information about animal's spatial location from neuronal and astrocytic population vectors. p-values for two-tailed paired t-tests with Bonferroni-correction for decoded information of animal's spatial location from population vectors comprising all astrocytic ROIs vs all ROIs of both types (top row) and all neuronal ROIs vs all ROIs of both types (bottom row) during monodirectional virtual navigation shown in Fig. 5. Data from 11 imaging sessions from 7 animals.

	Permutation type	p G = 4	p G = 8	p G = 12	p G = 16	p G = 20	p G = 24
Astrocytes (A)	Chance	1E-3	1E-3	1E-3	1E-3	1E-3	1E-3
	Trial-shuff.	2E-3	2E-3	2E-3	2E-3	2E-3	2E-3
Neurons (N)	Chance	1E-3	1E-3	1E-3	1E-3	1E-3	1E-3
	Trial-shuff.	2E-3	2E-3	2E-3	2E-3	2E-3	2E-3
Astrocytes + Neurons (A-N)	Chance	1E-3	1E-3	1E-3	1E-3	1E-3	1E-3
	Trial-shuff.	2E-3	2E-3	2E-3	2E-3	2E-3	2E-3

Table 5. Hypothesis testing: decoding information about animal’s spatial location from neuronal and astrocytic population vectors. p-values for one-tailed non-parametric permutation tests for decoding information from population vectors comprising either all astrocytic (top row), all neuronal (middle row), or ROIs of both types (bottom row) during monodirectional virtual navigation (see Fig. 5 and Extended data Fig. 13). Significance levels are reported as a function of decoding granularity. For each imaging session and each granularity, null distributions were obtained with 1000 and 500 iterations to estimate chance level and trial shuffling, respectively (Methods). Data from 11 imaging sessions from 7 animals.

	Direction	p G = 4	p G = 8	p G = 12	p G = 16
Decoded information	Forward	1E-3	1E-3	1E-3	1E-3
	Backward	1E-3	1E-3	1E-3	1E-3
Decoding accuracy	Forward	1E-3	1E-3	1E-3	1E-3
	Backward	1E-3	1E-3	1E-3	1E-3

Table 6. Hypothesis testing: decoding performances about animal's spatial location from astrocytic calcium signals during bidirectional virtual navigation. p-values for one-tailed non-parametric permutation tests as a function of decoding granularity for decoded information (see Extended data Fig. 7B, F) and decoding accuracy (see Extended data Fig. 7C, G). Decoding performance is reported for forward- and backward-running directions (see Extended data Fig. 7). For each imaging session and each granularity, null distributions were obtained with 1000 iterations to estimate chance level (Methods). Data from 15 imaging sessions in 4 animals for forward-running direction. Data from 17 imaging sessions in 4 animals for backward-running direction.

Pair type	Class	Mean pairwise correlation	s.e.m.	Lower- bound	Upper- bound	p
Astrocytic ROIs from same cell (A- A_{same})	Reliably encoding spatial information	0.68	0.08	0.55	0.80	2E-4
Astrocytic ROIs from different cells (A-A_{other})	Reliably encoding spatial information	0.31	0.06	0.18	0.44	3E-3
Neurons (N)	Reliably encoding spatial information	0.10	0.01	0.07	0.12	7E-5
Astrocytes + Neurons (A-N)	Reliably encoding spatial information	0.05	0.02	0.01	0.09	3E-3
Astrocytic ROIs from same cell (A- A_{same})	All	0.52	0.03	0.46	0.58	7E-5
Astrocytic ROIs from different cells (A-A_{other})	All	0.28	0.03	0.35	0.21	2E-4
Neurons (N)	All	0.07	0.01	0.04	0.09	7E-5
Astrocytes + Neurons (A-N)	All	0.04	0.01	0.01	0.06	1E-3

Table 7. Pairwise correlations of calcium signals during virtual navigation Descriptive statistics and confidence intervals estimation for pairwise Pearson correlation. Mean, s.e.m, 95% confidence interval limits, and p value for Wilcoxon Rank sums test for $H_0 = 0$ are shown. Pairs were composed either of two astrocytic ROIs belonging to the same astrocyte (A-A_{same}), two

astrocytic ROIs belonging to the different astrocytes (A-A_{other}), two neuronal ROIs (N-N), or one astrocytic and one neuronal ROI (A-N). Correlation was measured for ROI pairs with reliable spatial information or for all possible pairs. Data are from 11 imaging sessions on 7 animals.

	p N _s = 9	p N _s = 12	p N _s = 15	p N _s = 18
Astrocytes (A)	2E-17	2E-13	1E-11	2E-14
Neurons (N)	5E-270	4E-259	5E-245	3E-243

Table 8. Hypothesis testing: visual cues identity does not explain neither astrocytic nor neuronal spatial tuning during virtual navigation. p-values for Binomial tests for astrocytic (top row) or neuronal (bottom row) ROIs encoding reliable spatial information showing a significant decrease in their information content when position is shuffled within individual visual cues (see also Extended data Fig. 14). Significance levels are reported as a function of the number of position bins (N_s). For each imaging session and each N_s, I_v distributions were obtained with 100 iterations in which position was shuffled within visual cues to estimate average I_v (see also Methods). Data from 11 imaging sessions from 7 animals.

	Permutation type	p G = 9	p G = 12	p G = 15	p G = 18
Astrocytes (A)	Position within visual cues	9.8E-04	9.8E-04	9.8E-04	9.8E-04
Neurons (N)	Position within visual cues	9.8E-04	9.8E-04	9.8E-04	9.8E-04

Table 9. Hypothesis testing: animals' position is decoded beyond visual cues identity from both astrocytic and neuronal calcium signals. p-values for Wilcoxon Signed rank tests for decoding information from population vectors comprising either all astrocytic (top row) or all neuronal (bottom row) during monodirectional virtual navigation (see Extended data Fig. 21). Significance levels are reported as a function of decoding granularity. For each imaging session and each granularity, I_V distributions were obtained with 500 iterations in which position was shuffled within visual cues to estimate average I_V (see Methods). Data from 11 imaging sessions from 7 animals.

	Permutation type	p G = 4	p G = 8	p G = 12	p G = 16	p G = 20	p G = 24
Astrocytes (A)	Chance	1E-3	1E-3	1E-3	1E-3	1E-3	1E-3
Neurons (N)	Chance	1E-3	1E-3	1E-3	1E-3	1E-3	1E-3
Astrocytes + Neurons (A-N)	Chance	1E-3	1E-3	1E-3	1E-3	1E-3	1E-3

Table 10. Hypothesis testing: decoding accuracy about animal's spatial location from neuronal and astrocytic population vectors. p-values for one-tailed non-parametric permutation tests for decoding accuracy from population vectors comprising either all astrocytic (top row), all neuronal (middle row), or all ROIs of both types (bottom row) during monodirectional virtual navigation (see Extended data Fig. 13). Significance levels are reported as a function of decoding granularity. For each imaging session and each granularity, null distributions were obtained with 1000 iterations to estimate chance level (Methods). Data from 11 imaging sessions from 7 animals.

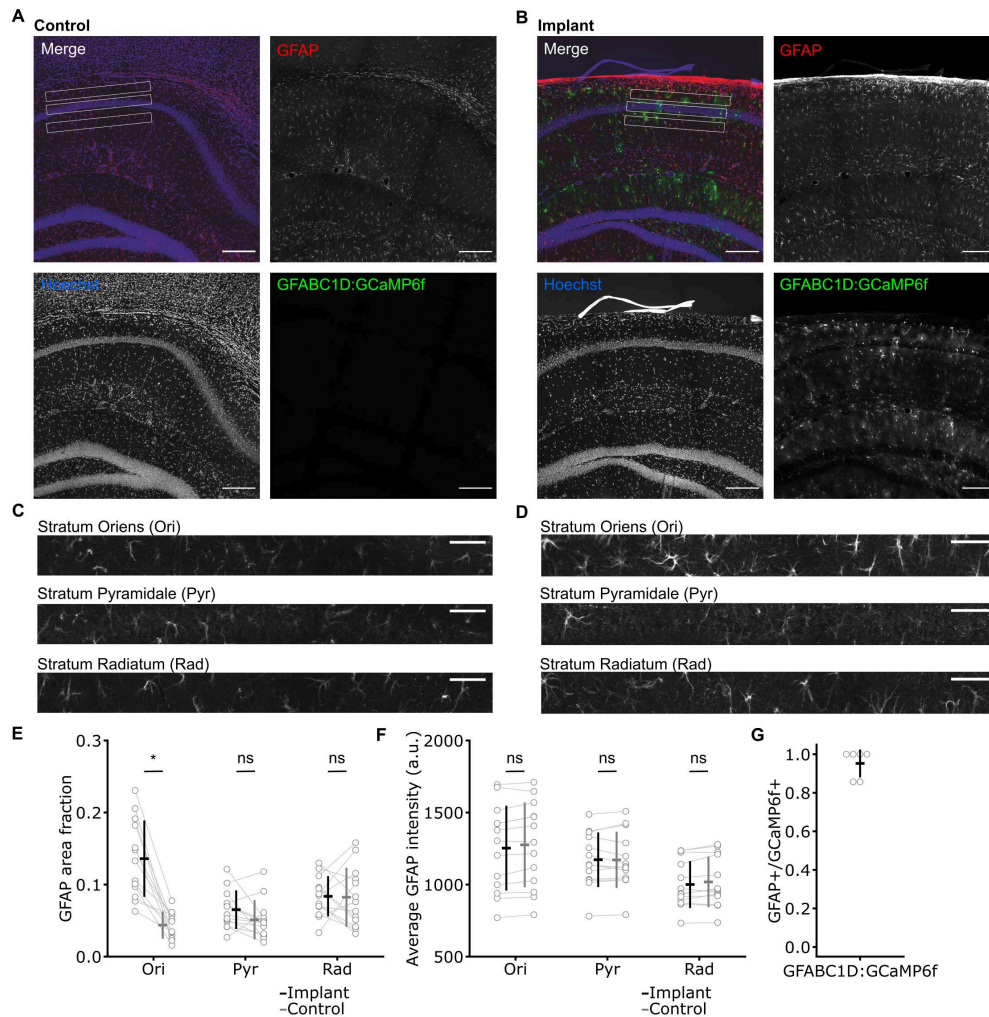


Figure A.1: Chronic CA1 window to monitor astrocytic calcium dynamics in head restrained mice. (A, B) Representative images of hippocampal brain slices from animals injected with AAV5 pZac2.1 gfaABC1D-cyto-GCaMP6f and implanted with a chronic optical window. Images are maximum intensity projection of confocal z-stacks (8 planes, $1.5 \mu\text{m}/\text{step}$) from hemispheres contralateral (A) and ipsilateral (B) to the injection and implant site. Brain slices were stained with anti-GFAP and anti-GFP primary antibodies, which were counterstained with Alexa-546 and Alexa-488 conjugated secondary antibodies, respectively. Cell nuclei were labeled with Hoechst. (C, D) Zoom-in of the ROIs (white rectangles in A and B) used for quantification of GFAP-staining in stratum Oriens, stratum Pyramidale, and stratum Radiatum. (E) Fraction of ROI area immunolabeled for GFAP. (F) Average fluorescence intensity of GFAP-positive pixels in the 3 hippocampal regions under the different experimental conditions. Data are presented as mean \pm SD from 13 slices in 3 animals. In E: $p = 1.4\text{E-}2$, $p = 1.3\text{E-}1$, and $p = 8.2\text{E-}1$ for stratum Oriens, Pyramidale, and Radiatum, respectively. Paired t test. In F: $p = 8.8\text{E-}2$, $p = 9.5\text{E-}1$, and $p = 2.0\text{E-}1$ for stratum Oriens, Pyramidale, and Radiatum, respectively. Paired t test. (G) Fraction of GCaMP6f cells immunolabeled for GFAP ($95 \pm 7\%$, out of a total of 45 GCaMP6f-expressing cells from $N = 6$ sections from 3 mice). Scale bars: $200 \mu\text{m}$ and $50 \mu\text{m}$ for A and B and C and D, respectively. The data presented in this figure can be found in S2 Data. GFAP, glial fibrillary acidic protein; GFP, green fluorescent protein; ROI, region of interest.

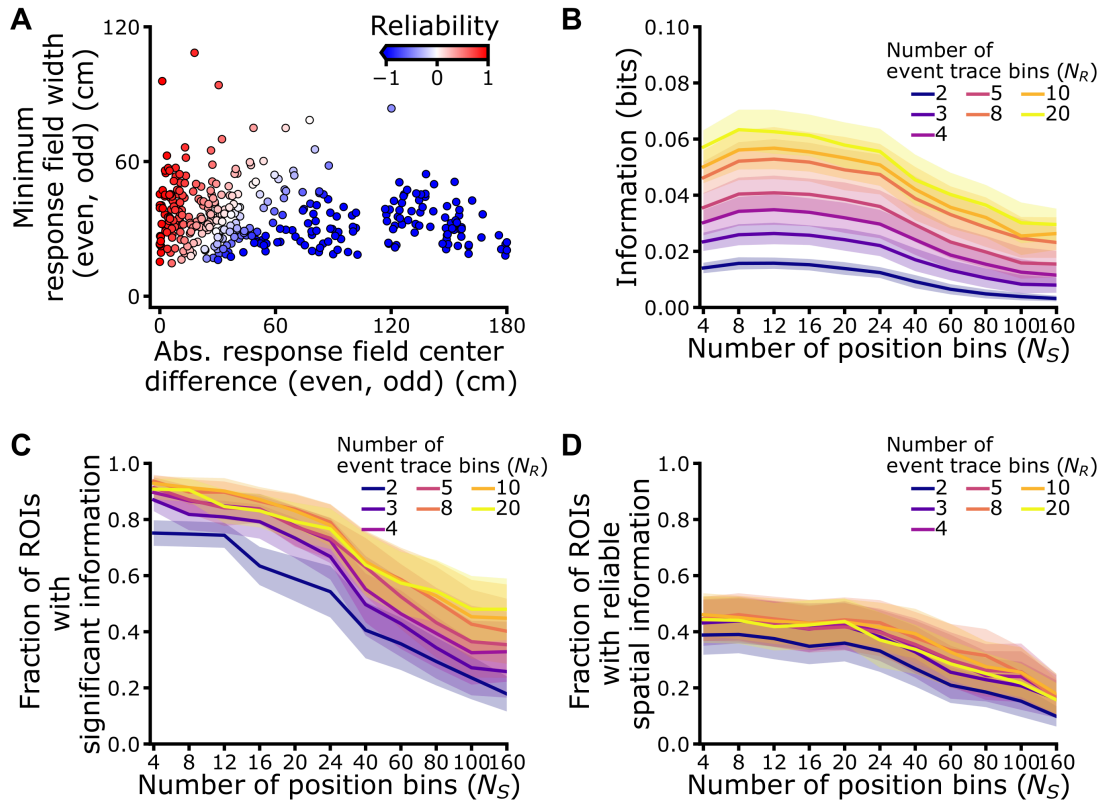


Figure A.2: Identification of reliable spatial modulation of astrocytic calcium signals. (A) Minimum response field width between even and odd trials as a function of the difference in place field position. The pseudocolor scale indicates reliability of the response (see Methods). (B, C) Mutual information values (B) and fraction of ROIs showing significant spatial information (C) as a function of the number of bins for the stimulus (animals' position in the linear track). Colors indicate different binning of the response (calcium event trace). Mutual information values were bias-corrected using bootstrap method (104 iterations). Significance level for information content was set at $p \leq 0.05$. (D) Fraction of ROIs with reliable spatial information as a function of the number of bins for the stimulus. Colors indicate different binning of the response. Data in (B, D) are presented as mean \pm SEM from 7 imaging sessions in 3 animals. The data presented in this figure can be found in S2 Data. ROI, region of interest; SEM, standard error of the mean.

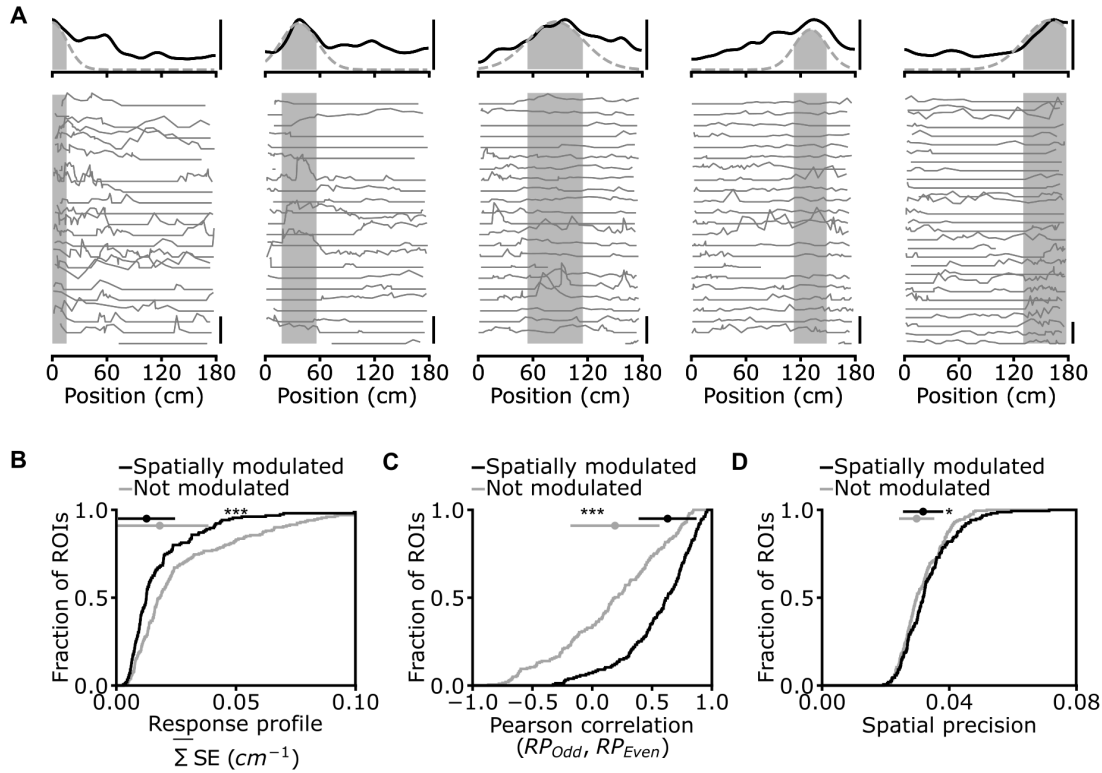


Figure A.3: Reliable spatial modulation of astrocytic calcium signals. (A) Representative traces showing calcium signals for 5 astrocytic ROIs encoding spatial information shown in Fig 1E. Top: Solid black lines indicate the average astrocytic calcium response across runs as a function of spatial position, and the dashed gray lines indicate response field Gaussian fitting function. Bottom: Solid gray lines indicate normalized calcium event traces as a function of position in the virtual corridor for individual runs. Filled gray areas indicate response field width. (B) Cumulative distribution of the mean SE of the response profile in astrocytic ROIs (median \pm MAD $1.3\text{E-}2 \pm 1.2\text{E-}2 \text{ cm}^{-1}$, $N = 155$ out of 356 total ROIs, for ROIs with reliable spatial information, black; $1.8\text{E-}2 \pm 2.0\text{E-}2$, $N = 201$ out of 356 total ROIs, for not modulated ROIs, gray: $p = 1\text{E-}5$, Kolmogorov Smirnov test). (C) Cumulative distribution of Pearson correlation values between astrocytic response profiles in even and odd trials (median \pm MAD 0.63 ± 0.24 , $N = 155$ out of 356 total ROIs for ROIs with reliable spatial information, black; 0.19 ± 0.37 , $N = 201$ out of 356 total ROIs, for not modulated ROIs, gray; $p = 5\text{E-}14$, Kolmogorov Smirnov test). (D) Cumulative distribution of the spatial precision index of the response field of astrocytic ROIs (black: median \pm MAD $3.2\text{E-}2 \pm 0.6\text{E-}2$, $N = 155$ out of 356 total ROIs, for ROIs with reliable spatial information; gray: $3.0\text{E-}2 \pm 0.5\text{E-}2 \text{ cm}^{-1}$, $N = 201$ out of 356 total ROIs, for not modulated ROIs: $p = 3.8\text{E-}2$, Kolmogorov–Smirnov test). In all panels, data from 7 imaging sessions in 3 animals. The data presented in this figure can be found in S2 Data. MAD, median absolute deviation; ROI, region of interest; SE, standard error.

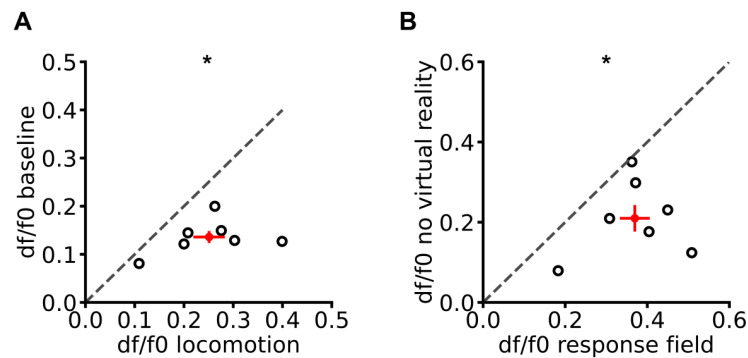


Figure A.4: Modulation of astrocytic calcium responses during locomotion and virtual navigation. (A) Scatterplot of the average $\Delta F/F_0$ of astrocytic ROIs during baseline (mouse speed ≤ 1 cm/s) versus during locomotion (mouse speed > 1 cm/s). Under both conditions, the mouse was immersed in the virtual reality. Black open dots represent averages of each imaging session. The red cross shows the mean \pm SEM of plotted data (mean $\Delta F/F_0$ during baseline 0.14 ± 0.01 ; mean $\Delta F/F_0$ during locomotion 0.25 ± 0.03 ; $N = 356$ ROIs; $p = 0.016$ Wilcoxon signed rank test). (B) Same as in (A) but for $\Delta F/F_0$ values measured in astrocytic ROIs encoding reliable spatial information when the mouse was not exposed to the visual stimulation of the virtual reality (during intertrial intervals) versus when the mouse was passing through each ROIs' response fields (mean $\Delta F/F_0$ during without visual stimulation 0.21 ± 0.03 ; mean $\Delta F/F_0$ inside the response field 0.37 ± 0.04 ; $N = 155$ out of 356 total ROIs; $p = 0.016$ Wilcoxon signed rank test). Data in (A, B) from 7 imaging sessions in 3 animals. The data presented in this figure can be found in S2 Data. ROI, region of interest; SEM, standard error of the mean.

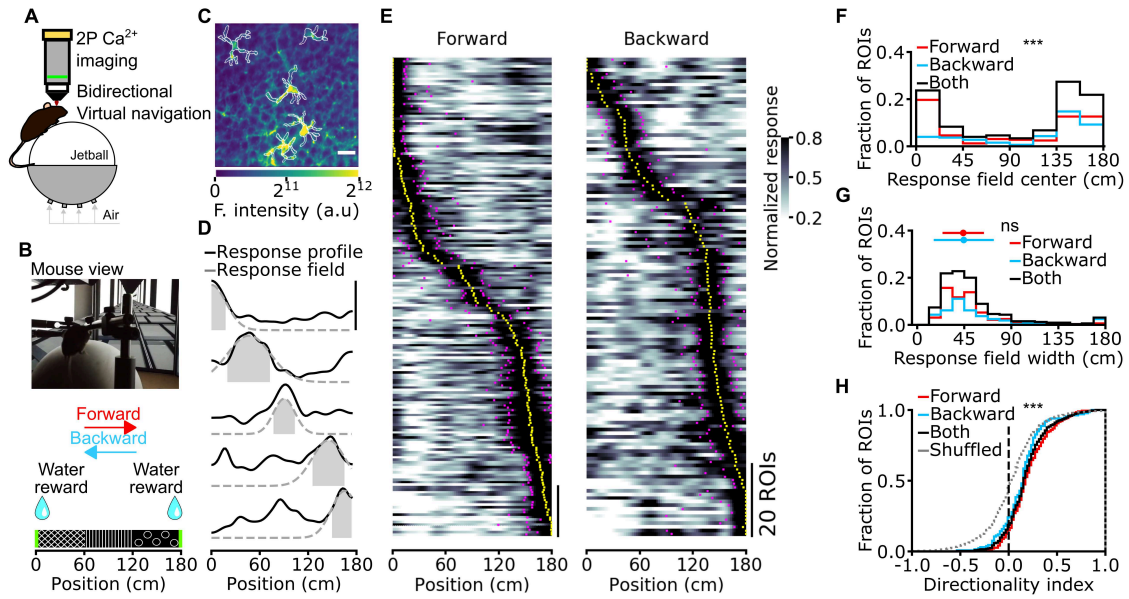


Figure A.5: Calcium signals of CA1 astrocytes encode direction selective spatial information during virtual bidirectional navigation. (A) Two-photon functional imaging of CA1 astrocytes is performed during bidirectional virtual navigation. (B) Head-restrained mice run on an air-suspended spherical treadmill in a linear virtual track in both forward and backward directions. Water rewards are delivered at either end of the virtual corridor. (C) Median projection of GCaMP6f-labeled astrocytes in the CA1 pyramidal layer. White lines indicate segmented ROIs. Scale bar: $20\ \mu\text{m}$. (D) Calcium signals for 5 representative astrocytic ROIs reliably encoding spatial information across the corridor length. Solid black lines indicate the average astrocytic calcium response across trials as a function of spatial position. Dashed gray lines and filled gray areas indicate the Gaussian fitting function and the response field width (see Methods), respectively. (E) Normalized astrocytic calcium responses as a function of position for astrocytic ROIs with reliable spatial information. Trials are divided according to running direction (forward and backward). For forward trials, informative ROIs are $N = 192$ out of 648 total ROIs, mean \pm SD: $29 \pm 13\%$; for backward trials, informative ROIs are $N = 133$ out of 648 ROIs, mean \pm SD: $20 \pm 13\%$, $p = 0.09$, Wilcoxon signed rank test. Scale bar: 20 ROIs. Yellow dots indicate the center position of the response field, and the magenta dots indicate the width of the field response. (F) Distributions of astrocytic response field position for forward and backward running direction. Median \pm MAD 93 ± 66 cm, $N = 192$ out of 648 total ROIs for the forward direction; 138 ± 47 cm $N = 133$ out of 648 total ROIs for the backward direction; $p = 9\text{E-}7$, Kolmogorov–Smirnov test). (G) Distributions of response field width for the forward and backward running direction (response field width, 44 ± 19 cm, $N = 192$ out of 648 total ROIs for the forward direction; response field width, 44 ± 28 cm, $N = 133$ out of 648 total ROIs for the backward direction; $p = 0.34$, Wilcoxon rank sums test). (H) DI for forward and backward running directions (DI, 0.18 ± 0.16 , $N = 192$ out of 648 total ROIs for forward trials; DI, 0.16 ± 0.16 , $N = 133$ out of 648 total ROIs for backward trials; $p = 8\text{E-}19$ and $p = 2\text{E-}8$, respectively, Kolmogorov–Smirnov test versus shuffled distribution). In all panels, data from 18 imaging sessions in 4 animals. The data presented in this figure can be found in S2 Data. DI, directionality index; MAD, median absolute deviation; ROI, region of interest; SD, standard deviation; SEM, standard error of the mean.

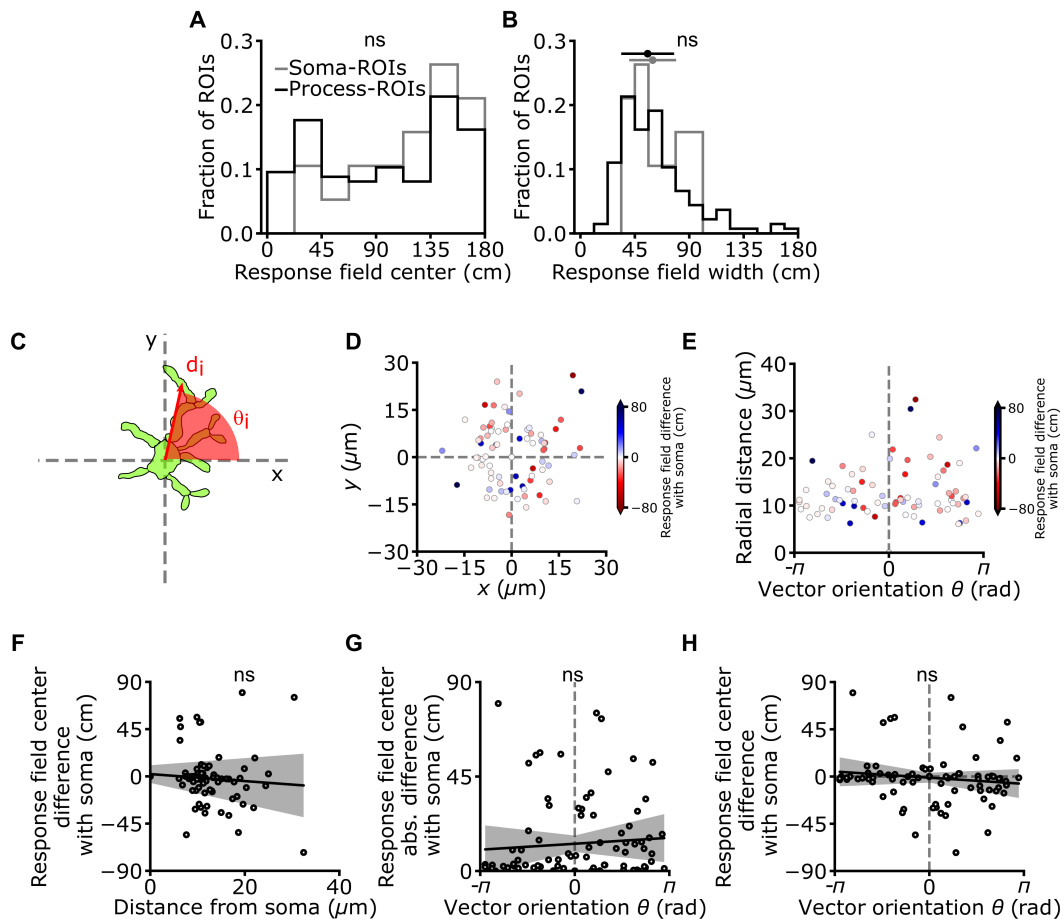


Figure A.6: Anatomical organization of subcellularly localized astrocytic calcium signals. (A) Distribution of field position for soma ROIs and process ROIs ($p = 0.36$, Kolmogorov–Smirnov test). (B) Distribution of response field width for astrocytic soma ROIs and process ROIs (median width for soma ROIs: 60 ± 19 cm; median width for process ROIs: 56 ± 22 cm, $p = 0.36$, Wilcoxon rank sums test). (C) For each pair of ROIs within a given astrocyte, the distance (d) between the centers of 2 ROIs and the angle between the line connecting the 2 ROI centers and the x-axis are calculated. Only astrocytes showing significant spatial modulation in the soma and at least 1 process were used for this analysis. (D, E) Difference in field position of a process with respect to the field position of its corresponding soma, expressed as function of Cartesian (D) and polar (E) coordinates of the ROI centers. (F) Difference in response field position of a process with respect to the field position of its corresponding soma as a function of the process distance from cell soma ($R^2 = 0.01$, $p = 3.3E-1$, Wald test, data from 19 cells from 7 imaging sessions on 3 animals). (G, H) Absolute value (G) or signed (H) difference in response field position of a process ROI with respect to the field position of its corresponding soma as a function of the process angular coordinate (absolute value of difference in response field $R^2 = 0.01$, $p = 4.8E-1$, Wald test; signed value of difference in response field $R^2 = 0.01$, $p = 4.1E-1$, Wald test, data from 19 cells from 7 imaging sessions on 3 animals). The data presented in this figure can be found in S2 Data. ROI, region of interest.

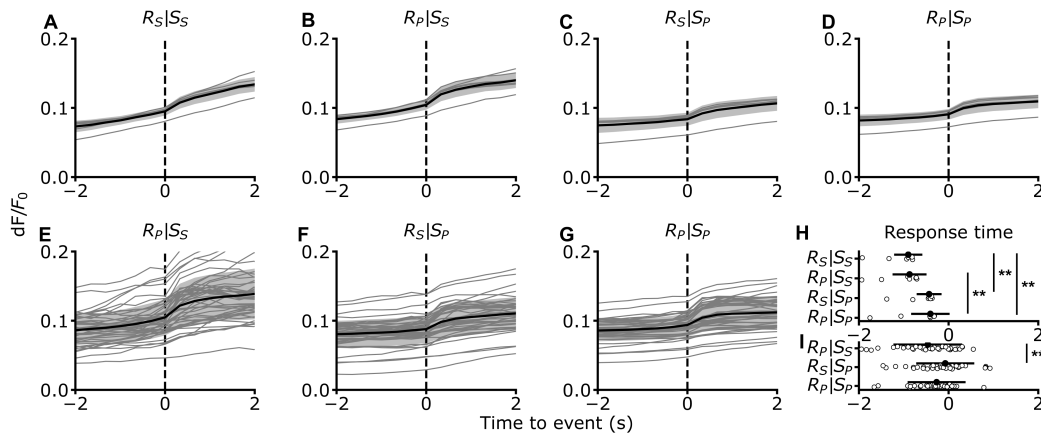


Figure A.7: Temporal relationships among subcellularly localized astrocytic calcium signals. (A) Event triggered average of astrocytic calcium responses. Calcium responses of putative receiver (R) ROIs are aligned to calcium events of putative source (S) ROIs according to anatomic identities of ROIs (e.g., somatic receiver ROIs and somatic source ROIs). Data from 7 imaging sessions in 3 animals. Black line indicates the mean, and shaded area the standard deviation. (B–D) Same as in (A) for pairs of process receiver and somatic source (B), somatic receiver and process source (C), and process receiver and process source (D). (E–G) Same as in (B–D) but for pairs of ROIs belonging to the same astrocyte ($N = 46$ astrocytes from 7 imaging sessions in 3 animals). (H) Response time (see Methods) for signals shown in (A–D). $p = 6E-4$, Friedman test with Nemenyi post hoc correction. (I) Response time for signals shown in (E–G). $p = 7E-3$, Friedman test with Nemenyi post hoc correction. The data presented in this figure can be found in S2 Data. ROI, region of interest.

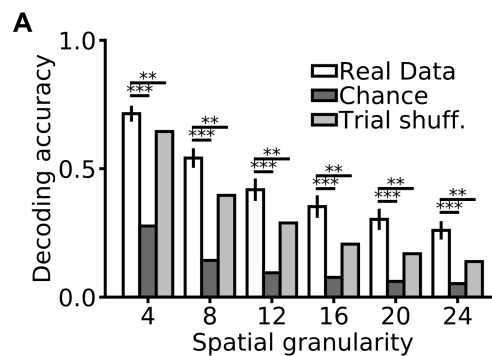


Figure A.8: Decoding animal's position from astrocytic calcium signals in the unidirectional virtual navigation task. (A) Decoding accuracy as a function of spatial granularity on real (white), chance (dark gray), and trial-shuffled (gray) data (see Methods). Data are presented as mean \pm SEM from 7 imaging sessions on 3 animals; see also S2 Table. The data presented in this figure can be found in S2 Data. SEM, standard error of the mean.

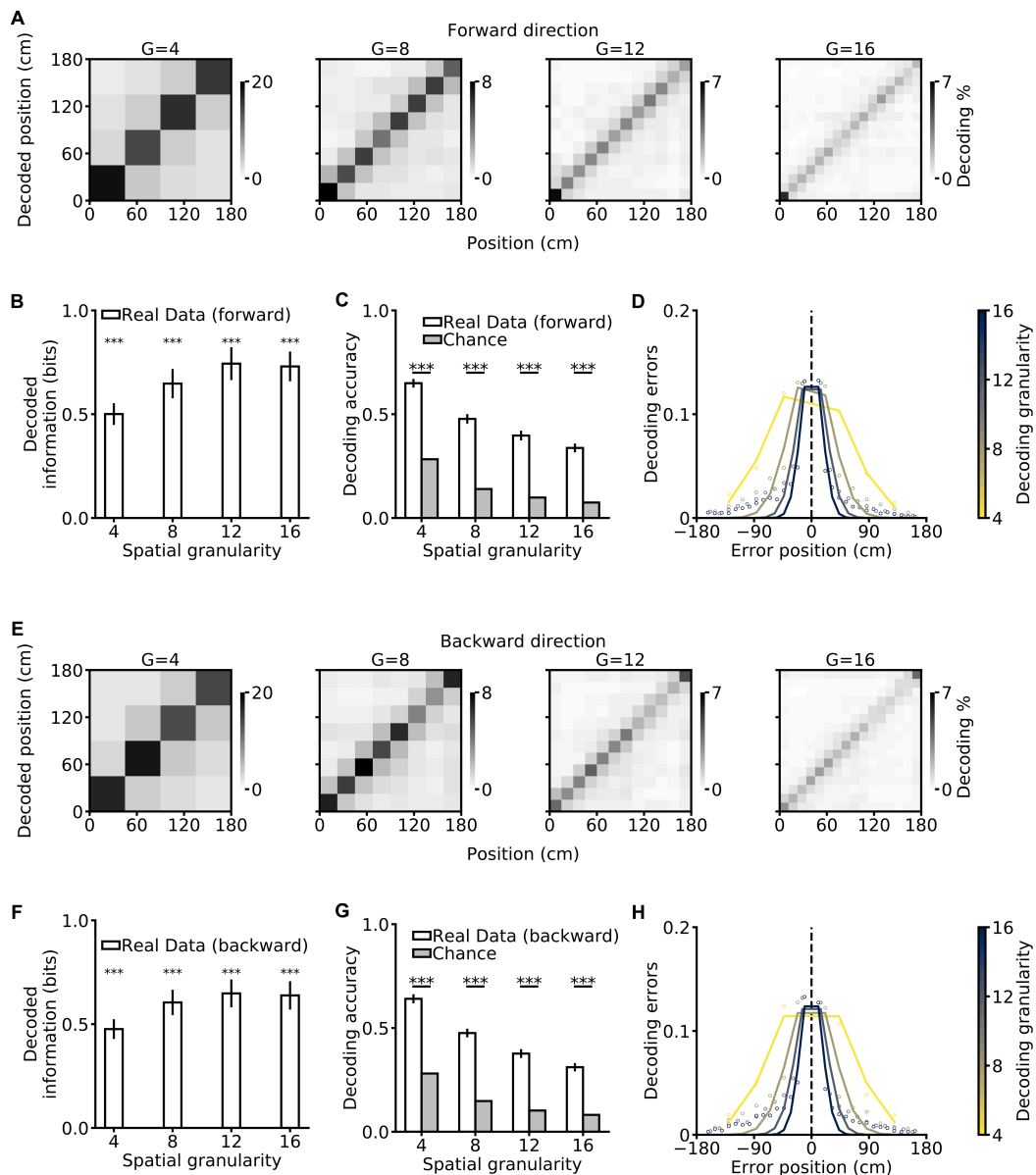


Figure A.9: Decoding animal's position from astrocytic calcium signals in the bidirectional virtual navigation task. (A) Confusion matrices of an SVM classifier for different spatial granularities ($G = 4, 8, 12, 16$) for trials in which the mouse was running in the forward direction (forward). The actual position of the animal is shown on the x-axis, the decoded position on the y-axis. Gray scale indicates the number of events in each matrix element. (B) Decoded information as a function of spatial granularity on real (white) and chance (gray) data for forward trials. (C) Decoding accuracy as a function of spatial granularity. (D) Decoding error as a function of the error position within the confusion matrix for forward trials. The color code indicates spatial granularity. In panels (A–D), data from 15 imaging sessions in 4 animals. (E–H) Same as in (A–D) for trials in the backward direction. Data from 17 imaging sessions in 4 animals. In (B, C, F, G), data are presented as mean \pm SEM. See also S6 Table. The data presented in this figure can be found in S3 Data. SEM, standard error of the mean; SVM, support vector machine.

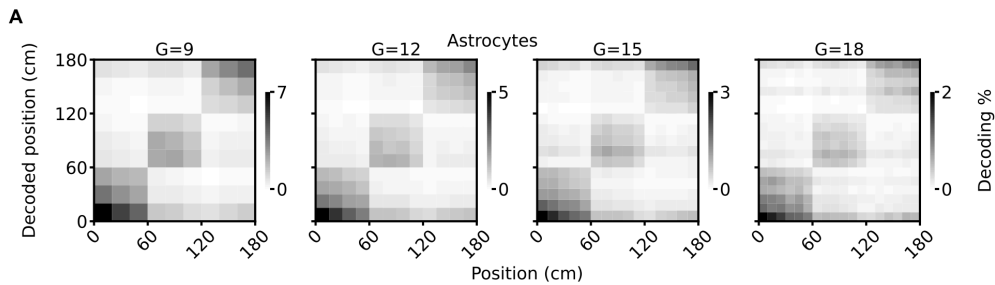


Figure A.10: Visual cues identities do not explain animal’s position decoding from astrocytic calcium signals. (A) Confusion matrices of an SVM classifier decoding the mouse’s position using population vectors data comprising astrocytic ROIs in which position was shuffled within visual cues. Shuffling position within visual cues decoupled spatial information encoded in the population vector from the information related to visual cues identity (see Methods). The true position of the animal is shown on the x-axis and the decoded position on the y-axis. Gray scale indicates the percentage of occurrence of each matrix element (Decoding). Results are shown for various spatial granularities ($G = 9, 12, 15, 18$). In all panels, data from 500 permutations on 7 imaging sessions in 3 animals are shown. The data presented in this figure can be found in S3 Data. ROI, region of interest; SVM, support vector machine.

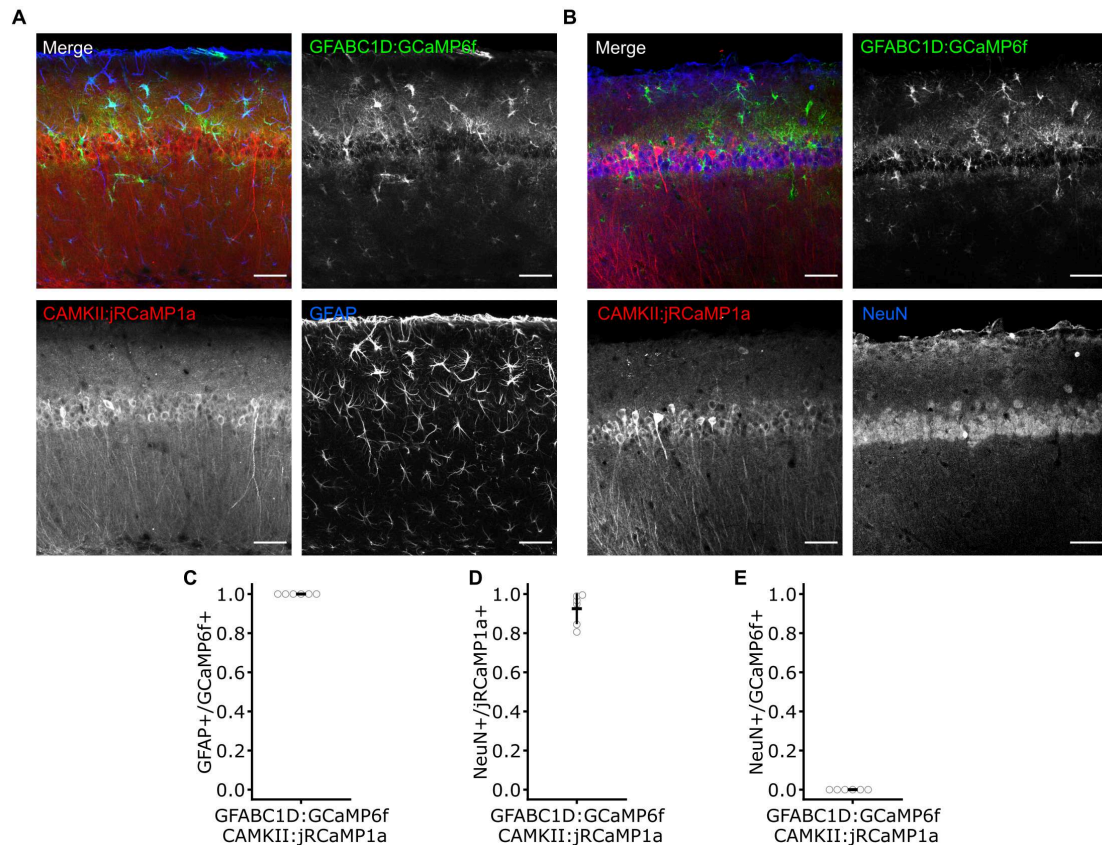


Figure A.11: Chronic CA1 window to simultaneously monitor astrocytic and neuronal calcium signals in head restrained mice. (A, B) Representative images of hippocampal CA1 areas from animals transduced with AAV5 pZac2.1 gfaABC1D-cyto-GCaMP6f and AAV1/2 pAAV CAMKII-jRCaMP1a implanted with a chronic optical window. Images are maximum intensity projection of confocal z-stacks (9 planes, $2\ \mu\text{m}/\text{step}$) from brain slices stained either with anti-GFAP (A) or an anti-NeuN primary antibody (B). In both cases, counterstaining was performed with an Alexa-647 conjugated secondary antibody. (C) Related to (A): Fraction of GCaMP6f-expressing cells immunolabeled for GFAP ($100 \pm 0\%$, out of a total of 71 GCaMP6f-expressing cells from $N = 6$ sections from 3 mice). (D) Related to (B): fraction of jRCaMP1a-expressing cells immunolabeled for NeuN ($93 \pm 8\%$, out of a total of 985 jRCaMP1a-expressing cells from $N = 6$ sections from 3 mice). (E) Same as in (D) but for GCaMP6f-expressing cells ($0 \pm 0\%$, out of a total of 50 GCaMP6f-expressing cells, from $N = 6$ sections from 3 mice). Scale bars in A and B: $50\ \mu\text{m}$. The data presented in this figure can be found in S3 Data. GFAP, glial fibrillary acidic protein.

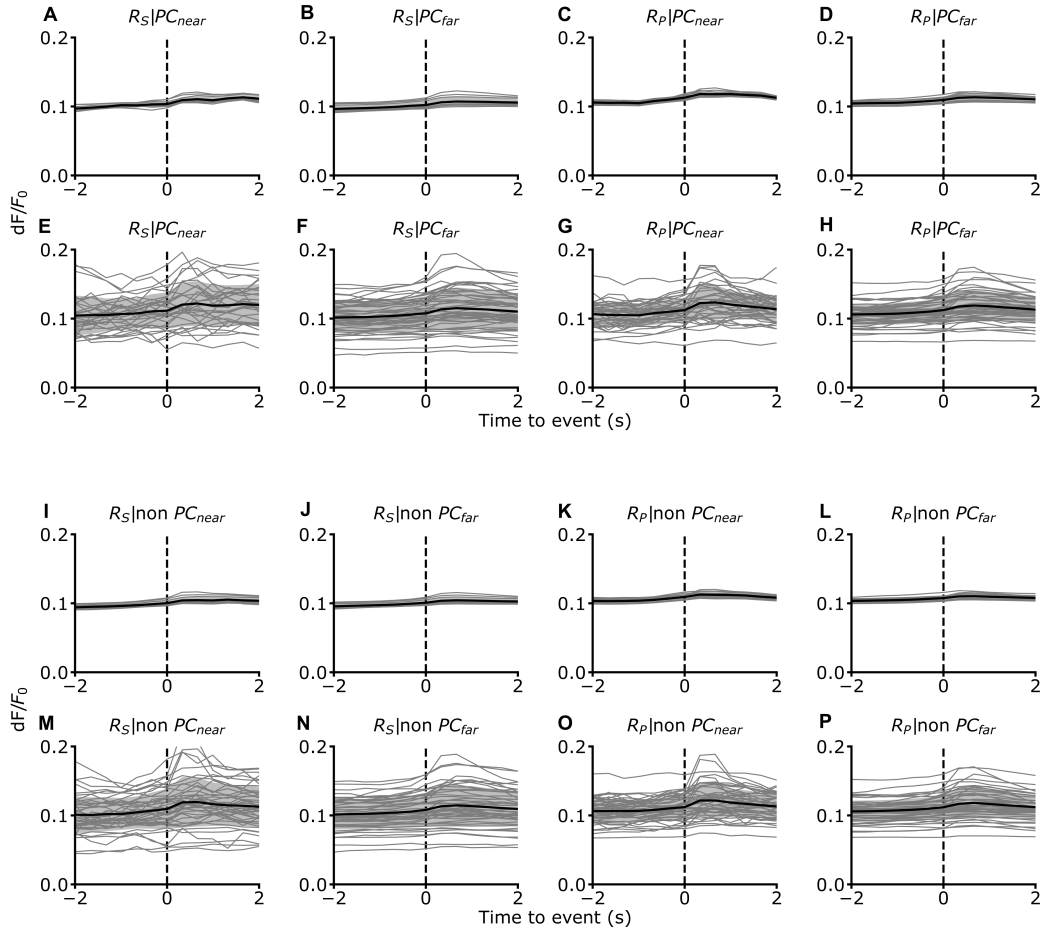


Figure A.12: Temporal relationships between astrocytic and neuronal signals. (A–D) Event triggered average of astrocytic calcium responses. Calcium responses of putative receiver (R) ROIs are aligned to calcium events of neuronal PCs. Astrocytic receiver ROIs could be in the soma (s) or processes (p). Neuronal cells were classified as being close ($\leq 15 \mu\text{m}$) or far ($> 15 \mu\text{m}$) from astrocytic receiver ROIs. Data from 11 imaging sessions in 7 animals. The black line indicates the mean, the shaded area the standard deviation. (E, F) Same as in (A–D) but for receiver ROIs belonging to the same astrocyte ($N = 23$ cells from 11 imaging sessions in 7 animals). (I–L) Same as in (A–D) but calcium responses of putative receiver (R) ROIs are aligned to calcium events of nonspatially informative cells (non-PC). Data from 11 imaging sessions in 7 animals. (M–P) Same as in (I–L) but for receiver ROIs belonging to the same astrocyte ($N = 48$ astrocytes from 11 imaging sessions in 7 animals). The data presented in this figure can be found in S3 Data. PC, place cell; ROI, region of interest.

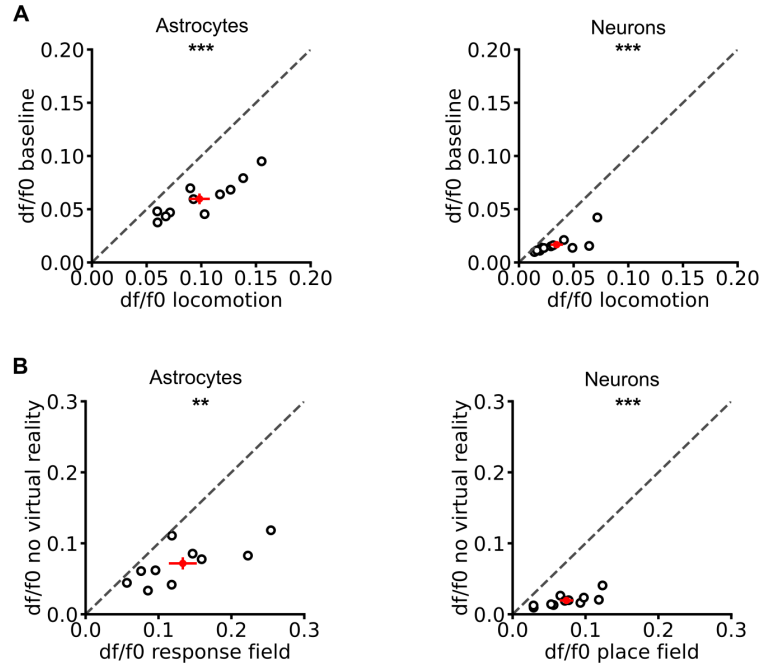


Figure A.13: Modulation of astrocytic and neuronal calcium responses during locomotion and virtual navigation. (A) Scatterplot of the average $\Delta F/F_0$ of astrocytic ROIs during baseline (mouse speed ≤ 1 cm/s) versus during locomotion (mouse speed > 1 cm/s). Under both conditions, the mouse was immersed in the virtual reality. Black open dots show averages of each imaging session. The red cross shows the mean \pm SEM of plotted data. Average $\Delta F/F_0$ values were measured in astrocytic ROIs (left; mean $\Delta F/F_0$ during baseline 0.06 ± 0.01 ; mean $\Delta F/F_0$ during locomotion 0.10 ± 0.01 , $N = 341$ ROIs; $p = 9.8E-4$ Wilcoxon signed rank test) and neuronal ROIs (right; mean $\Delta F/F_0$ during baseline 0.017 ± 0.003 ; mean $\Delta F/F_0$ during locomotion 0.03 ± 0.01 , $N = 870$ ROIs; $p = 9.8E-4$ Wilcoxon signed rank test) recorded from mice co-injected with AAV5 pZac2.1 gfaABC1D-cyto-GCaMP6f and AAV1/2 pAAV-CAMKII-jRCaMP1a. (B) Same as in (A) but for $\Delta F/F_0$ values measured in ROIs encoding reliable spatial information when the mouse was not exposed to the visual stimulation of the virtual reality versus when the mouse was passing through each ROIs' response fields. Astrocytic ROIs, left, (mean $\Delta F/F_0$ without visual stimulation 0.07 ± 0.01 ; mean $\Delta F/F_0$ inside the response field 0.13 ± 0.02 ; $p = 0.016$ Wilcoxon signed rank test), neuronal ROIs, right, (mean $\Delta F/F_0$ without visual stimulation 0.020 ± 0.002 ; mean $\Delta F/F_0$ inside the response field 0.07 ± 0.01 ; $p = 0.016$ Wilcoxon signed rank test). Data in (A, B) are presented as mean \pm SEM and come from 11 imaging sessions in 7 animals. The data presented in this figure can be found in S3 Data. ROI, region of interest; SEM, standard error of the mean.

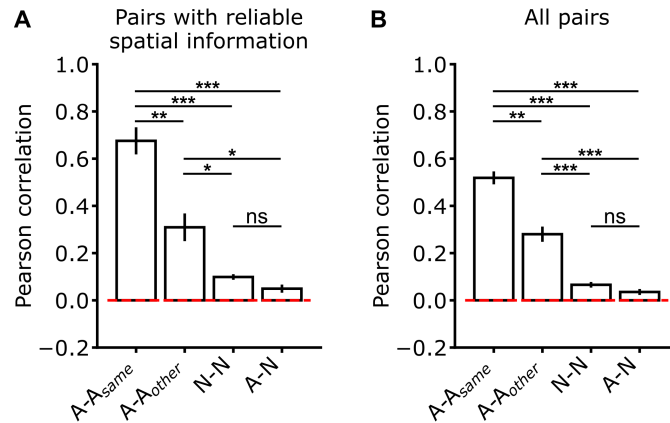


Figure A.14: Pairwise correlations of calcium signals during virtual navigation. (A, B) Pearson correlation for different pairs of ROIs. Pairs were composed either of two astrocytic ROIs belonging to the same astrocyte (A-Asame), two astrocytic ROIs belonging to the different astrocytes (A-Aother), two neuronal ROIs (N-N), or one astrocytic and one neuronal ROI (A-N). Red line indicates the zero correlation level. In (A), only results for ROI pairs with reliable spatial information are reported ($p = 5.2E-3$, $p = 6.5E-4$, $p = 9.4E-4$, $p = 1.5E-2$, $p = 1.5E-2$, $p = 9.9E-2$ for A-Asame versus A-Aother, A-Asame versus N-N, A-Asame versus A-N, A-Aother versus N-N, A-Aother versus A-N, N-N versus A-N, respectively. Wilcoxon rank sums test with Bonferroni post hoc correction). In (B), results for all possible pairs are displayed ($p = 2.6E-3$, $p = 4.3E-4$, $p = 4.3E-4$, $p = 8.6E-4$, $p = 8.6E-4$, $p = 1.4E-1$ for A-Asame versus A-Aother, A-Asame versus N-N, A-Asame versus A-N, A-Aother versus N-N, A-Aother versus A-N, N-N versus A-N, respectively. Wilcoxon rank sums test with Bonferroni post hoc correction). Data are presented as mean \pm SEM from 11 imaging sessions on 7 animals. Data from astrocytic recording comprises 36 cells in which there was significant spatial modulation in at least 1 ROI. The data presented in this figure can be found in S4 Data. ROI, region of interest; SEM, standard error of the mean.

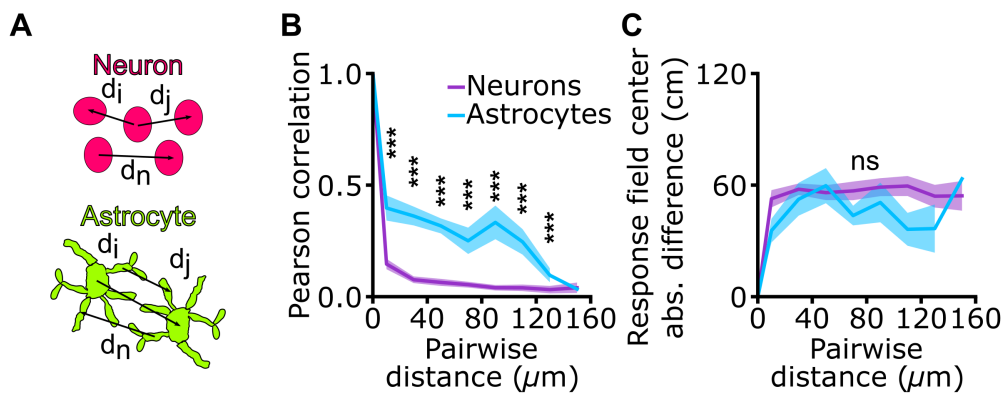


Figure A.15: Pairwise correlation of calcium signals and difference in field position as a function of pairwise distance. (A) The distance (d) between the centers 2 ROIs comprising a pair is computed for all astrocytic (top) and neuronal (bottom) ROIs. (B, C) Pearson correlation (B) and difference between response field position (C) as a function of pairwise distance for pairs of astrocytic ROIs with reliable spatial information (cyan) and pairs of neuronal ROIs with reliable spatial information (purple). Data are expressed as mean \pm SEM from 11 imaging sessions on 7 animals. (A) $p = 8\text{E-}4$, $p = 8\text{E-}4$, $p = 1\text{E-}4$, $p = 1\text{E-}3$, $p = 1\text{E-}3$, $p = 1\text{E-}3$, $p = 8\text{E-}4$, and $p = 2\text{E-}1$ for 10, 30, 70, 90, 110, 130, and 150 μm pairwise distances, respectively. Two-sample Kolmogorov–Smirnov test with Bonferroni post hoc correction. (B) $p = 1$, $p = 1$, $p = 0.7$, $p = 1$, $p = 1$, $p = 1$, $p = 0.2$, and $p = 0.2$ for 10, 30, 70, 90, 110, 130, and 150 μm pairwise distances, respectively. Two-sample Kolmogorov–Smirnov test with Bonferroni post hoc correction. Data from astrocytic recording comprises 36 cells in which there was significant spatial modulation in at least 1 ROI. The data presented in this figure can be found in S5 Data. ROI, region of interest; SEM, standard error of the mean.

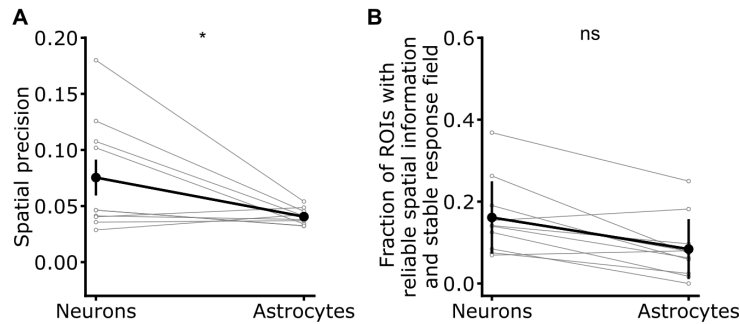


Figure A.16: Precision and stability of neuronal and astrocytic spatial responses. (A) Spatial precision index for simultaneously recorded neuronal and astrocytic response fields (mean \pm SEM; neuronal responses $7.5E-2 \pm 1.6E-2$; astrocytic responses $4.1E-2 \pm 0.2E-2$; $p = 4.6E-2$ Wilcoxon signed rank test; data from 11 imaging sessions on 7 animals). (B) Fraction of neuronal and astrocytic ROIs showing reliable spatial information and stable response field (mean \pm SD; neurons 0.16 ± 0.09 ; astrocytic responses 0.08 ± 0.07 ; $p = 2.9E-1$ Wilcoxon signed rank test; data from 11 imaging sessions on 7 animals). The data presented in this figure can be found in S5 Data. ROI, region of interest; SD, standard deviation; SEM, standard error of the mean.

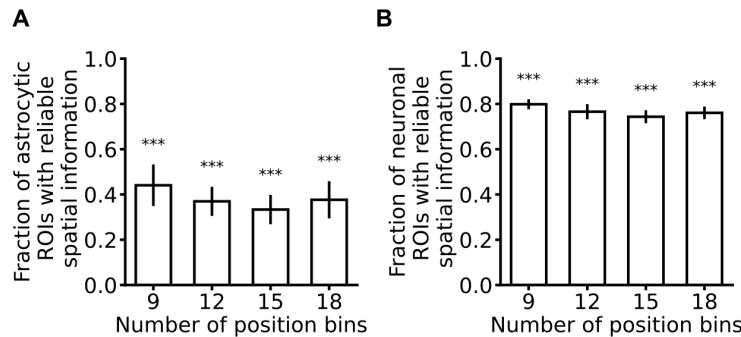


Figure A.17: The majority of spatial information in astrocytes and neurons is genuine spatial information that cannot be explained by tuning to visual cues. (A, B) Fraction of astrocytic (A) and neuronal (B) ROIs encoding reliable spatial information showing a significant decrease in their information content when position is shuffled within visual cues. Shuffling position within individual visual cues decoupled spatial information encoded in the astrocytic response from the information related to visual cues identity (see Methods). The fraction of ROIs showing significant information loss is shown as function of the number of position bins used to compute mutual information. Data are presented as mean \pm SEM from 11 experimental sessions in 7 animals, ($N = 76$ for astrocytic ROIs, $N = 335$ for neuronal ROIs, binomial test, see S8 Table). The data presented in this figure can be found in S5 Data. ROI, region of interest; SEM, standard error of the mean.

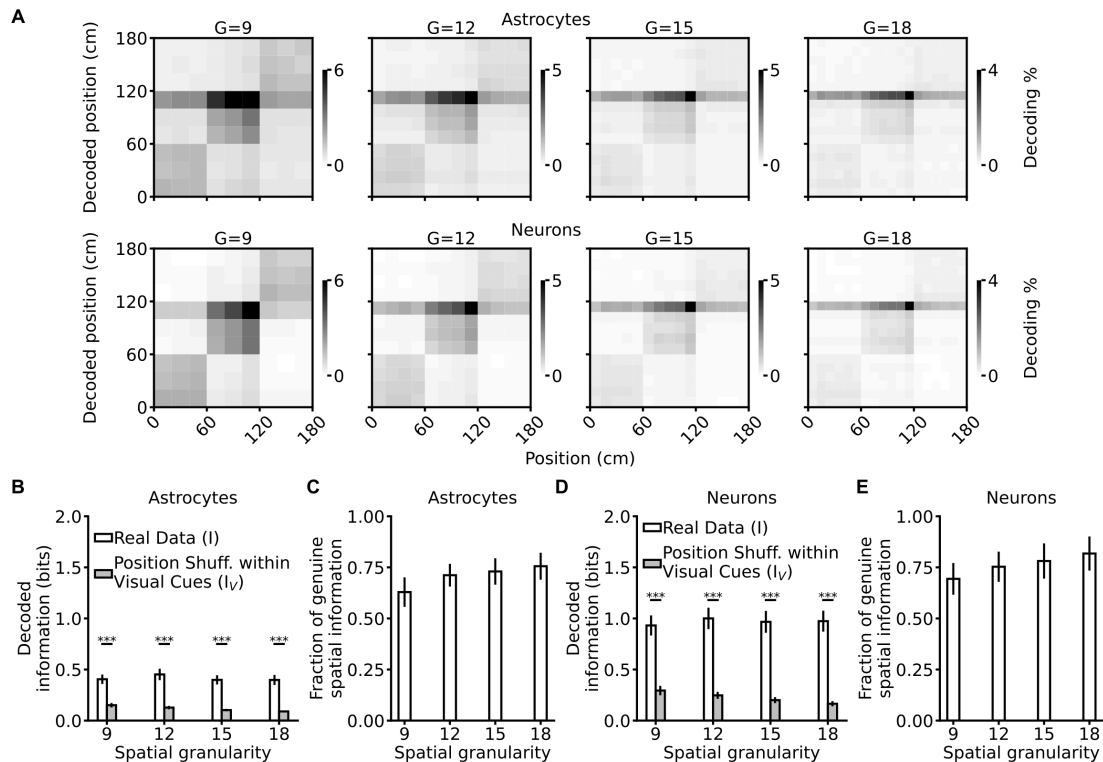


Figure A.18: Visual cues identity does not explain animal's position decoding from neither astrocytic nor neuronal calcium signals. (A) Confusion matrices of an SVM classifier decoding the mouse's position using population vectors comprising either astrocytic (top) or neuronal (bottom) ROIs in which position was shuffled within visual cues. Shuffling position within visual cues decoupled spatial information encoded in the population vector from the information related to visual cues identity (see Methods). The true position of the animal is shown on the x-axis and the decoded position on the y-axis. Gray scale indicates the percentage of occurrence of each matrix element. Results are shown for various spatial granularities ($G = 9, 12, 15, 18$). (B) Decoded information from astrocytic population vectors as a function of decoding granularity on real data (white) and for data in which position is shuffled within visual cues (gray, see Methods). (C) Fraction of genuine spatial information in astrocytic population vectors computed shuffling position within individual visual cues. Results are shown as a function of decoding granularity. (D, E) Same as in (B, C) but from population vectors comprising neuronal ROIs. In all panels, data are shown as mean \pm SEM and were obtained from 11 imaging sessions in 7 animals (see also S9 Table). The data presented in this figure can be found in S5 Data. ROI, region of interest; SEM, standard error of the mean; SVM, support vector machine.

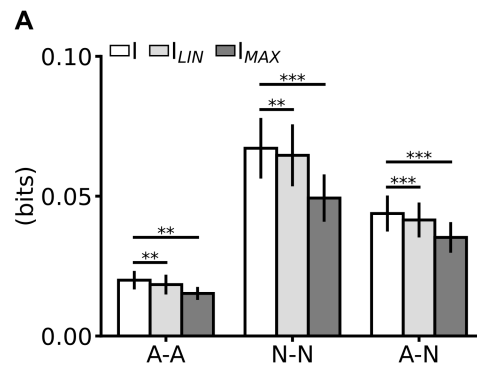


Figure A.19: Astrocytes and neurons encode complementary and synergistic spatial information. (A) Mutual information about position encoded by pairs of ROIs (I) is shown in comparison to the sum (I_{LIN}) and to the maximum (I_{MAX}) of the information separately encoded by each component of the pair. A-A, pair composed of 2 astrocytic ROIs; N-N, pair composed of 2 neuronal ROIs; A-N, mixed pair composed of one astrocytic and one neuronal ROI. For this analysis, the values of information were computed using the “shuffled” bias correction procedure (see methods) which overcorrects the bias inducing an underestimation of I (I versus I_{LIN} : A-A: $p = 1E-2$, N-N: $p = 7E-3$, A-N: $p = 1E-3$; I versus I_{MAX} : A-A: $p = 5E-3$, N-N: $p = 1E-3$, A-N: $p = 1E-3$, Wilcoxon signed rank test, see also S3 Table). Data are represented as mean \pm SEM from 11 imaging sessions in 7 animals. The data presented in this figure can be found in S5 Data. ROI, region of interest, SEM, standard error of the mean.

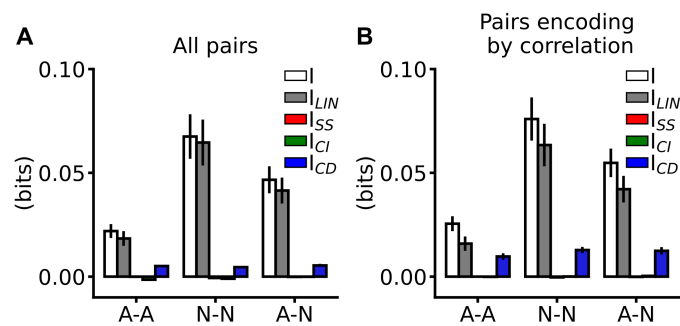


Figure A.20: Position-dependent correlations contribute to synergistic information encoding. (A, B) Information breakdown for the different types of ROI pairs: 2 astrocytic ROIs (A-A), 2 neuronal ROIs (N-N), or one astrocytic and one neuronal ROI (A-N). Pairs were classified as synergistic (B) based on the value of ΔI (see Methods). I (white) is the mutual information about position encoded by the pair. I_{LIN} (gray) is the sum of the mutual information about position independently encoded in the response of each member of the pair. I_{SS} (red) is the redundant information component quantifying similarity in the responses of the members of the pair. I_{CI} (green) and I_{CD} (blue) quantify the information contribution of correlation independent or dependent on position, respectively. Data are represented as mean \pm SEM and were collected in 11 imaging sessions on 7 animals. The data presented in this figure can be found in S5 Data. ROI, region of interest; SEM, standard error of the mean.

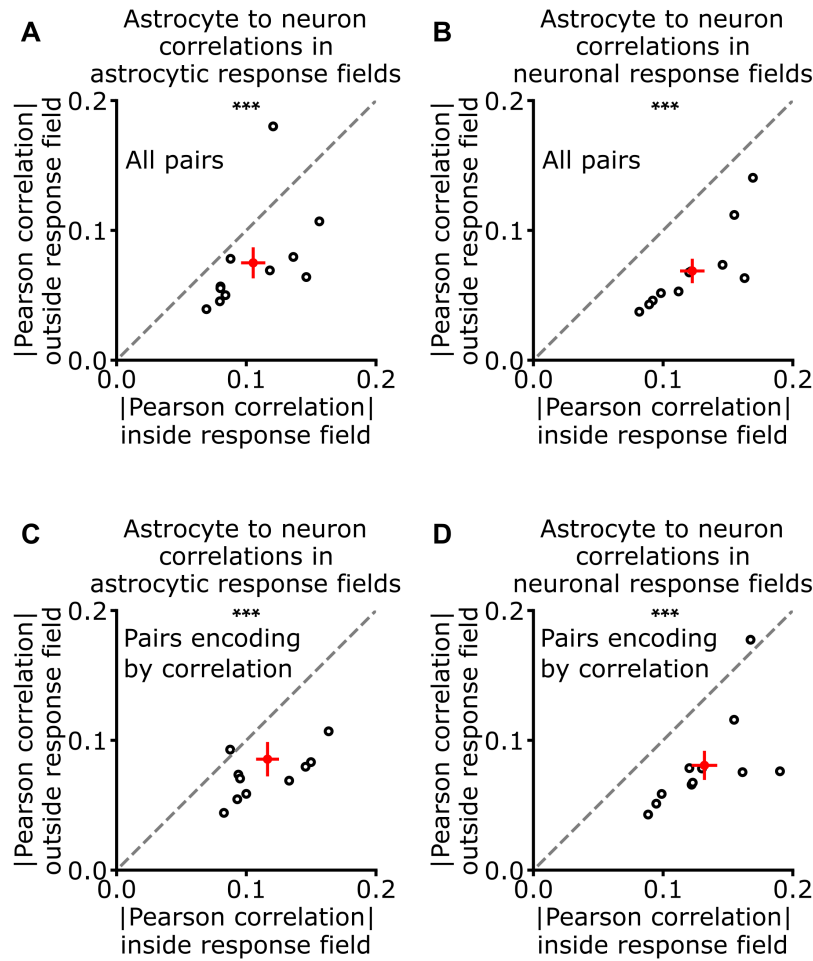


Figure A.21: Correlation between astrocytes and neurons is animal’s position-dependent. (A–D) Scatterplot of the absolute value of Pearson correlation outside the response field against the absolute value of Pearson correlation inside the response field for pairs comprising one astrocytic and one neuronal ROI. Black open dots show averages of each imaging session, the red cross shows the mean \pm SEM (A, B) Correlations were measured for all possible pairs. In (A), correlations are computed with respect to astrocytic response field (mean correlation inside the response field 0.11 ± 0.01 ; mean correlation outside the response field 0.07 ± 0.01 , $p = 6.4E-3$ Wilcoxon rank sums test). In (B), correlations are computed with respect to neuronal response field (mean correlation inside the response field 0.12 ± 0.01 ; mean correlation outside the response field 0.07 ± 0.01 , $p = 1.1E-3$ Wilcoxon rank sums test). (C, D) Same as (A, B) but correlations were computed only on synergistic pairs based on the value of ΔI (see Methods, Fig 6, and S11 Fig). In (C), correlations are computed with respect to astrocytic response field (mean correlation inside the response field 0.12 ± 0.01 ; mean correlation outside the response field 0.09 ± 0.01 , $p = 7.8E-3$ Wilcoxon rank sums test). In (D), correlations are computed with respect to neuronal response field (mean correlation inside the response field 0.13 ± 0.01 ; mean correlation outside the response field 0.08 ± 0.01 , $p = 1.8E-3$ Wilcoxon rank sums test). For each pair of ROIs, correlations were computed averaging 100 resampling to compensate unbalanced observations inside and outside the response field. Data from 11 imaging sessions on 7 animals. The data presented in this figure can be found in S5 Data. ROI, region of interest; SEM, standard error of the mean.

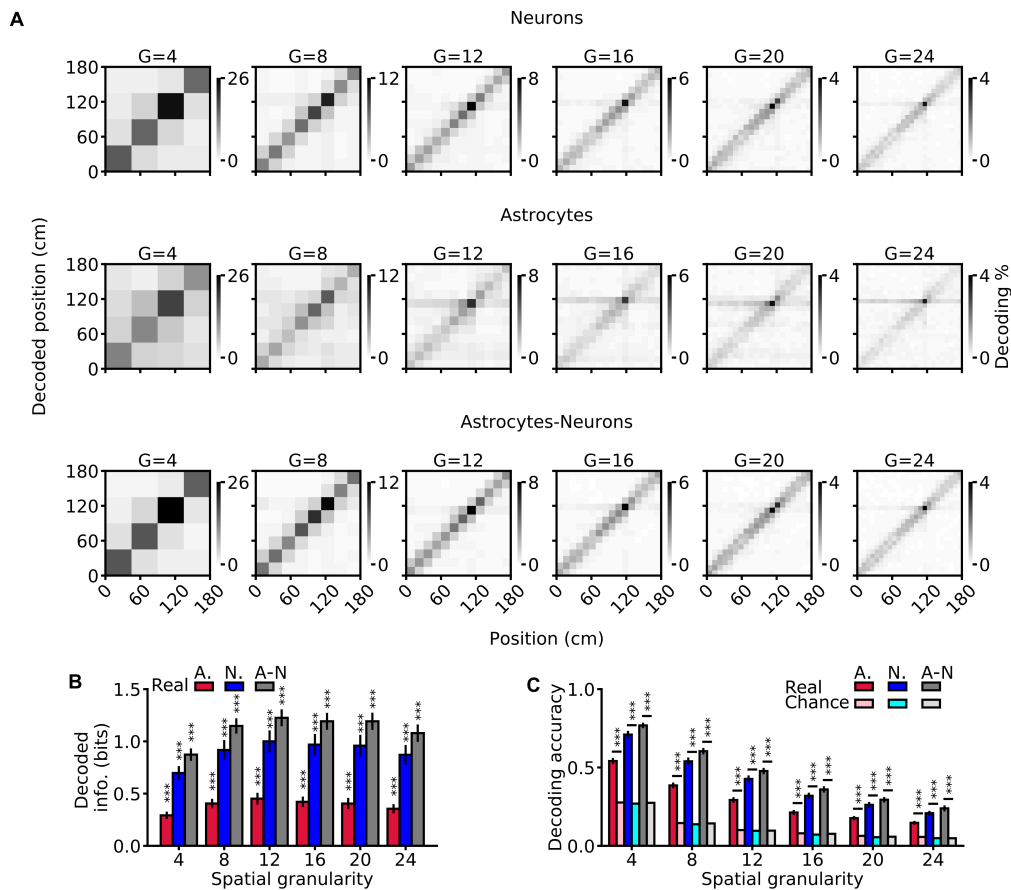


Figure A.22: Decoding the animal's position from neuronal and astrocytic population vectors. (A) Confusion matrices of an SVM classifier decoding the mouse's position using population vectors comprising neuronal (top), astrocytic (middle), and neuronal + astrocytic ROIs (bottom) for various spatial granularities ($G = 4, 8, 12, 16, 20, 24$). The true position of the animal is shown on the x-axis and the decoded position on the y-axis. Gray scale indicates the percentage of occurrence of each matrix element. (B) Decoded mutual information between predicted and real position in the linear track and (C) decoding accuracy for the different population vectors as a function of spatial granularity. In B and C, asterisks indicate significance against chance level (S5 and S10 Tables). Data are displayed as mean \pm SEM and were collected in 11 imaging sessions from 7 animals. The data presented in this figure can be found in S5 Data. ROI, region of interest; SEM, standard error of the mean; SVM, support vector machine.

Appendix B

Chapter 4: Supplementary material

B.1 Neuronal and astrocytic algorithms

STNeuroNet implementation We segmented dataset-1 with STNeuroNet [182] software validating its performances using leave-one-out cross validation strategy. We preprocessed our data as described in [182] and we adapted the consensus annotation (see consensus annotation) to identify active somata of astrocyte in each frame of our data (github.com/soltanianzadeh/STNeuroNet, `prepareTemporalMask.m`). In the training dataset, somata were classified as active/inactive analyzing df/f0 traces extracted using the procedure described in [111] to detect statistically significant calcium events. For each FOV we generated the training set cropping 120x144x144 voxels surrounding each somata in the consensus annotation. Then, we trained the net for 5000 epochs with learning rate 0.5×10^{-4} and batch size of 3. The loss function always converged to a plateau within 5000 epochs with these training parameters. Then, we used the same training procedure outlined by [182].

Caiman implementation We segmented dataset-1 with CaImAn [181] software validating its performances against the consensus annotations. CaImAn hyperparameters were set according to astrocytic somata morphology [31] and signal dynamics. We used patch-size = [80,80] and overlap = [20,20] for dataset-1. Components to be found is set to $K = 1$ since in these patches there is at least 1 astrocytic somata. Decay time is 1.5 s and we set merging threshold equal to 0.6 in each test. Other parameters were set to default settings.

UNet2DS implementation We segmented dataset-1 with UNet2DS software (<https://github.com/alexklibisz/deep-calcium>) validating its performances using leave-one-out cross validation strategy. For dataset-1 we used the same training procedure outlined in [180], we used 50 epochs with 100 training iterations in each epoch using sixteen randomly cropped 128×128 pixels regions from the mean image, utilizing

the dice-loss and the Adam optimizer. We monitored the F1 score on a validation set, selected from the training set (5% of the training set) to ensure the network was not overfitting.

GECI-Quant To perform semantic segmentation with GECI-Quant annotator-1 followed the procedure described in [98]. Briefly, for each FOV in dataset-1 and dataset-2, the annotator selected for two regions of interest for every astrocyte corresponding to soma and astrocytic domain, respectively. Then the annotator-1 manually selected an intensity threshold for each region of interest following the procedure outlined in [98]. GECI-Quant segmentations were used to compute the performances.

B.2 Algorithm details

Spatial sharpening Module. In the Spatial sharpening module, we used CLAHE Algorithm and Sharpening Kernel Convolution to enhance the median projection of the filtered FOV recordings. We used the OpenCV-python [198] = 4.1.0.25 implementation of CLAHE algorithm with tile-Size equal to 8x8. For the sharpening kernel convolution, we used K as kernel to convolve with the input image.

$$K = \begin{bmatrix} -1 & -1 & -1 \\ -1 & 9 & -1 \\ -1 & -1 & -1 \end{bmatrix} \quad (\text{B.1})$$

Local Activity Filtering Module. The local time filter module removes background pixel from the single-cell sharpened spatial map. If we define pixels segmented in consensus annotations as true positive, the thresholds in local time filter module have to be tuned on the training dataset limiting the average number of true positive pixels removed by the module. We generated a set of 4 couples (α_1, α_2) of thresholds: (0.3,0.15), (0.25,0.1), (0.2,0.07), (0.15,0.05) on which the local time filtering module can be tuned. The module selects the couple (α_1, α_2) with the highest threshold values resulting in an average number of removed true positive pixels smaller than 5%.

Data Augmentation. For data augmentation during training we used 20 transformation of input images: rotation by 90° , 180° , 270° , gaussian blurring with a 3x3 kernel and $\sigma=3$, gaussian noise sampling values from a Gaussian distribution with $\mu = 0$ and $\sigma = 0.3$, salt and pepper noise, scaling of image size by factor 0.8 and 1.4, 4 Perspective transformation, horizontal and vertical flipping, pixels intensity scaling by factors 3 and 0.5, pincushion transformation, barrel transformation, 2 Elastic transformation.

Cell-wise probability map. The DNN outputs consists in a 3D tensor whose dimensions are: input height, input width and 3 channels corresponding to the probability of the pixel to belong to somata, processes, or background classes. We find the maximum probability channel for each pixel and set to 0 the other 2 channels. Then for the somata class we binarize the somata-channel and set to 1 the pixel with probability greater than 0. Then we find all the clusters of connected pixels in the map (connected-Components function in OpenCV, [198]). For each cluster we computed the average probability across its pixels. We removed a cluster if the average probability is less than 905%. RASTA compares this filtered binary map with the somata FOV segmentation results removing somata that don't overlap with any cluster. A cluster and a soma overlap when the common area between the two cluster is greater than $0.1 * \max(\text{Area}_{\text{soma}}, \text{Area}_{\text{cluster}})$.

Removal of DNN artifacts. Processes artifacts in FOV are removed from FOV if not connected spatially to a soma. For each FOV, a binary mask is generated merging processes and somata ROIs. Then, all the connected components (CCs, clusters of pixels which are connected to each other through 8-pixel connectivity) in the binary mask are computed. Each CC which does not include any soma ROI is neglected. Then, we use these filtered CCs to remove processes ROIs which do not belong to them.

Table S1. Results of each annotator against consensus annotation of dataset-1. Detection and Segmentation results are given using F1-score (Precision, Recall) metrics (mean±sem)

	Detection	Segmentation	
		Somata	Processes
Annotator-1	0.88±0.02 (0.91±0.02,0.89±0.03)	0.845±0.009 (0.78±0.02,0.939±0.005)	0.62±0.02 (0.56±0.02,0.74±0.01)
Annotator -2	0.88±0.02 (0.87±0.03,0.91±0.02)	0.84±0.01 (0.85±0.01,0.852±0.006)	0.56±0.01 (0.55±0.02,0.62±0.02)
Annotator -3	0.90±0.02 (0.89±0.03,0.92±0.02)	0.882±0.007 (0.923±0.008,0.86±0.01)	0.64±0.02 (0.75±0.02,0.59±0.02)

Table S2. Results of RASTA, STNeuronet, Caiman and GECI-Quant against consensus annotation of dataset-1. Detection and Segmentation results are given using F1-score (Precision, Recall) metrics (mean±sem)

	Detection	Segmentation	
		Somata	Processes
RASTA	0.81±0.04 (0.79±0.04,0.87±0.03)	0.822±0.008 (0.78±0.02,0.89±0.01)	0.59±0.01 (0.62±0.02,0.60±0.01)
STNeuronet	0.27±0.05 (0.26±0.05,0.32±0.06)	-	-
Caiman	0.20±0.04 (0.25±0.04,0.17±0.03)	-	-
UNet2DS	0.65±0.04 (0.67±0.06,0.67±0.05)	-	-
GECI-Quant	0.74±0.04 (0.72±0.04,0.76±0.04)	0.775±0.008 (0.72±0.01,0.88±0.01)	0.33±0.02 (0.25±0.02,0.65±0.03)

Table S3. Results of RASTA, and AQuA in reconstructing astrocytic morphology. Results are F1-score (Precision, Recall) metrics (mean±sem)

	F1-score (Precision, Recall)
RASTA	0.62±0.03 (0.61±0.03,0.65±0.03)
AQuA	0.23±0.02 (0.12±0.02,0.53±0.2)

Table S4. Results of each annotator and RASTA against consensus annotation of dataset-2. Detection and Segmentation results are given using F1-score (Precision, Recall) metrics (mean±sem)

	Detection	Segmentation	
		Somata	Processes
Annotator -1	0.859±0.008 (0.88±0.01, 0.83±0.01)	0.86±0.004 (0.90±0.01,0.84±0.02)	0.63±0.02 (0.65±0.01,0.67±0.03)
Annotator -2	0.84±0.02 (0.89±0.01, 0.80±0.03)	0.836±0.006 (0.918±0.003,0.78±0.01)	0.58±0.02 (0.58±0.02,0.64±0.03)
Annotator -3	0.85±0.02 (0.83±0.02, 0.88±0.02)	0.834±0.005 (0.935±0.006,0.76±0.01)	0.53±0.02 (0.60±0.02,0.52±0.02)
RASTA	0.81±0.02 (0.76±0.02,0.86±0.01)	0.822±0.004 (0.805±0.009,0.910±0.008)	0.57±0.02 (0.68±0.02,0.55±0.02)

Table S5. Results of each annotator and RASTA against consensus annotation of dataset-3. Detection and Segmentation results are given using F1-score (Precision, Recall) metrics (mean±sem)

	Detection	Segmentation	
		Somata	Processes
Annotator -1	0.84±0.01 (0.91±0.01, 0.78±0.02)	0.853±0.006 (0.878±0.008,0.85±0.01)	0.62±0.01 (0.69±0.02,0.61±0.02)
Annotator -2	0.83±0.02 (0.81±0.02, 0.85±0.03)	0.856±0.003 (0.904±0.005,0.825±0.005)	0.55±0.02 (0.58±0.01,0.60±0.02)
Annotator -3	0.81±0.03 (0.78±0.03, 0.85±0.03)	0.815±0.009 (0.962±0.005,0.717±0.02)	0.55±0.01 (0.66±0.01,0.51±0.01)
RASTA	0.78±0.02 (0.76±0.04,0.82±0.03)	0.835±0.002 (0.780±0.008,0.92±0.01)	0.57±0.01 (0.57±0.02,0.63±0.01)

Table S6. Results of each annotator and RASTA against consensus annotation of dataset-4. Detection and Segmentation results are given using F1-score (Precision, Recall) metrics (mean±sem)

	Detection	Segmentation	
		Somata	Processes
Annotator -1	0.81±0.01 (0.90±0.01, 0.75±0.02)	0.835±0.006 (0.84±0.01,0.852±0.007)	0.55±0.02 (0.69±0.02,0.52±0.03)
Annotator -2	0.72±0.02 (0.73±0.03, 0.73±0.03)	0.827±0.007 (0.897±0.007,0.78±0.01)	0.50±0.02 (0.63±0.01,0.47±0.02)
Annotator -3	0.74±0.03 (0.70±0.06, 0.80±0.01)	0.834±0.004 (0.898±0.008,0.79±0.01)	0.50±0.02 (0.65±0.03,0.46±0.02)
RASTA	0.80±0.02 (0.78±0.03,0.82±0.02)	0.813±0.006 (0.755±0.007,0.904±0.006)	0.53±0.01 (0.50±0.02,0.66±0.02)

Table S7. RASTA DNN training parameters

		Epochs		Optimizer	lr	Batch size	Input image size
		N1	N2				
Dataset-1		12	3	Adam	10 ⁻⁴	35	96x96
Dataset-2		12	3	Adam	10 ⁻⁴	35	48x48
Dataset-3	Training on Dataset-1	-	-	-	-	-	-
Dataset-4	Training on Dataset-1	-	-	-	-	-	-

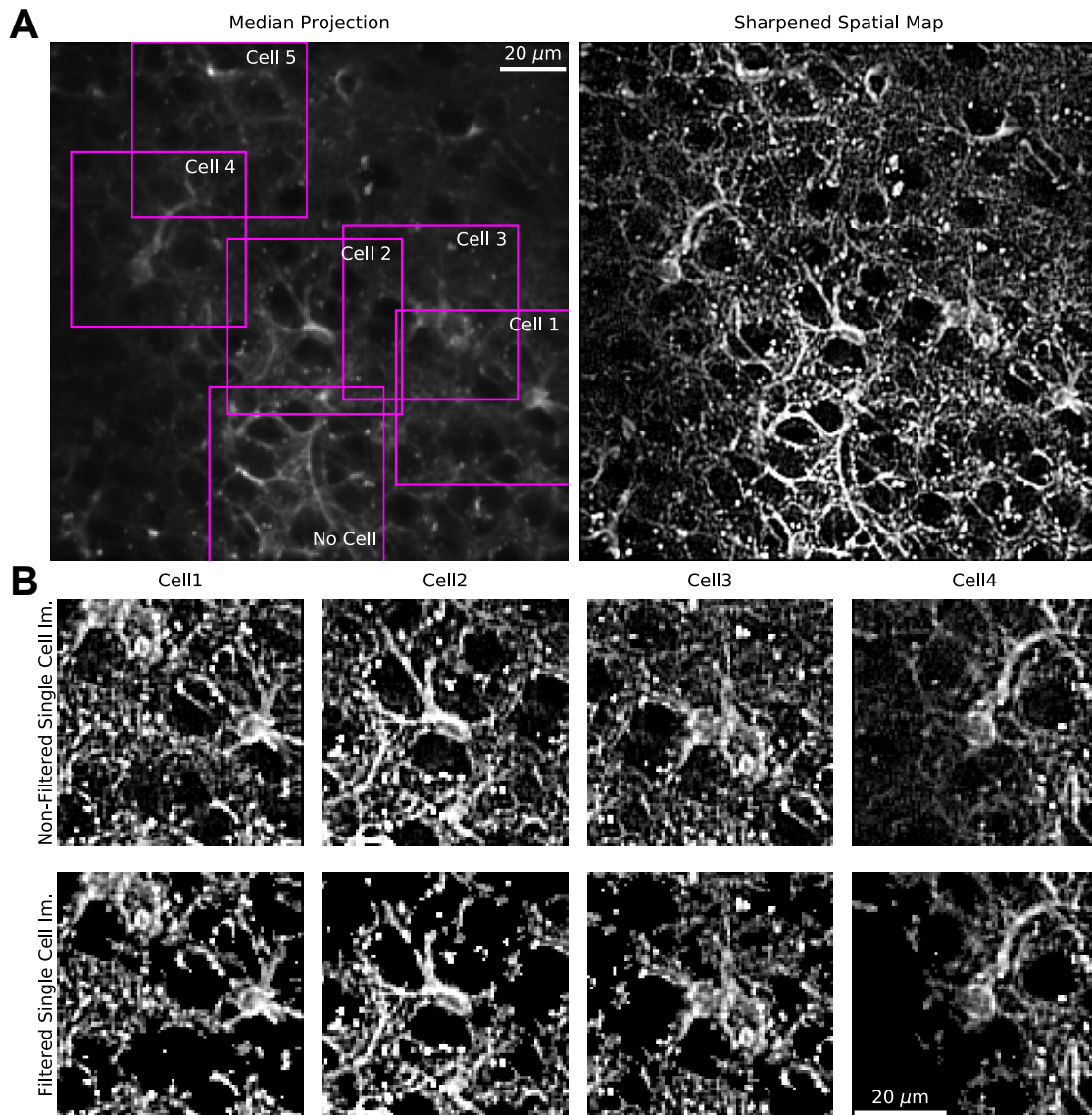


Figure B.1: RASTA pre-processing. A) Left: median projection of a representative FOV (Id:2) overlaid with putative bounding boxes computed by activity map generation. Right: spatial sharpening of the same FOV shown on the left panel. B) Top: zoom in showing sharpened images of four cells (cell 1-4) extracted from the putative bounding boxes shown in the left panel of A. Bottom: for each image the result of local activity filtering is shown.

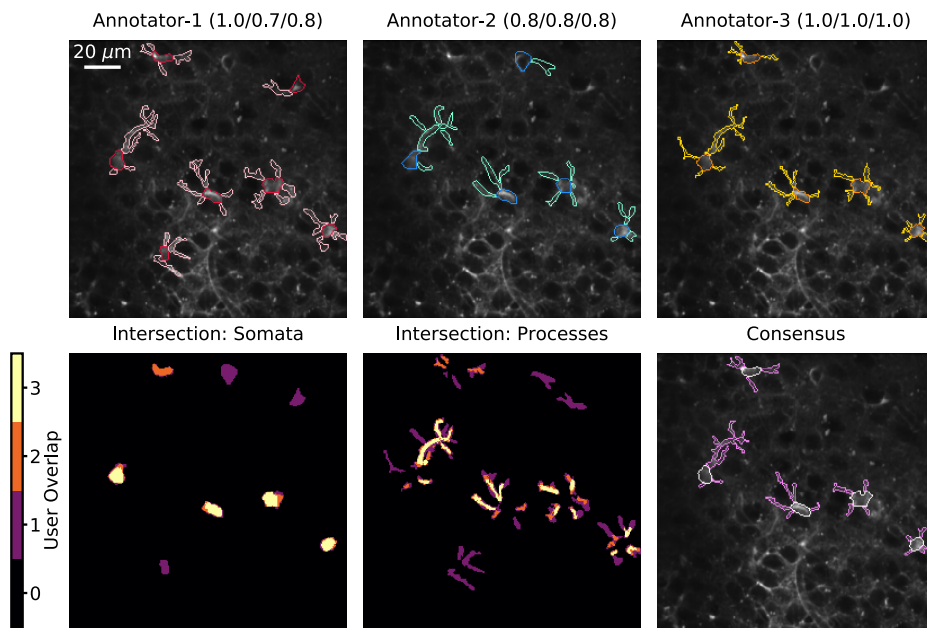


Figure B.2: Generation of the consensus annotation. Top: individual manual annotations (colored contours) for FOV (Id:2) by three graders (annotator-1, annotator-2, and annotator-3). Manual annotations are plotted on top of the median projection of the two-photon t-series. The numbers in parenthesis in the top label report detection precision, recall, and F1 score. Bottom: intersection of somata annotations (left), intersection of process annotations (middle), and result of the consensus annotation (right).

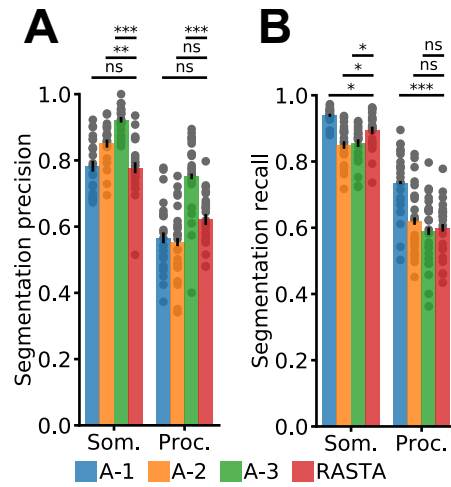


Figure B.3: Precision and Recall of RASTA semantic segmentation against human annotators on dataset-1. A-B) Precision (A) and Recall (B) of somata and process segmentation for the three annotators and RASTA (two-sided Wilcoxon rank sum test $N = 24$; LOOCV results). See also table S1. In this as well as other figures: n.s., not significant, * $p < 0.05$, ** $p < 0.005$, and *** $p < 0.0005$.

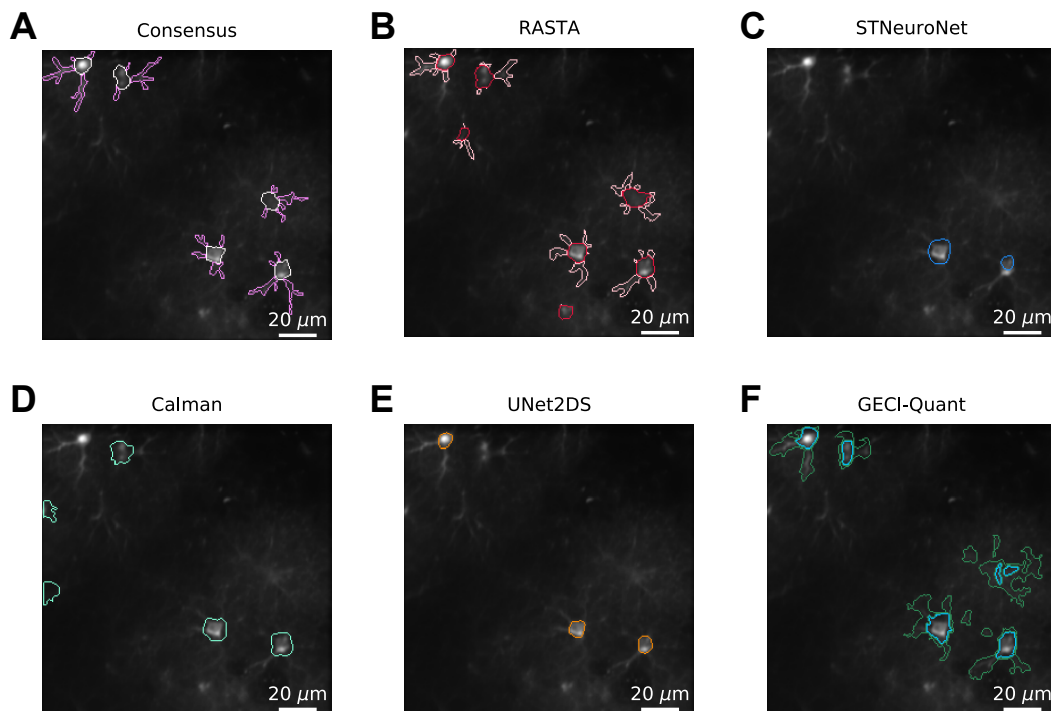


Figure B.4: Representative example of segmentations of somata and processes (dataset-1 Id:5) for: A) the consensus annotation, somata (white), processes (light purple); B) RASTA, somata (red), processes (pink); C) STNeuroNet, somata (blue); D) CalmAn, somata (light green); E) UNet2DS, somata (orange); F) GECI-Quant, somata (light blue), processes (green).

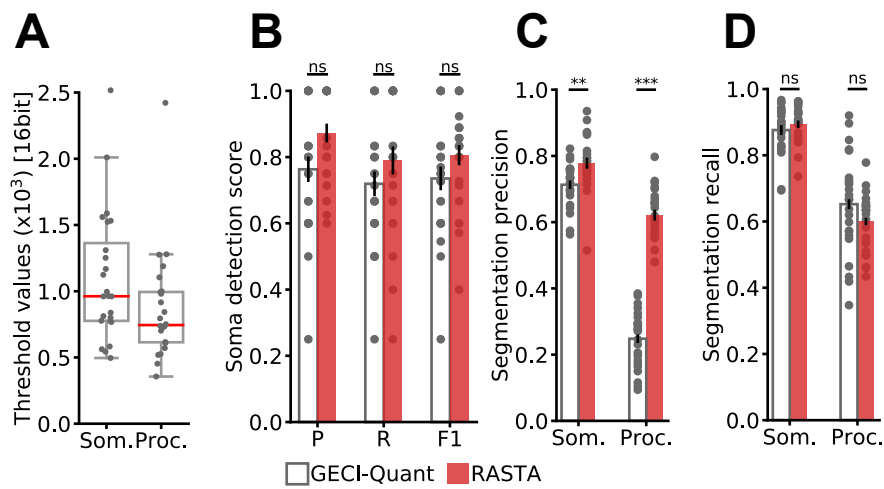


Figure B.5: RASTA semantic segmentation against GECI-quant segmentation. A) GECI-Quant thresholds distributions for dataset-1. Box charts show the median values (red line) and the interquartile range (IQR, black top and bottom limit of the box). The whiskers extend to 1.5 times the IQR. B) Geci-Quant soma detection vs. RASTA in dataset-1. Precision, recall, and F1-score are shown (two-sided Wilcoxon signed rank sum test $N = 24$; LOOCV results). C-D) Precision (C) and recall (D) for somata and process segmentation (two-sided Wilcoxon rank sum test $N = 24$; LOOCV results). See also table S2.

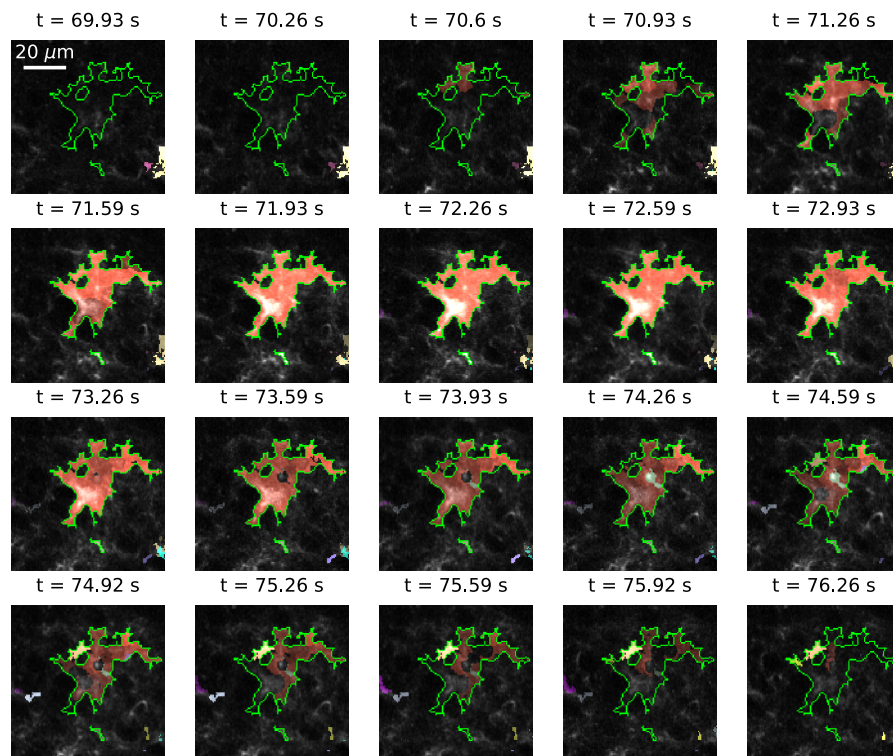


Figure B.6: RASTA seeding of event-based segmentation. Example of a spatiotemporal Ca²⁺ events (red to white colors) detected with AQuA when seeded with the astrocytic domain (green line) identified by RASTA. Each image represents a single frame of a representative t-series (id: 2, dataset-1). Colors superimposed to each frame represent a detected event in the astrocyte. Frame acquisition time is reported on the top of each image.

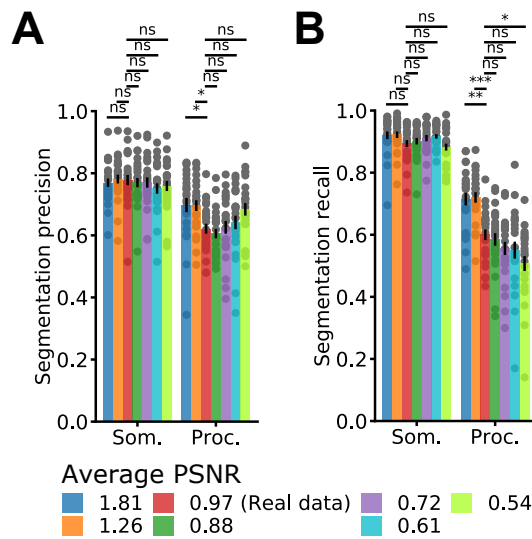


Figure B.7: RASTA performance under various signal-to-noise ratio regimes. A-B) Precision (A) and Recall (B) for RASTA segmentation of somata and processes under the different simulated conditions of PSNR (two-sided Wilcoxon rank sum test $N = 24$; LOOCV results).

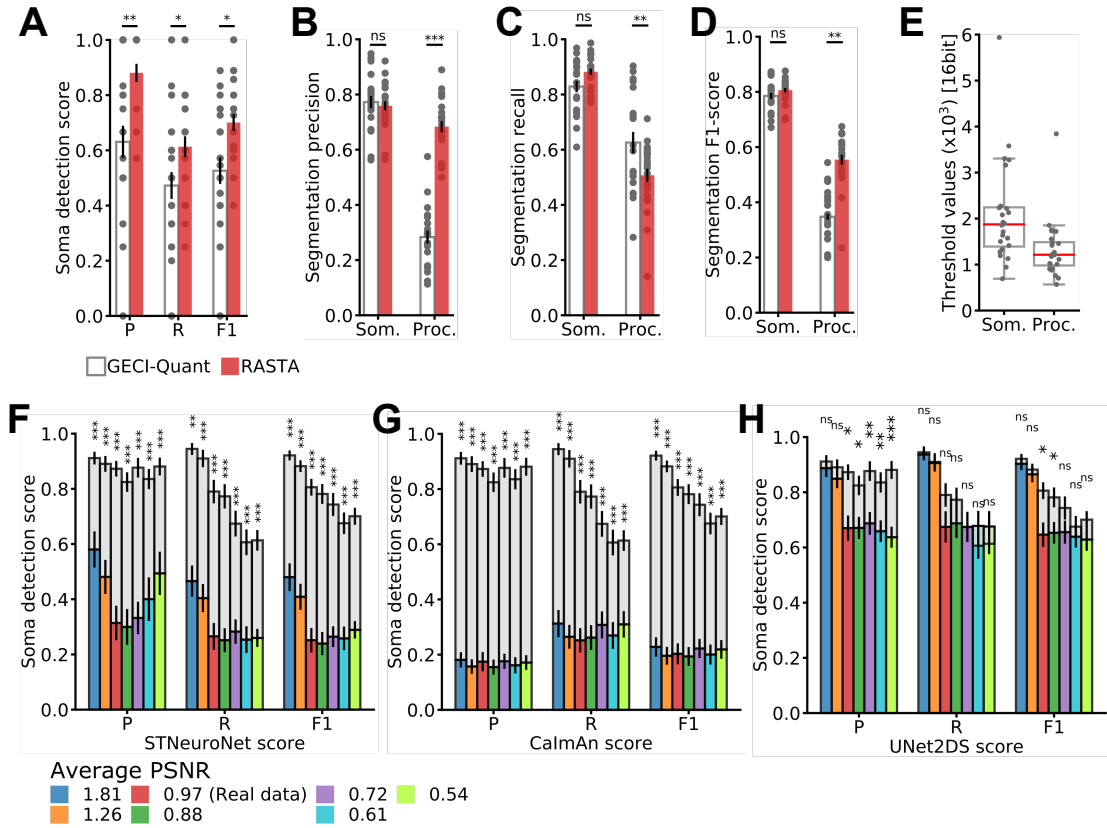


Figure B.8: Performance of RASTA and other algorithms under various signal-to-noise ratio regimes. A) Precision, Recall, and F1-score for soma detection for GECI-Quant (white) and Rasta (red) in the 0.54 PSNR dataset (two-sided Wilcoxon signed rank sum test $N = 24$; LOOCV results). B-D) Segmentation Precision (B), Recall (C), and F1-score (D) GECI-Quant (white) and RASTA (red) on the 0.54 PSNR dataset (two-sided Wilcoxon rank sum test $N = 24$; LOOCV results). E) Distribution of GECI-Quant thresholds distributions in the 0.54 PSNR dataset for somata (Som.) and processes (Proc.). Box charts show the median values (red line) and the interquartile range (IQR, black top and bottom limit of the box). The whiskers extend to 1.5 times the IQR. F-H) Effect of artificial noise on soma detection performances. Detection Precision, Recall and F1-score for RASTA (grey bars), STNeuroNet (F), CaImAn (G), and UNet2DS (H) on the same dataset but with different level of PSNR (two-sided Wilcoxon rank sum test $N = 24$; LOOCV results).

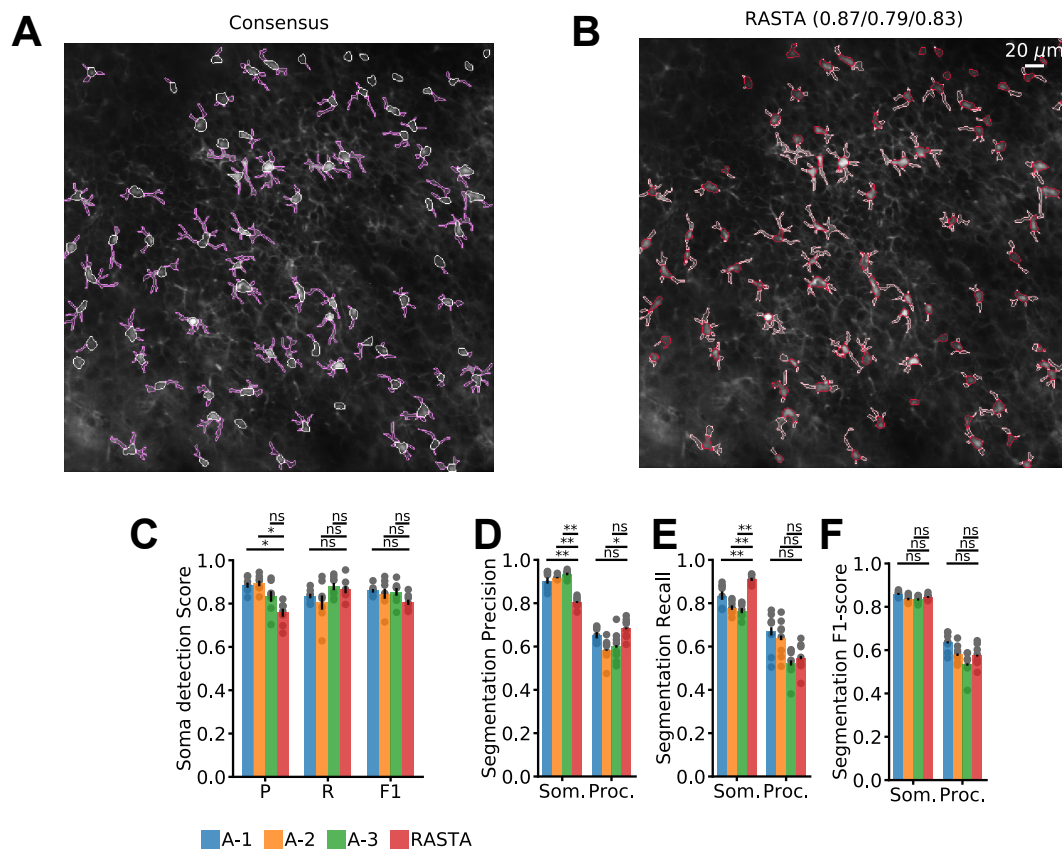


Figure B.11: RASTA detection and segmentation performance on dataset-2. A) Consensus annotation of one representative FOV (Id: 3) showing Td-Tomato-expressing astrocytes. B) RASTA segmentation result for the same FOV shown in (A). C) Detection precision, Recall, and F1-score for RASTA and the three annotators (two-sided Wilcoxon rank sum test $N = 8$; LOOCV results). D-F) Segmentation Precision, Recall, and F1-score of RASTA and the three annotators for somata (Som.) and processes (Proc.) (two-sided Wilcoxon rank sum test $N = 8$; LOOCV results). See also Table S3.

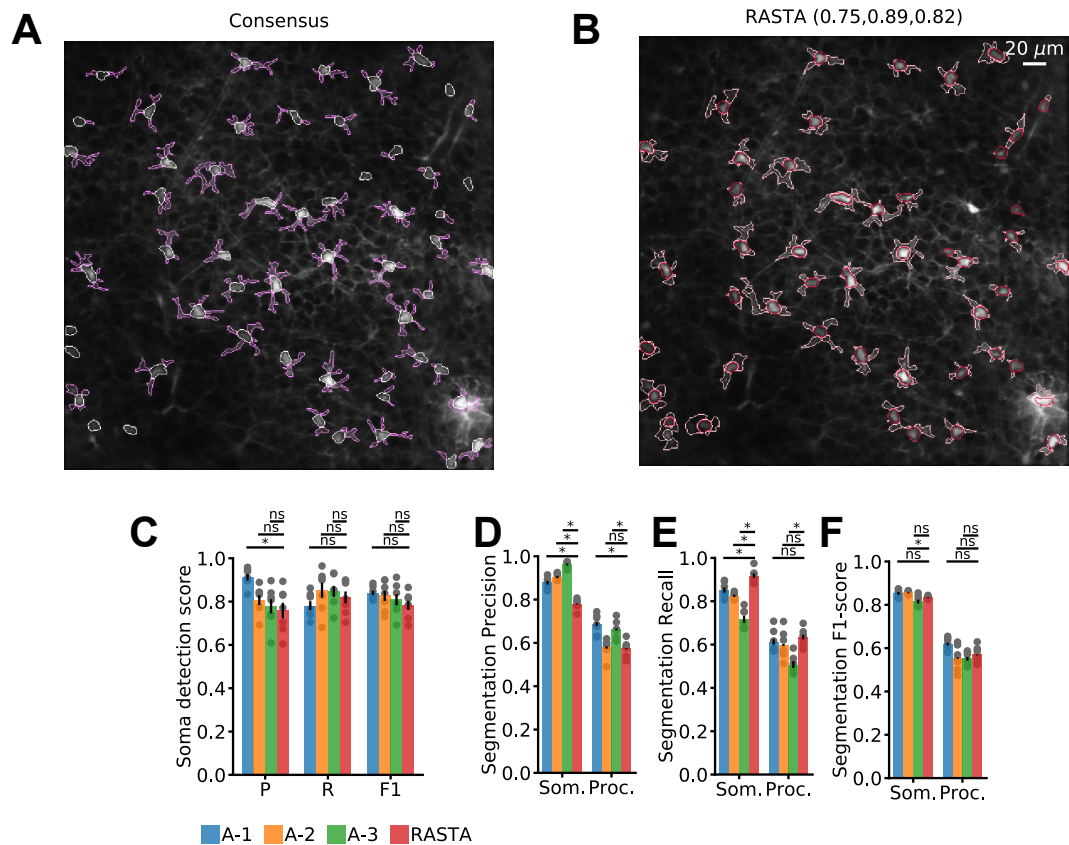


Figure B.12: RASTA detection and segmentation performance on dataset-3. A) Consensus annotation of one representative FOV (Id: 5) showing Td-Tomato-expressing astrocytes. B) RASTA segmentation result for the same FOV shown in (A). C) Detection precision, Recall, and F1-score for RASTA and the three annotators (two-sided Wilcoxon rank sum test $N = 7$; LOOCV results). D-F) Segmentation Precision, Recall, and F1-score of RASTA and the three annotators for somata (Som.) and processes (Proc.) (two-sided Wilcoxon rank sum test $N=7$; LOOCV results). See also Table S4.

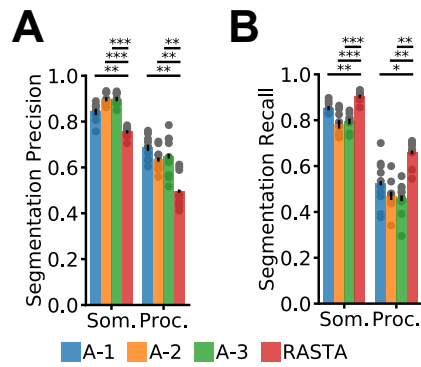


Figure B.13: RASTA detection and segmentation performance on dataset-4. A-B) Segmentation Precision (A) and Recall (B) of RASTA and the three annotators for somata (Som.) and processes (Proc.) (two-sided Wilcoxon rank sum test $N=10$; LOOCV results). See also Table S5.

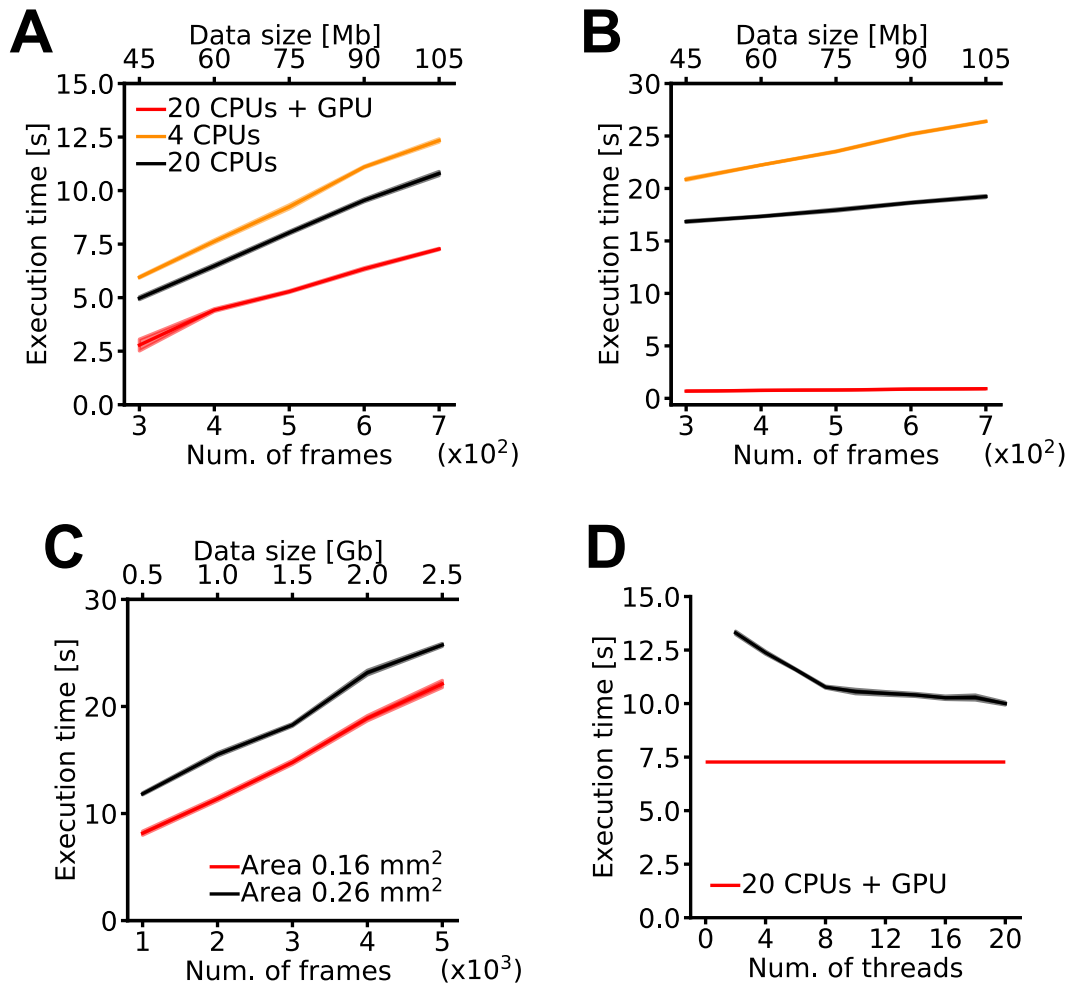


Figure B.14: Execution time of the RASTA inference pipeline. A) Execution time of RASTA inference pipeline without the cross-correlation analysis as a function of the size of the input t-series in dataset-1. The different colors indicate the execution time for three different hardware configurations: 4 CPUs, 20 CPUs, and 20 CPUs + GPU. B) Execution time for the cross-correlation module as a function of the size of the input t-series in dataset-1. Color code same as in (A). Please note that the GPU configuration is faster than the multi-processing CPU configuration. This is because the computation of cross-correlation value between pixels can be massively parallelizable with GPUs. C) Execution time for the inference pipeline without cross-correlation analysis as a function of the size of the input t-series for dataset-2 (black, area 0.26 mm²) and dataset-3 (red, area of FOV 0.16 mm²). D) Execution time of RASTA inference pipeline on a 700 frames t-series of dataset-1 without the cross-correlation analysis as a function of the number of cores used (black line). The red line represents the execution time of RASTA with the 20 CPUs + GPU hardware configuration.